A MODEL FOR DEEP GEOTHERMAL BRINES: STATE SPACE DESCRIPTION AND THERMODYNAMIC PROPERTIES

A thesis presented in partial fulfilment
of the requirements for
the degree of Ph.D. in
Mathematics at
Massey University

Christopher Charles Palliser

June 1998

Abstract

To facilitate the simulation of heat and fluid transport in deep geophysical environments, this thesis proposes correlations for calculation of density, enthalpy and viscosity values for brine (H_2O + NaCl) over a wide range of temperature T, pressure p and mass fraction of sodium chloride X. Although geothermal fluids are not pure H_2O-NaCl systems, they are mainly composed of H_2O and NaCl and in this thesis we model geothermal fluids as brines. Firstly T-p-X state space delineations of such a model fluid are described. Then using experimental and calculated data, approximate correlations for the three properties are given in terms of the primary variables T, p and X. These correlations cover the entire T-p-X state space and can be used in subroutines suitable for use in numerical simulation programs. The case of one-dimensional, steady vertical flows is described and our correlations for the state space delineations and the thermodynamic properties are tested on such flows.

Acknowledgements

This thesis is dedicated to my wife , Alataua. Without her love and prayers, none of this would have been possible. Fa'afetai lava la'u pele.

My special thanks to my chief supervisor, Professor Robert McKibbin, for his expertise, guidance and patience, and also thank you to Dr. Alex McNabb for his help.

My love and thanks to my father, Ray, for his generosity and support and also to my children, Matthew, Carissa, Joshua, Susan and Samuel.

To my extended family and church family at St. Oswalds, I give my thanks for their prayers and encouragement over the years.

Thank you to Mark Johnston for his assistance with computing and Liz Herkes for drawing some of the diagrams.

Thank you to Massey University for the Doctoral Scholarship and to Dr. Graham Weir and Industrial Research Limited for their financial assistance during recent months.

Chapters 3 and 4 have been accepted for publication in the journal called Transport in Porous Media.

Nomenclature

The unit volume and area referred to here are the unit volume and area of the fluid-saturated porous medium, i.e. the fluid-filled geothermal system.

A_e	Internal energy per unit volume, J/m^3
A_m	Total mass per unit volume, kg/m^3
A_m^γ	Mass per unit volume of the sodium chloride ($\gamma = c$), rock ($\gamma = r$) or water ($\gamma = w$), kg/m^3
C	Chemical composition
c	Specific heat at constant volume, kJ/kg K = J/g K
$\mathbf{g}$, g	Acceleration due to gravity, m/s^2
h	Specific enthalpy, kJ/kg = J/g
k	Permeability, m^2
k_{ri}	Relative permeability of the liquid ($i = \ell$) or the gas ($i = g$), dimensionless
K	Thermal conductivity, W/m K
m_γ	Mass flux per unit area of the sodium chloride ($\gamma = c$) or the water ($\gamma = w$), kg/m^2 s
NCG	Non-condensible gas(es)
p	Pressure, bars absolute
q_e	Rate of production or injection of energy per unit volume, J/m^3 s
q_m^γ	Rate of production or injection of mass per unit volume of the sodium chloride ($\gamma = c$) or the water ($\gamma = w$), kg/m^3 s
Q_e, q	Energy flux per unit area, J/m^2 s
Q_m	Total mass flux per unit area, kg/m^2 s
Q_m^γ	Mass flux per unit area of the sodium chloride ($\gamma = c$) or the water ($\gamma = w$), kg/m^2 s

Q_{mi}	Mass flux of liquid ($i = \ell$) or gas ($i = g$) per unit area, kg/m^2 s
Q^{γ}_{mi}	Mass flux per unit area of γ in the i phase, $\gamma = w$ (water) or c (sodium chloride), $i = \ell$ (liquid) or g (gas), kg/m^2 s
t	Time , s
T	Temperature, °C
TDS	Total dissolved solids
S	Saturation, dimensionless
u	Specific internal energy, kJ/kg = J/g
V	Volume, m^3
VPL	Vapour pressure lowering
$\mathbf{x}$	Position vector, m
X	Mass fraction of sodium chloride, dimensionless
z	Vertical coordinate, m

Subscripts

b	Brine
bg	Brine gas or vapour
$b\ell$	Brine liquid
c	Sodium chloride
cap	Capillary
cg	Sodium chloride gas
$c\ell$	Sodium chloride liquid
$c\ sat$	Sodium chloride saturation
$cg\ sat$	Saturated sodium chloride gas
$c\ell\ sat$	Saturated sodium chloride liquid
$CRIT$	Critical
e	Energy
f	Fluid
g	Gas or vapour
gs	Gas phase of the two-phase fluid
$g\ SAT\ (= bg\ sat)$	Halite-saturated gas on the three-phase surface
$g\ sol$	Maximum solubility in water gas (vapour) or halite-saturated gas

ℓ	Liquid
ℓs	Liquid phase of the two-phase fluid
$\ell\ SAT\ (= b\ell\ sat)$	Halite-saturated liquid on the three-phase surface
$\ell\ sol$	Maximum solubility in liquid water or halite-saturated liquid
m	Mass
mg	Mass of gas
$m\ell$	Mass of liquid
r	Rock
SAT	Saturation
w	Water
$w\ sat$	Water saturation
$wg\ sat$	Saturated water gas
$w\ell\ sat$	Saturated liquid water
1000	1000 bars absolute
$2b$	Region 2b

Superscripts

c	Sodium chloride
w	Water

Greek letters

ε	Volume fraction of pore space occupied by the fluid or voidage, dimensionless
μ	Dynamic viscosity, kg/m s
$\nu = \mu/\rho$	Kinematic viscosity, m^2/s
ρ	Density, kg/m^3
ϕ	Porosity, dimensionless

Contents

Chapter 1

Introduction

1.1 Background

Geothermal systems are found near the Earth's surface, commonly at the boundaries of tectonic plates where the upward heat flux is higher than normal. These systems extend from the Earth's surface to magmatic heat sources at depth in the Earth's crust. Such systems are found all over the world and New Zealand's best known example is the Wairakei geothermal system. This geothermal system is part of what is known as the Taupo Volcanic Zone (TVZ), a central North Island volcanic zone which contains about twenty geothermal fields. The near-surface permeable fluid-saturated regions of TVZ fields are accessible by drilling to depths of three kilometres or greater below the surface. These near-surface energy resources, often referred to as geothermal reservoirs, are used for direct heat applications (e.g. home heating, warm baths, prawn farming) and electricity generation (e.g. Wairakei and Ohaaki in New Zealand).

In geothermal or hydrothermal systems, heat from depth is transported to the surface by thermal convection of heated groundwater. Figure 1.1 shows a schematic of a hydrothermal system above sea level. It illustrates a large scale convective circulation of groundwater or meteoric (comes from the atmosphere) water. This cold groundwater percolates down through the porous rock matrix of the geothermal system by way of faults and fractures in the rocks, is heated, and then rises to the surface as a plume of hot fluid. The basic mechanism is buoyancy, since hot fluid is lighter than cold fluid. Near the top of the system, where the pressures are lower, boiling may occur. At depth the high pressures prevent boiling. For the

TVZ, [McNabb, 1992] estimated that at most 10 % of hydrothermal water is of magmatic origin, so that most of the water that is discharged is of meteoric origin and enters the system at the surface.

The temperatures in the mid to upper parts of reservoirs are less than the critical temperature of water (= 374.15 °C), i.e. subcritical temperatures. [The critical temperature and pressure of a substance mark the transition from being able to distinguish between the liquid and vapour (or gas) phases—subcritical, to being unable to distinguish between these phases, i.e. a single-phase which is neither liquid nor gas—supercritical.] At greater depths, the temperatures become supercritical; for example, in 1994–1995 at a depth of 3,729 metres in well WD1 at Kakkonda in Japan, temperatures of 500 °C were observed [Lichti and Sanada, 1997]. At depths where magma is reached, the temperatures can be as high as 800–1200 °C [McNabb, 1992] and [McNabb et al., 1993].

The cooling magma, as depicted in Figure 1.1, provides the heat source for the geothermal system. For the TVZ, [McNabb, 1992] estimated the surface of the magma to be 5–10 kilometres below the Earth's surface. There is debate concerning the nature of these heat sources which underlie geothermal fields. [Kissling, 1996] discussed the particular debate about the heat source beneath the TVZ. One school of thought is that the heat source for the TVZ is an isolated magmatic body or pluton placed at depth which is cooled by the circulation of the overlying groundwater. [Cathles, 1977] studied such systems and and found that a single magmatic intrusion is not sufficient to supply the heat for a Wairakei-type geothermal system. He suggested that continuous replenishment must be occurring. More recently, [McNabb, 1992] proposed a continuous replenishment model in which a stably-stratified dense saline hotplate forms at depth due to the phase behaviour of high temperature H_2O-NaCl mixtures. He postulated that this dense layer, which lies between the base of the reservoirs and the magma surface, thermally insulates the groundwater from molten magmatic temperatures which can reach 1200 °C.

In order to try and utilize geothermal resources as efficiently and economically as possible, and also to ensure minimum disruption to the environment, modelling of geothermal systems, and reservoirs in particular, is necessary. Modelling helps determine the natural (prior to exploitation) state of a geothermal system and its behaviour under exploitation. As described in [O'Sullivan and McKibbin, 1989], the main aim of reservoir modelling is to set up a computer or mathematical model

which represents among other things, the permeability structure, heat and fluid inputs and the thermodynamic and transport properties of the geothermal fluids of the real reservoir with sufficient accuracy so that the simulated behaviour of the model over 20 or 30 years can be used confidently as a prediction of the performance of the real reservoir. This mathematical model involves the development of equations which express the principles of conservation of mass, linear momentum and energy, and which may be used to describe the transport of mass and heat in a porous medium. Solving these equations requires knowledge of the thermodynamic properties of density, enthalpy and viscosity of the geothermal fluid.

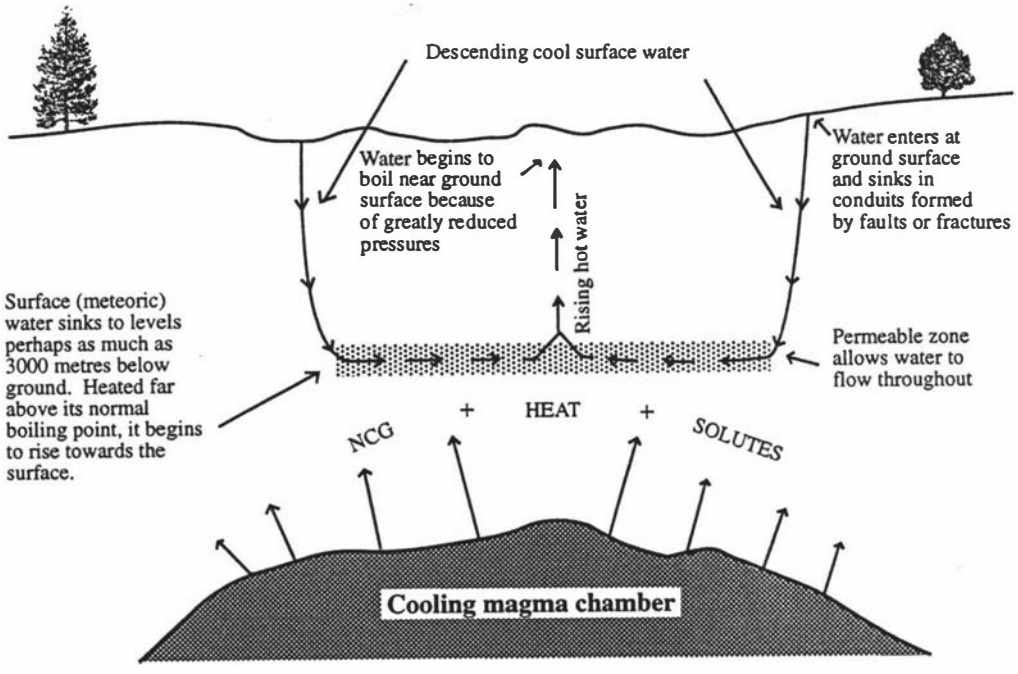

Figure 1.1: Schematic diagram of a hydrothermal system (above sea level), adapted from [Todd, 1980]

Initially geothermal fluids were modelled as pure water and the well known thermodynamic properties of pure water were used in numerical simulators such as MULKOM, see [Pruess, 1983]. These pure water models are of three types:

1. Single-phase, extending to supercritical temperatures (and pressures), e.g. [Cathles, 1977] and [Norton and Knight, 1977].

2. Multi-phase (single-phase liquid, single-phase steam, two-phase water—liquid

and steam), confined to subcritical temperatures,
e.g. [Faust and Mercer, 1981] and [Pruess, 1983].

3. Multi-phase, extending to supercritical temperatures,
e.g. [White and Kissling, 1992] and [Hayba and Ingebritsen, 1994].

However geothermal fluids consist not only of water (solvent) but also of dissolved solids (solutes) and non-condensible gases (NCG). It is thought that the cooling magma, see Figure 1.1, is the source of these solutes and NCG. According to [Battistelli et al., 1997], the total dissolved solids (TDS) content in geothermal reservoir fluids ranges from a few thousand ppm (wt.) up to about 300,000 ppm, with the principal solid being sodium chloride (NaCl). For example, the 3,729 metre deep well in Kakkonda, Japan (mentioned above), was found to have chloride concentrations of 200,000–300,000 ppm [Lichti and Sanada, 1997]. The concentration of the NCG in geothermal reservoir fluids ranges from a few hundred ppm (wt.) up to several tens of thousands ppm, with carbon dioxide (CO_2) occupying by far the greatest volume [Alkan et al., 1995] and [Battistelli et al., 1997]. The addition of solute and non-condensible gas components can significantly alter a reservoir's performance, hence geothermal fluids are also modelled as a water, solute and non-condensible gas mixture. Since NaCl and CO_2 are the main solute and non-condensible gas respectively, most effort has been directed at modelling mixtures which have NaCl and CO_2 representing the effects of the TDS and NCG respectively. Therefore work has been done on H_2O-CO_2, H_2O-NaCl and H_2O-CO_2-NaCl mixtures or systems. For example, [Battistelli et al., 1993] developed a new equation of state module for the TOUGH2 simulator (a later version of MULKOM). This module is able to handle mixtures of water, sodium chloride and a non-condensible gas at subcritical temperatures. Their paper concentrated on H_2O-NaCl-CO_2 mixtures. Various authors have used this module to model special features of reservoirs.

The only model for the geothermal fluid flow of these H_2O-NaCl and H_2O-CO_2-NaCl systems which extends to supercritical temperatures (and pressures), is the mathematical model that has been developed by [McKibbin and McNabb, 1993]. In this paper they developed correlations which delineate the entire H_2O-NaCl (brine) phase or state space, i.e. from pure water to pure sodium chloride, and temperature and pressure ranges which take in all the features of this state space

and therefore extend to supercritical temperatures and pressures. They also described the conservation equations and ran some simulations of the fluid flow of brine whose temperatures and pressures were typical of the deeper parts of geothermal systems [McKibbin and McNabb, 1995a]. In [McKibbin and McNabb, 1995b] they added CO_2 to their H_2O-NaCl model.

All of the above mathematical models for H_2O-NaCl or H_2O-NaCl-CO_2 systems require knowledge of the thermodynamic properties of density, specific enthalpy and kinematic viscosity of brine and the subcritical models use various formulae and correlations for these three brine properties. Compared with pure water however, there is not as much known about these properties of brine, especially at supercritical temperatures. For their model which extends to supercritical temperatures, McKibbin and McNabb use pure water subroutines for the specific enthalpy and kinematic viscosity. For the density at subcritical temperatures, they use that of single-phase water vapour if the pressure is less than the saturation pressure of water, $p_{w\ sat}(T)$; if the pressure is greater than $p_{w\ sat}(T)$, a brine density subroutine is used. For temperatures beyond critical, a brine density subroutine is also used.

What is now required are correlations for the density, specific enthalpy and kinematic viscosity of brine that extend to supercritical temperatures (and pressures) so that the temperature and pressure ranges of the deeper parts of geothermal reservoirs are covered. It is hoped that this will improve the models of these deeper reservoirs. This thesis develops such correlations (supercritical and subcritical) as well as modifying the state space description of the H_2O-NaCl system. These correlations and modifications, which cover the entire H_2O-NaCl state space, should also help research in the following areas:

- What is the nature of the fluids that are present above the cooling volcanic magma releasing solute-saturated vapours into the groundwater at depth in the Earth's crust, and in convecting hydrothermal systems on the seafloor? How do the fluid phase properties of brines influence heat transfer and the transport of minerals? Is the idea proposed in [McNabb, 1992] for the TVZ and in [McNabb et al., 1993] for seafloor hydrothermal systems feasible, i.e. do the phase and thermodynamic properties of brine make it possible that there are dense hot brine layers that form stably-stratified layers at depth which effectively shield the groundwater and convecting seawater from the highest magmatic temperatures?

- Adding salt (NaCl) to water considerably alters such important features like the critical point and the two-phase region (region where liquid and vapour or gas coexist). Salinity extends the critical point of pure water to a critical line and the analogy to the two-phase (saturation) line of water is a large two-phase region (volume in the 3-D temperature-pressure-salinity phase space) for brine. It is important to model the phase space of geothermal fluids accurately since, as discussed in [McNabb et al., 1993], when modelling fluid flow, it is found that phase changes play a major role in the behaviour of a system, because they produce sudden changes in the physical properties of the fluid, which in turn create buoyancy effects due to density changes, releases of thermal energy due to latent heat effects and big changes in chemical concentrations.

- The formation of porphyry copper deposits (copper deposits in igneous rock) at some stage involves the interaction of meteoric groundwaters with saline fluids evolved from magma [Henley and McNabb, 1978]; this is also thought to be the case with other ore deposits. [Cathles, 1977] wrote that salinity strongly affects the ability of hydrothermal solutions to carry minerals and that a proper account of geothermal systems and mineral deposition phenomena must include the effects of salinity on boiling and the dispersal of initially high magmatic salinities by fluid convection. Thus a good knowledge of the phase and thermodynamic properties of the H_2O-NaCl system has the potential to predict deposition environments that can be matched with fluid inclusion data to guide exploration. (Fluid inclusion is where minute amounts of fluid are trapped in a crystal during crystallization. The temperature and composition of the fluid from which the enclosing mineral originated can be estimated from studies of such inclusions.)

1.2 Previous work

There have been many articles written about modelling various aspects of geothermal reservoirs and on the state space and thermodynamic properties of water (H_2O), brine (H_2O-NaCl) and salt (NaCl). The papers which discuss the state space and thermodynamic properties are predominantly written by chemists and the arguments used are chemically complex, especially if the authors are developing theoretically-based equations in order to describe the state space and properties. Such papers will be discussed in the chapters on the state space and the thermodynamic properties. Since we are primarily interested in describing the H_2O-NaCl state space and developing correlations for the thermodynamic properties of brine in such a way that they can be used for numerical simulation purposes, i.e. workable descriptions and correlations, this section will concentrate mainly on those articles where use of the chemists' work is made, i.e. equations and/or data for the state space description and property correlations, in numerical simulation packages.

1.2.1 Water models

As described in [Hayba and Ingebritsen, 1997], some of the earliest work on relatively sophisticated numerical models of heat and mass transport in porous media was that done by [Cathles, 1977] and [Norton and Knight, 1977]. They examined density-driven groundwater flow caused by a cooling pluton. (A pluton is a very hot igneous mass emplaced into the upper 10 km of the Earth's crust.) The fluid in these early models is assumed to be pure water and the conditions extend to supercritical; temperatures up to 800 °C in the case of Cathles and up to 1000 °C in the case of Norton and Knight. Only single-phase conditions are modelled however: Norton and Knight avoid the two-phase region, and Cathles assume that the water in each finite-difference block was either all steam or all liquid. The primary or state variables in their conservation or governing equations are temperature and stream function. (Primary or state variables allow the thermodynamic state of a system to be defined.)

The first multi-phase numerical simulation programs were developed in the late 1970's and early 1980's. The fluid is pure water whose temperatures are subcritical and the phases are single-phase liquid, single-phase steam and two-phase water

(liquid and steam). [Faust and Mercer, 1981] described a three-dimensional multi-phase model called GEOTHER for the flow of pure water in a porous medium whose temperature and pressure ranges are 10–300 °C and 1–175 bars abs. (all pressures in this thesis are given in bars absolute) respectively. Similarly [Pruess, 1983] described the development of a numerical simulation program called MULKOM with temperature and pressure ranges extending to 350 °C and 1000 bars. The big difference between MULKOM and GEOTHER is the choice of primary variables: pressure and enthalpy are used in GEOTHER, pressure and temperature in MULKOM for single-phase liquid and steam, pressure and saturation for two-phase water. The significance of this will be discussed shortly.

One of the first fluid-flow multi-phase simulation programs that used the thermodynamic properties of water where the conditions were supercritical, was the model developed by [Roberts et al., 1987]. Their model is an extension of the Faust and Mercer model discussed earlier and is able to model the multi-phase flow of water whose temperature (T) and pressure (p) ranges extend to 1000 °C and 1000 bars respectively. Another model which has been developed from that of Faust and Mercer, and hence uses pressure and enthalpy as primary variables, is that described by [Hayba and Ingebritsen, 1994]. They developed a multi-phase model called HYDROTHERM which can simulate the transient flow of water up to 1200 °C and 10,000 bars. [Hayba and Ingebritsen, 1997] claimed that previous geothermal models like MULKOM tend to avoid the region very near the critical point of water, i.e. (T, p) = (374.15 °C, 221.2 bars). This is because these previous models use pressure and temperature as their primary variables and using these variables leads to a singularity in fluid heat capacity at the critical point (it goes to infinity). They also stated that there is a similar difficulty with the partial derivatives of density at the critical point. Hayba and Ingebritsen claimed that such difficulties do not occur using pressure and enthalpy as the primary variables and such properties as the density, viscosity and temperature of liquid water and steam merge smoothly to finite values at the critical point.

There has been other work done on these supercritical, multi-phase pure water flows. For example, [Hanano and Seth, 1995] improved the geothermal simulator SIM.FIGS so that the flow of water whose temperatures and pressures extend up to 800 °C and 1000 bars can be modelled. They use the same primary variables as those used in MULKOM. [White and Kissling, 1992] extended MULKOM

to similar temperatures and pressures. They built onto the existing structure of MULKOM by developing a pseudo-saturation line in the T-p plane which extends beyond the critical point. This is a computational device designed to deal with, for example, the scenario of going from single-phase liquid (subcritical) through the supercritical region of the T-p space to single-phase steam (subcritical). This device enables the saturation of the elements to be kept track of during computation, since above the critical point the distinction between liquid and steam disappears, and the values assigned to the saturation variables become arbitrary. [Hayba and Ingebritsen, 1994] tackled this problem by treating supercritical blocks as though they contain two phases with identical properties and gradually decreasing the saturation from 1 (liquid) to 0 (steam) radially in the T-p plane about the critical point.

1.2.2 Water + sodium chloride ± carbon dioxide models

So far we have discussed models in which the geothermal fluid is modelled as a single-component fluid, namely water. We now turn our attention to work done on modelling geothermal systems where the fluid is taken to be a multi-component fluid with water being the main component. Since we are primarily interested in the state space description and the thermodynamic properties of brine, this subsection concentrates on those models where the gas pressure, density, enthalpy and viscosity of the system H_2O-NaCl are described. (We use gas pressures in our delineations or description of the H_2O-NaCl state space.) Articles which describe H_2O-NaCl-CO_2 systems also have information on the properties of H_2O-NaCl-CO_2 and H_2O-CO_2 mixtures, but we will concentrate on the H_2O-NaCl descriptions where they are given.

Subcritical models

Probably the best known geothermal reservoir numerical simulators for modelling multi-component fluids are the successors to MULKOM, i.e. TOUGH [Pruess, 1987] and TOUGH2 [Pruess, 1991]. TOUGH2 is a numerical simulation program for multi-dimensional coupled fluid and heat flows of multi-phase multi-component fluid mixtures in porous and fractured media. [Heat and brine transport are coupled in that, for example, heat transport is caused not only by a temperature

gradient (i.e. density effects), but also by the salt's concentration gradient.] It belongs to the MULKOM family of codes and is a more general version of the TOUGH simulator. TOUGH2 has added capabilities and user features such as the ability to handle different mixtures in the form of equation of state (EOS) modules, e.g. water + carbon dioxide or air or hydrogen. From the point of view of this thesis, we are interested in a new module for TOUGH2 whose development was first described in [Battistelli et al., 1993]. This module, named EWASG (Equation of State for Water, Salt and Gas), is able to handle three-component mixtures: water, sodium chloride and a non-condensible gas (NCG). Sodium chloride is used to simulate the effects of dissolved solids since it is the major component of the dissolved solids, and the NCG can be air, CO_2, CH_4, H_2 or N_2. Water and the NCG components may be present in the liquid and gas phases, while the salt component may be dissolved in the liquid phase and/or precipitated to form a solid salt phase. The treatment of precipitation/dissolution of sodium chloride uses the method employed to treat similar phenomena occurring for water-silica mixtures [Verma and Pruess, 1988]. The solubility of NaCl in the gas phase is neglected. Vapour pressure lowering (VPL) due to salinity, and porosity and permeability reduction from salt precipitation is accounted for. The dependence of density, viscosity and enthalpy of brine on salt concentration is also accounted for by EWASG.

[Battistelli et al., 1995] enhanced EWASG by including VPL due to capillary pressure effects. Previously EWASG considered only salinity-induced VPL. As discussed in [Battistelli et al., 1997], the vapour pressure of water in a porous medium at a given temperature tends to be lower than that above a flat surface of bulk water. This VPL for a porous medium is caused by capillary and vapour adsorption effects, which [Battistelli et al., 1997] refer to as suction pressure effects. According to [Battistelli et al., 1995], these suction pressure effects depend mainly on the capillary pressure. [As described in [Bear and Bachmat, 1991], when two immiscible fluids are in contact, a discontinuity in pressure exists across the interface separating them. This difference in pressure is called capillary pressure, p_{cap}, which depends on the surface tension between the two fluids and S_ℓ, the liquid saturation. Surface tension, in turn, is a function of temperature, T, and chemical composition, C. Therefore $p_{cap} = p_{cap}(S_\ell, T, C)$. Vapour adsorption is where, for example, liquid molecules adhere onto the surfaces of the solid surrounding the pore spaces despite the fact that thermodynamic conditions are such that liquid molecules

could not exist in free space (pore space), e.g. superheated vapour exists in the free space.] According to [Battistelli et al., 1997], VPL phenomena are believed to be of major importance in determining the in-place and extractable fluid reserves of vapour-dominated reservoirs. Other enhancements to TOUGH2 include that developed by [White, 1995], which enable the reactive chemical transport of dissolved solids and non-condensible gases to be simulated. [Kissling et al., 1996] used this extension to model the Wairakei Geothermal Field. [Oldenburg et al., 1995] used TOUGH2 with a newly developed dispersion module (T2DM) in order to investigate double-diffusive convection (free convection with two buoyancy sources of different diffusivities) in relation to hypersaline geothermal systems.

As described in [Battistelli et al., 1993], EWASG uses the theoretical equations of [Haas, 1976] in order to calculate the density and vapour (gas) pressure of vapour-saturated brines. [Vapour-saturated brine refers to brine on the liquid boundary (surface) of the two-phase region (liquid and gas) of the H_2O-NaCl state space.] The brine enthalpy on this two-phase liquid surface is calculated using the correlation of [Michaelides, 1981] based on the thermodynamic data of [Silvester and Pitzer, 1976]. The viscosity on this surface is estimated using an equation from [Chierici et al., 1981] which applies a correction as a function of salt mass fraction (X) to the viscosity of saturated water. The effect of pressure on brine density, enthalpy and viscosity is estimated using the assumption that brine compressibility is the same as that of pure water from the pressure on this two-phase liquid surface to the current (higher) pressure. The T and X ranges of validity for these three properties are: $75 \leq T \leq 325$ °C (density), $100 \leq T \leq 300$ °C (enthalpy), $0 \leq X \leq 0.30$ (viscosity and some density values), $0 \leq X \leq$ halite or NaCl saturation (vapour pressure and some density values). The enthalpy of pure NaCl is calculated by integrating the equation of heat capacity at constant pressure given in [Silvester and Pitzer, 1976], where $25 \leq T \leq 800$ °C. The density of pure salt is taken to be constant. No mention is made of the validity range of X for the enthalpy, the T validity range for the viscosity, or the viscosity of pure sodium chloride. Halite saturation on the two-phase liquid surface is calculated using an equation due to Potter quoted in [Chou, 1987], who recommended the use of this equation from 0 to 382 °C.

An updated description of EWASG is given in [Battistelli et al., 1997] where the correlations for the thermodynamic properties of H_2O-NaCl-CO_2 are partially

revised in order to extend their range of application over the T-p-X space of interest. The range of applicability is now: temperatures from 100 to 350 °C, total pressure up to 800 bars (partial pressure of CO_2 up to 100 bars), and salt mass fraction up to halite saturation. The lower temperature limit of 100 °C is a result of a correlation used for brine enthalpy, otherwise it could be less than 10 °C.

As they did originally in 1993, [Battistelli et al., 1997] have used the equations of [Haas, 1976] for density and vapour pressure values of brine on the two-phase liquid surface. However this time they have used them outside their range of validity as specified by Haas, so that the validity ranges for T and X are now $0 \leq T \leq 350$ °C and $0 \leq X \leq$ halite saturation for both the density and vapour pressure. These extended correlations compare favourably with data from [Potter and Brown, 1977] (density) and [Tanger and Pitzer, 1989] (vapour pressure), see Figures 2 and 3 of [Battistelli et al., 1997]. In order to extend the temperature range of the compressed brine density (i.e. where the pressure is greater than that on the two-phase liquid surface) to 350 °C, Battistelli et al. use a correlation for brine compressibility taken from [Andersen et al., 1992]. This correlation gives values which also closely match the experimental data of Potter and Brown for $X = 0.25$, $5 \leq T \leq 350$ °C and pressures extending from that on the two-phase liquid boundary to 800 bars—see Figure 5 of [Battistelli et al., 1997]. The density of pure sodium chloride, previously taken to be constant, is now given as a function of T and p. Halite saturation and the enthalpy of brine and pure salt are calculated as was done for the previous version of EWASG [Battistelli et al., 1993], although this new EWASG version also has a look-up table for brine enthalpy values on the two-phase liquid surface. These values are taken from [Phillips et al., 1981] and cover $0 \leq T \leq 300$ °C and $0 \leq X \leq 0.25$ [Battistelli, 1998]. For the dynamic viscosity of brine on the two-phase liquid surface and compressed brine (aqueous solutions), the new version of EWASG uses a correlation from [Phillips et al., 1981] which is valid for $10 \leq T \leq 350$ °C, $0 \leq X \leq 0.23$ and $0 < p \leq 500$ bars. [Battistelli et al., 1997] concluded by recommending that work should be done in improving the accuracy of the calculation of the brine properties for $X > 0.25$ and in developing a new correlation for brine enthalpy that is valid for $T < 100$ °C.

Other authors have also modelled subcritical H_2O-NaCl-CO_2 systems but used different simulators. For example, [Andersen et al., 1992] presented a pVT model for H_2O-NaCl-CO_2 systems (V is the specific volume = 1/density). The range

of applicability of their model is: temperatures from 24 to about 371 °C, pressures from 1 to 345 bars and salt mass fractions up to 0.30. The possible precipitation of salt is not accounted for in their model. Their correlation for the vapour pressure of brine on the two-phase liquid boundary accurately reproduces data whose temperature extends to about 400 °C and salt mass fraction range from 0 to 0.30. This data is taken from [Haas, 1976], [Pitzer et al., 1983] and [Bischoff and Pitzer, 1989]. Andersen et al. discussed the liquid-phase density of brine. It is not clear what is meant by 'liquid-phase' here. Do they mean the density on the liquid part of the two-phase boundary or are they referring to brine whose pressure is greater than the pressure on the two-phase boundary and is therefore wholly liquid? They developed a correlation for the liquid-phase density of brine based partly on some experimental data from [Potter and Haas, 1978]. This correlation incorporates a compressibility factor (this was also used by [Battistelli et al., 1997], see above). In Figure 9 of their paper, Andersen et al. compared densities of brine solutions calculated from their correlation with some data where $10 \leq T \leq 426$ °C, $0 \leq X \leq 0.25$ at water saturation pressure, but do not mention where the data was obtained. Andersen et al. developed a correlation for the liquid-phase enthalpy of brine based on the theoretically-calculated data of [Haas, 1976]. Their correlation compares favourably with Haas's data and also with that of [Tanger and Pitzer, 1989] for temperatures up to 400 °C and $0 \leq X \leq 0.30$. According to [Battistelli et al., 1997], these correlations have been packaged into an equation of state (EOS) module and included in a simulator called TETRAD, which has been used to study the effects of salt on the formation of a high-temperature reservoir in vapour-dominated systems.

[Alkan et al., 1995] developed correlations for the thermodynamic properties of H_2O-NaCl-CO_2 mixtures at subcritical temperatures, and these were then used in a model based on the general material-energy balance equation given by [Whiting and Ramey, 1969] for geothermal reservoirs. For the density of salt solutions (presumably by 'solutions' they mean aqueous or liquid solutions), they use an equation given by [Wahl, 1977] for an 'average' brine (nearly equal to NaCl solution). For the enthalpy of NaCl solutions, they develop an equation that is based on data obtained from Wahl. The viscosity is given by an equation which multiplies the viscosity of water by a quadratic polynomial in X. Test runs on three geothermal

reservoirs are made.

An EOS module for H_2O-NaCl-CO_2 systems was also developed by [Pritchett, 1993] which implements salt precipitation and associated permeability changes and is being used in the STAR reservoir simulator.

Models which extend to supercritical temperatures and pressures

[McKibbin and McNabb, 1993] described a model for the T-p-X state-space of a H_2O-NaCl system whose temperature and pressure ranges include those that are typical of a deep geothermal system, i.e. supercritical. They give a mathematical description of the T-p-X state space which enables eight different regions in the state space to be delineated, showing where gas, liquid and two-phase brine flows may exist as well as regions where solid sodium chloride may be either deposited or dissolved while in equilibrium with saturated brines. Their description or correlations are based mainly on experimental data from [Sourirajan and Kennedy, 1962] with a small number of data points from [Haas, 1976] also being used. McKibbin and McNabb take the critical point of pure NaCl to be (T, p) = (1075 °C, 930 bars), as quoted in [Bowers and Helgeson, 1983]. The T, p and X ranges of their state space description are $0 < T < 1075$ °C, $0 < p < 1600$ bars and $0 < X < 1$. McKibbin and McNabb also describe the conservation equations of mass, linear momentum (Darcy's law) and energy, which are used to model the flow of brine and heat through a geothermal system. In [McNabb et al., 1993] and [McKibbin and McNabb, 1995a] they implemented these equations and state space description in models whose temperatures and pressures extended to supercritical values. The 1993 paper tested a two-dimensional model of thermal convection over a mid-ocean ridge magmatic hot plate and the 1995 paper described some simulations of one-dimensional (vertical), steady (fluid flow does not change with time) flows of brine. Both papers use the enthalpy and viscosity of pure water for the entire state space. For density, they use that of water for $T \leq 374.15$ °C (the critical temperature of water) and $p < p_{w\ sat}(T)$, the saturation pressure of water. For the rest of the state space they used a density subroutine based on data from [Haas, 1976], [Potter and Brown, 1977] and [Bischoff, 1991]. Unlike EWASG, in the 1-D vertical flow simulations, the permeability of the fluid-filled formation remains constant over time and space, since it is assumed that any salt precipitate causes the rock to expand in such a way that the effective porosity and permeability

remain constant.

[McNabb et al., 1993] commented that they await better data to adequately describe the brine enthalpies and viscosties over the full range of the thermodynamic variables, and [McKibbin and McNabb, 1995a] concluded by writing that 'Further work continues on correlations and calculation subroutines to improve the estimation of brine properties such as density, enthalpy and viscosity, and to use these in 2-D and 3-D simulations.'

1.3 This work—an outline

Much work has been done on the modelling of that part of geothermal systems where the temperatures are less than the critical value for water, i.e. 374.15 °C. These parts are relatively shallow and are commonly known as geothermal reservoirs. We are also interested in the deeper parts of geothermal systems, i.e. those parts which lie below the reservoirs and above magmatic heat, fluid and chemical sources. Since the temperature and pressure of the magma surface are very much supercritical (well above the critical temperature and pressure of water), the temperatures and pressures of these deeper parts of geothermal systems are probably supercritical too. Since the main solute component of geothermal fluids is NaCl, it is used to represent the effects of the solutes and we model the geothermal fluid as brine (H_2O-NaCl). Our aim in this thesis is to describe the H_2O-NaCl state space and develop correlations for the thermodynamic properties of density (ρ), specific enthalpy (h) and dynamic viscosity (μ) of brines in such a way that they can be used for numerical simulation purposes, i.e. workable descriptions and correlations. These thermodynamic properties are required in order to solve the conservation equations which are used to mathematically model the heat and mass transfer processes in a geothermal system.

This thesis updates the work done on the brine state space as described in [McKibbin and McNabb, 1993], by revising the correlations that delineate the state space in the light of more recent data. The data used for this revision is based on more up-to-date and comprehensive data sets than that used by McKibbin and McNabb. This means that the boundaries of the state space, which these correlations describe, and the regions are better established than previously. The correlations for the three thermodynamic properties of brine are new because they not

only cover subcritical temperatures, but also supercritical temperatures and in fact cover the entire brine state space. Previous work on these properties for brine such as that described in the TOUGH2 module EWASG, see [Battistelli et al., 1997], cover subcritical temperatures only. There has been work done on these properties at supercritical temperatures, but the fluid used has been water. As discussed previously, the fluid found in geothermal systems is not pure water, but rather a complex mixture of water, dissolved solids (the principal one being NaCl) and non-condensible gases. Therefore developing correlations for the density, enthalpy and viscosity of H_2O-NaCl or brine enables more accurate modelling of the flow of mass and heat through geothermal systems. McNabb et al. and McKibbin & McNabb ran some simulations which are described in [McNabb et al., 1993] and [McKibbin and McNabb, 1995a]. For these simulations they used a subroutine for the density of brine that extended to supercritical temperatures. However this subroutine did not cover all the T-p-X brine state space and this thesis does not use their subroutine.

As will be seen, some of the published data for the pure H_2O-NaCl system have diverging trends. It may be possible to get a coherent, self-consistent set of data for the pure H_2O-NaCl system, but until more work is done on reconciling the divergent trends of some of the data, we will use data sets that are self-consistent with one another, since as mentioned above, we wish to develop workable correlations. While our correlations may not fit the data as well as we would like, especially at higher temperatures and pressures, qualitatively they are accurate and at $X = 0$ they match the data for water.

Chapter 2 gives details of our model. This includes the model fluid that is used, the conceptual model and the mathematical model which includes the conservation equations. Chapter 3 presents an updated version of the H_2O-NaCl T-p-X state space description that was first given in [McKibbin and McNabb, 1993]. It is explained how the state space description accounts for salinity-induced vapour pressure lowering. The development of the new correlations for ρ, h and μ of brine are described in Chapter 4. The case of 1-D steady vertical flows is described in Chapter 5 and we test our correlations for the state space delineations and the thermodynamic properties on such flows. The actual correlation formulae for the state space delineations and thermodynamic properties can be found in the Appendices.

Chapter 2

The model

2.1 The model fluid

In order to provide quantitative modelling of the heat and mass flow processes of geothermal fluids using conservation equations, definitions of the properties of these fluid systems are required. Since the composition of such fluids is not accurately known, especially at depth, a first step forward is to propose a model geothermal fluid based on the properties of the major components of the fluids. As discussed in Section 1.1, the main solute component is NaCl and the main gas component is CO_2. It would seem sensible, therefore, to design a model brine which is an approximation to a pure NaCl-H_2O system and where the effects of gas are approximated by CO_2. This model brine would not exactly match the data for pure systems. Such is the approach in this thesis. We are trying to model a geothermal fluid based qualitatively and, to a great extent, quantitatively on the system H_2O-NaCl. Since the model is approximate it need not exactly match the data at every point; however it must match for pure water when there is no dissolved salt (when $X = 0$) and the properties of water are well known.

2.2 The conceptual model

Our model fluid (brine) moves through a geothermal system by way of spaces and fractures in the rock, i.e. the fluid is flowing in a porous medium, in fact the geothermal system is treated as a fluid-saturated permeable medium. The remainder of this section is adapted from material found in [Bear and Bachmat, 1991] and

[Bear and Verruijt, 1994].

A porous medium domain consists of a void space and a solid matrix. The void space is occupied by one or more fluid phases. The solid matrix is distributed throughout the porous medium. This implies that any sample of sufficiently large volume (referred to as an Arbitrary Elementary Volume or AEV), taken at different places within the domain, will always contain a solid phase.

In principle, the flow of a fluid in a porous medium may be treated at the microscopic level, where the attention is focused at what happens at a point within the fluid. For example, for a single-phase fluid that occupies the entire void space, we can use the Navier-Stokes equations and solve them within the fluid domain, subject to boundary conditions on the solid-fluid interface that bounds this domain. Similarly for a two-phase fluid that occupies the void space. However, this approach is usually impractical due to our inability to describe the complex configuration of these boundaries. Moreover, even if we could solve for values of state variables such as pressure at the microscopic level, we could not verify these solutions by measurements at this level. To avoid these difficulties, another level of description is needed. This is the macroscopic level, at which quantities can be measured and boundary-value problems can be solved. To obtain the description of the flow at this level, the continuum approach is adopted. According to this approach, the real porous medium, in which each phase (solid or fluid) occupies only a portion of the AEV mentioned before, is replaced by a fictitious model in which each phase is regarded as a continuum that fills up the entire AEV. A set of overlapping and possibly interacting continua are therefore obtained for each AEV. For each of these continua, averaged values can be taken over the AEV and assigned to its centroid, regardless of whether the latter falls within the solid or within one of the fluids that occupy the void space. By traversing the entire porous medium domain with a moving AEV, fields of macroscopic variables, which are differentiable functions of the space coordinates, are obtained. Therefore, the macroscopic continuum model eliminates the need for specifying the microscopic configuration of the individual phases and enables the solution of problems of flow through porous media by appropriate mathematical techniques. The configuration of the void-solid and interphase boundaries within the averaging volume, as well as the effect of the conditions that prevail on them, appear in the macroscopic description or model in the form of coefficients, which are usually obtained experimentally.

The main drawback in using an AEV is that every averaged value such as the density or pressure must be accompanied by a label that specifies the volume over which this average was taken. To solve this problem, a universal procedure is needed that is applicable to all porous media and has the phases, components and their properties varying continuously. This universal averaging volume is known as the Representative Elementary Volume (REV)—see Figure 2.1. If d is a characteristic of the REV, ℓ a length characterising the microscopic structure of the void space and L a characteristic length of the porous medium domain, then the REV must be chosen such that $\ell \ll d \ll L$.

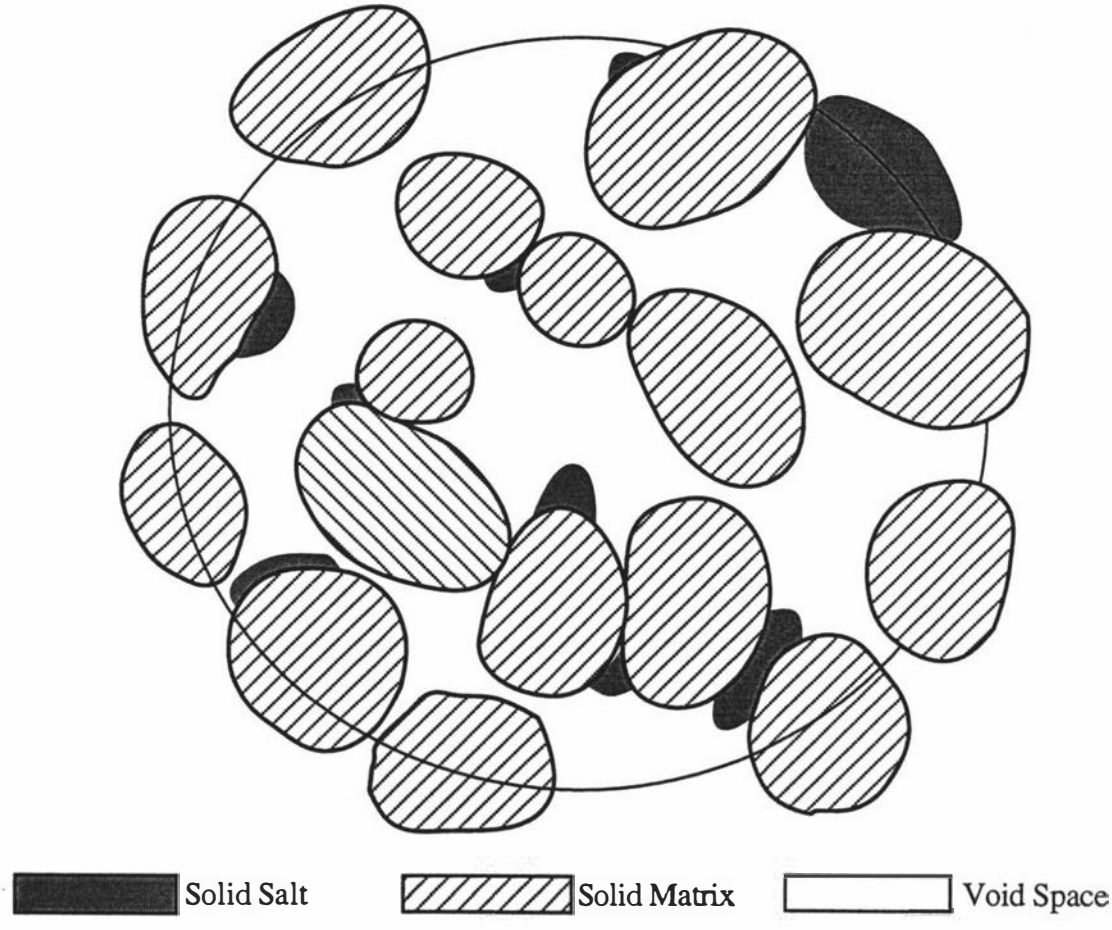

Figure 2.1: Schematic of a planar cross-section through a Representative Elementary Volume (REV), adapted from [Bear and Bachmat, 1991].

2.3 The mathematical model

In order to describe the flow of brine and heat through such a system, a model mathematical description must be formulated. This is done using equations of mass, linear momentum and energy conservation. Solving these equations enables the determination of such quantities as T and p gradients at a point in the flow, and T, p, X profiles in time and space.

The model described in this work does not include vapour pressure lowering (VPL) due to capillary pressure effects, as the subcritical module EWASG of TOUGH2 does—see Subsection 1.2.2. Vapour adsorption also causes VPL, but the VPL due to this is believed to be small compared with that due to capillary pressure effects. Neither the model described here nor EWASG incorporate VPL due to vapour adsorption effects; however the model of this work does include VPL due to salinity and this is described in Chapter 3 where the H_2O-NaCl state space is discussed. The importance of VPL due to capillary pressure and vapour adsorption remains unclear, since [Battistelli et al., 1993] stated that, 'salinity-induced VPL effects are likely to be more important in the depletion of vapour-dominated reservoirs than capillarity/adsorption induced effects'. Then in [Battistelli et al., 1997], they refer to a paper by [Satik et al., 1996] which says that the VPL associated with capillarity/adsorption effects (or suction pressure effects) are believed to be of major importance in determining the in-place and extractable fluid reserves of vapour-dominated reservoirs.

Furthermore, it is assumed here that the rock matrix is solid and stationary for all temperatures, even for those temperatures which are very much supercritical and found at depth in geothermal systems. However it is likely that at these higher temperatures, the rock matrix is no longer solid or stationary. For such a deformable matrix, there is strong coupling among such factors as the work due to pressure, body and surface forces, energy due to viscous dissipation and also that of chemical reactions. (Permeability may also be seriously compromised.) In order to fully model what is happening in geothermal systems, especially at depth, these factors need to be incorporated into the conservation of energy equation (see Subsection 2.3.2). Whilst these terms may be important, for the purposes of this thesis, we are interested in the salt effects due to modelling geothermal fluids as brine (as opposed to pure water).

2.3.1 Derivation of conservation equations

This subsection is adapted from material found in [Bear and Bachmat, 1991].

If we consider a single-phase continuum at the microscopic level, the description of a process undergone by a quantity such as mass, linear momentum or energy starts with the formulation of a balance or conservation equation for that quantity in the neighbourhood of an arbitrary point, P, within the phase. The point is defined by its position vector, $\mathbf{x}$. The equation can be derived in several ways. One way is to use the Eulerian approach in which the attention is focused on a fixed (arbitrary) finite domain, V, referred to as a control volume, bounded by a closed surface, S, see Figure 2.2.

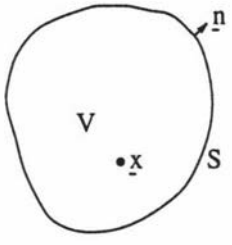

Figure 2.2: A control volume V bounded by a surface S.

For example, the instantaneous balance of energy (denoted by A_e) within V can be expressed by:

Rate of accumulation of A_e within V	=	Net influx of A_e into V through S	+	Net rate of production of A_e within V
(a)		(b)		(c)

(a) The rate of increase in the amount of A_e per unit volume within V is expressed by:

$$\frac{\partial}{\partial t}\int_V A_e \, dV = \int_V \frac{\partial A_e}{\partial t} \, dV$$

The exchange of integration and differentiation is allowed because the boundary of V is fixed.

(b) The net influx (= total influx minus total efflux) of A_e into V through S is given by:

$$-\int_S \mathbf{Q}_e \cdot \mathbf{n}\, dS$$

where $\mathbf{Q}_e$ is the energy flux per unit area and $\mathbf{n}$ is an outward-pointing unit normal vector.

(c) The net rate of production of A_e from sources within V is expressed by:

$$\int_V q_e\, dV$$

where q_e is the rate of production, or the rate of injection of energy per unit volume within V (withdrawal is a negative value).

Altogether, the balance of A_e within V is expressed by:

$$\int_V \frac{\partial A_e}{\partial t}\, dV = -\int_S \mathbf{Q}_e \cdot \mathbf{n}\, dS + \int_V q_e\, dV$$

Applying Gauss's or the divergence theorem to the first term on the right hand side and since V is an arbitrary control volume, we obtain:

$$\frac{\partial A_e}{\partial t} + \nabla \cdot \mathbf{Q}_e - q_e = 0 \tag{2.1}$$

The analogous equations to Equation (2.1) for mass and linear momentum are:

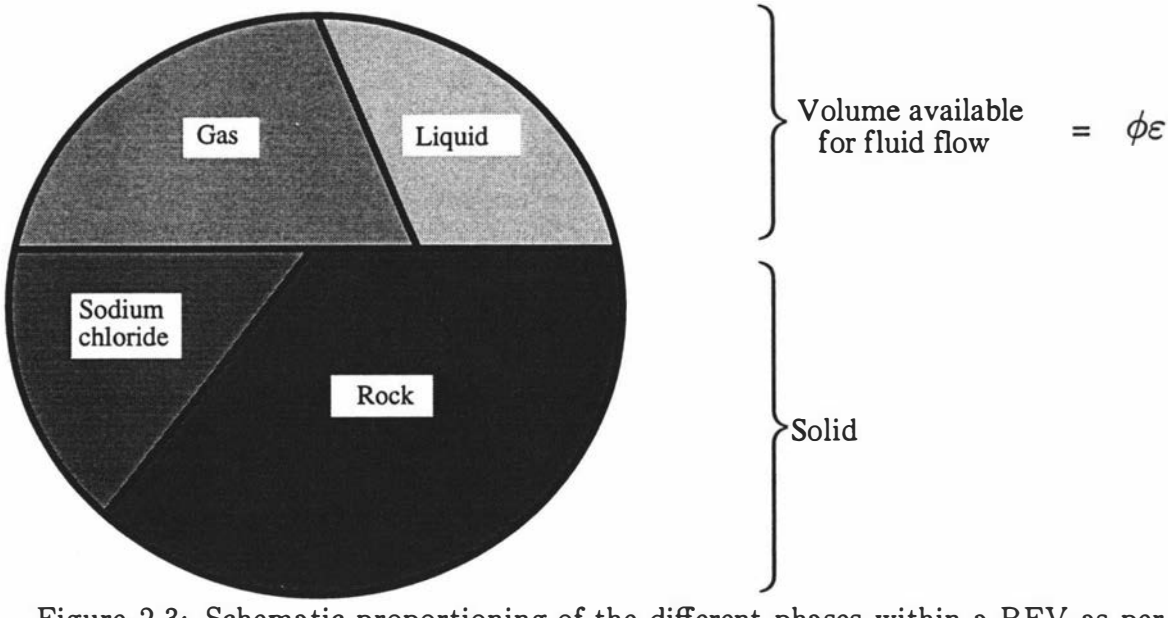

Figure 2.3: Schematic proportioning of the different phases within a REV as per the continuum approach, adapted from [McKibbin and McNabb, 1998].

$$\frac{\partial A_i^\gamma}{\partial t} + \nabla \cdot \mathbf{Q}_i^\gamma - q_i^\gamma = 0 \tag{2.2}$$

where i = mass (m) or linear momentum (lm) and
γ = water (w) or sodium chloride (c)

2.3.2 The conservation equations

We now switch from the microscopic level to the macroscopic one by applying averaging rules to Equations (2.1) and (2.2) in order to obtain the macroscopic conservation equations of energy, mass and linear momentum as described in [McKibbin and McNabb, 1993]. Figure 2.3 shows a REV in which the continuum approach (discussed in Section 2.2) has been implemented, i.e. each phase (solid, liquid or gas) is regarded as a continuum, uniformly distributed within the REV. Figure 2.3 shows a schematic proportioning of the phases within a REV. It is assumed that the phases are in local thermal and chemical equilibrium.

Conservation of mass

From Equation (2.2), we have for each component:

$$\mathrm{H_2O}: \quad \frac{\partial A_m^w}{\partial t} + \nabla \cdot \mathbf{Q}_m^w - q_m^w = 0 \tag{2.3}$$

$$\mathrm{NaCl}: \quad \frac{\partial A_m^c}{\partial t} + \nabla \cdot \mathbf{Q}_m^c - q_m^c = 0 \tag{2.4}$$

where A_m^γ is the mass per unit volume of each component γ ($\gamma = w$ or c). $\mathbf{Q}_m^\gamma$ is the mass flux per unit area of component γ and q_m^γ is the rate of production, or rate of injection (positive) or withdrawal (negative) of mass per unit volume of component γ.

The mass fraction of salt (X) is related to A_m^γ as follows:

$$X = \frac{A_m^c}{A_m^c + A_m^w} \tag{2.5}$$

If we consider a REV, see Figures 2.1 and 2.3, then the porosity (ϕ) is the ratio of the volume of pore space to the total volume of the REV. The volume fraction of the pore space occupied by the fluid is denoted by ε and is called the voidage. For example, if there is salt precipitated onto the rock (the walls of the pore space),

then $\varepsilon < 1$, otherwise $\varepsilon = 1$. Therefore, the volume available for fluid-flow within a REV, known as the effective porosity, is given by the product $\phi\varepsilon$—see Figure 2.3. The volume fraction of the pore space that is occupied by the solid sodium chloride precipitate is $\phi(1-\varepsilon)$.

The volume fraction of the liquid and gas phases within a REV is given by $\phi\varepsilon S_\ell$ and $\phi\varepsilon(1-S_\ell)$ respectively. S_ℓ, the liquid saturation, is the volume fraction of the fluid occupied by the liquid phase.

The mass of water per unit volume in the liquid and gas phases are $\phi\varepsilon S_\ell(1-X_\ell)\rho_l$ and $\phi\varepsilon(1-S_\ell)(1-X_g)\rho_g$, so that:

$$A_m^w = \phi\varepsilon[S_\ell(1-X_\ell)\rho_\ell + (1-S_\ell)(1-X_g)\rho_g] \tag{2.6}$$

where X_j is the sodium chloride mass fraction within each phase j [j = liquid (ℓ) or gas (g)], and ρ_j is the density of the j phase.

Similarly, the mass of sodium chloride per unit volume in the liquid and gas phases are $\phi\varepsilon S_\ell X_\ell\rho_\ell$ and $\phi\varepsilon(1-S_\ell)X_g\rho_g$. The mass of solid NaCl precipitate per unit volume is given by $\phi(1-\varepsilon)\rho_c$, where ρ_c is the density of solid salt. Therefore we have:

$$A_m^c = \phi\varepsilon[S_\ell X_\ell\rho_\ell + (1-S_\ell)X_g\rho_g] + \phi(1-\varepsilon)\rho_c \tag{2.7}$$

Substituting for A_m^c and A_m^w in Equation (2.5) gives:

$$X = \frac{(1-\varepsilon)\rho_c + \varepsilon[S_\ell X_\ell\rho_\ell + (1-S_\ell)X_g\rho_g]}{(1-\varepsilon)\rho_c + \varepsilon[S_\ell\rho_\ell + (1-S_\ell)\rho_g]} \tag{2.8}$$

The total mass of material per unit volume (A_m) of the fluid-saturated porous medium consists of the sum of the respective quantities for the rock matrix (A_m^r), sodium chloride and water:

$$\begin{aligned} A_m &= A_m^r + A_m^c + A_m^w \\ &= (1-\phi)\rho_r + \phi\{\varepsilon[S_\ell\rho_\ell + (1-S_\ell)\rho_g] + (1-\varepsilon)\rho_c\} \end{aligned} \tag{2.9}$$

where ρ_r is the density of the solid rock matrix.

Conservation of linear momentum

In the macroscopic continuum approach, subject to certain assumptions, the averaged linear momentum balance equation becomes what is known as Darcy's law,

i.e. fluid fluxes are assumed to be driven by gravity and pressure gradients, and are governed by the two-phase Darcy's law for flow in a porous medium. Dispersion of salt is assumed small compared with advection transport (advective flux is carried by the fluid flow) and is ignored. [Dispersion, which occurs at the microscopic level = mechanical dispersion + molecular diffusion. Because of the shape of the interconnected pore spaces, the streamlines fluctuate in space with respect to the mean direction of flow giving rise to mechanical dispersion. This phenomenon together with molecular diffusion causes the spreading of any initial close grouping of salt particles.]

The mass fluxes per unit area (cross-sectional area) are given for the water and sodium chloride by the sum of the mass fluxes associated with each fluid phase:

$$\begin{aligned} \mathbf{Q}_m^w &= \mathbf{Q}_{m\ell}^w + \mathbf{Q}_{mg}^w = (1 - X_\ell)\mathbf{Q}_{m\ell} + (1 - X_g)\mathbf{Q}_{mg} \\ \mathbf{Q}_m^c &= \mathbf{Q}_{m\ell}^c + \mathbf{Q}_{mg}^c = X_\ell \mathbf{Q}_{m\ell} + X_g \mathbf{Q}_{mg} \end{aligned}$$

The gravity- and pressure-driven mass fluxes corresponding to the liquid and gas phases, $\mathbf{Q}_{m\ell}$ and $\mathbf{Q}_{mg}$, are given by Darcy's law applied to each phase separately, as follows:

$$\mathbf{Q}_{m\ell} = \mathbf{Q}_{m\ell}^w + \mathbf{Q}_{m\ell}^c = k_{r\ell}\frac{k}{\nu_\ell}(-\nabla p + \rho_\ell \mathbf{g}) \tag{2.10}$$

$$\mathbf{Q}_{mg} = \mathbf{Q}_{mg}^w + \mathbf{Q}_{mg}^c = k_{rg}\frac{k}{\nu_g}(-\nabla p + \rho_g \mathbf{g}) \tag{2.11}$$

where k is the permeability of the fluid-filled porous medium and k_{rj} is the relative permeability for the j phase. (The k_{rj} are permeability reduction factors which are dependent on S_ℓ only and are the coefficients that are discussed in Section 2.2—they are introduced in the passage from the microscopic level of description to the macroscopic one.) ν_j is the kinematic viscosity for the j phase, p is the pressure and $\mathbf{g}$ is the acceleration due to gravity. The total fluid flux per unit area is given by:

$$\mathbf{Q}_m = \mathbf{Q}_{m\ell} + \mathbf{Q}_{mg}$$

Conservation of energy

Recalling the discussion earlier in this section about the assumptions made for the simple model described in this chapter, from Equation (2.1) we have:

$$\frac{\partial A_e}{\partial t} + \nabla \cdot \mathbf{Q}_e - q_e = 0 \tag{2.12}$$

where, using a method similar to that which resulted in Equation (2.9) for mass, the energy per unit volume of the fluid-saturated porous medium is given by,

$$A_e = (1-\phi)\rho_r u_r + \phi\{\varepsilon[S_\ell \rho_\ell u_\ell + (1-S_\ell)\rho_g u_g] + (1-\varepsilon)\rho_c u_c\} \quad (2.13)$$

where u_r, u_ℓ, u_g and u_c are the specific internal energies for the rock matrix, liquid and gas phases, and solid sodium chloride. $\mathbf{Q}_e$, the energy flux per unit area, is given by the sum of the energy fluxes corresponding to the flow of each phase and that due to heat conduction, as follows:

$$\mathbf{Q}_e = \mathbf{Q}_{m\ell} h_\ell + \mathbf{Q}_{mg} h_g - K\nabla T \quad (2.14)$$

where $\mathbf{Q}_{m\ell}$ and $\mathbf{Q}_{mg}$ are defined above, h_j is the specific enthalpy of the j fluid phase and T is the temperature. K is the thermal conductivity of the saturated rock formation and depends on both the conductivity of the rock (K_r) and that of the fluid (K_f): $K = (1-\phi)K_r + \phi K_f$. Since ϕ is usually small however, the value of K depends mainly on K_r and is assumed to be constant.

Solution of the above equations gives T, p, X profiles of the system at different times and positions in space. The partial differential equations are nonlinear since the thermodynamic properties of ρ, h and ν are functions of T, p and X, and therefore the equations have to be solved numerically. The details of the numerical solution will not be discussed here, but in Chapter 5 we will describe the solution details of the special case of 1-D (vertical) steady fluid flow.

Chapter 3

The H_2O-NaCl state space

3.1 Introduction

The T-p state space for pure water consists of four regions, namely: single-phase liquid, single-phase gas (steam), two-phase (liquid and gas coexist) and a supercritical region (no distinct phases). The two-phase region consists of a line in the T-p plane and separates the two single-phase regions. On this line, called the saturation line, determination of T (or p) uniquely specifies p (or T), i.e. T and p are dependent. If $T > 374.15$ °C or $p > 221.2$ bars, then the water is supercritical. Pure water models of geothermal fluid that use T and p as their primary variables, calculate the thermodynamic properties of water according to which region the (T, p) value (or state point) falls in. We adopt a similar approach with our brine model. However adding salt to water means that the state or phase space becomes considerably more complicated—the 2-D T-p plane for water becomes a 3-D T-p-X volume in the case of brine.

Papers such as [Bischoff and Pitzer, 1989] and [Anderko and Pitzer, 1993] show precise sketches of some aspects of H_2O-NaCl T-p-X state space delineations that are based on their data. No correlation formulae are given in such papers, therefore making them difficult to use for modelling purposes. This chapter develops correlations for the brine state space which delineate the state space into regions. These regions correspond to the brine being in different phases which include single-phase liquid, single-phase gas, two-phase (liquid + gas), supercritical (neither liquid nor gas) and regions where saturated brine (liquid or gas) is in equilibrium with solid sodium chloride precipitate. Given a particular T-p-X value, or state point, the

correlations enable this state point to be quickly linked to the appropriate region. For our brine model we have retained the eight-region brine state space first described in [McKibbin and McNabb, 1993]. The correlations that delineate the state space and define the boundaries for the eight regions are similar to those of McKibbin and McNabb with some exceptions, e.g. the critical point and saturation line for NaCl and the shape of the curve for $X_{g\ SAT}$ (the mass fraction of NaCl in the halite-saturated gas on the three-phase surface). However the correlations described in this chapter are based on more up-to-date and comprehensive sets of data than those used by McKibbin and McNabb, and therefore, I believe, place the eight-region brine state space and the boundaries for these regions on a 'firmer footing'.

The H_2O-NaCl state space has three different basic 'configurations' which correspond to three different temperature ranges, namely $0 < T \leq 374.15$ °C (see Figure 3.1 (a)), $374.15 < T < 800$ °C (see Figure 3.1 (b)) and $T \geq 800$ °C (see Figure 3.1 (c)). $T = 374.15$ °C is the critical temperature of water and (T, p) = (800 °C, 0 bars) is the triple point of NaCl. $p_{SAT}(T)$ refers to the three-phase (liquid, gas and solid) surface of brine (see Figure 3.1), whereas $p_{w\ sat}(T)$, often referred to in the literature as $p_{sat}(T)$, is the saturation pressure of pure water. $p_{SAT}(T) \neq p_{w\ sat}(T)$ or $p_{sat}(T)$. For $X = 0$ (pure water) and $0 < T \leq 374.15$ °C (see Figure 3.1 (a)), $p_{w\ sat}(T) = p_{CRIT}(T)$, the critical pressure of brine. For $374.15 < T < 800$ °C, see Figure 3.1 (b), the two-phase region (Region 5) becomes unattached from the left-hand side ($X = 0$) of Figure 3.1 (a) and $p_{w\ sat}(T)$ no longer equals $p_{CRIT}(T)$ at $X = 0$. For $T \geq 800$ °C, Region 5 goes from being above the three-phase surface, $p_{SAT}(T)$, for $T < 800$ °C, to being above the saturation line for pure sodium chloride which is given by $p_{c\ sat}(T)$, see Figure 3.1 (c). Also for $T \geq 800$ °C, the three-phase surface and the saturated gas region (Region 3) are replaced by the two-phase saturation line for NaCl ($p_{c\ sat}(T)$) and an unsaturated gas region (Region 7) respectively.

The boundary between Region 1 and Regions 2 & 6, see Figure 3.1 (a) and (b), is vertical since it is assumed that it is independent of pressure, see Section 3.5. The three-phase surface given by $p_{SAT}(T)$, see Figure 3.1 (a) and (b), is horizontal since for a given T, there is a unique value of p where saturated brine gas plus solid NaCl is in equilibrium with saturated brine liquid plus solid NaCl.

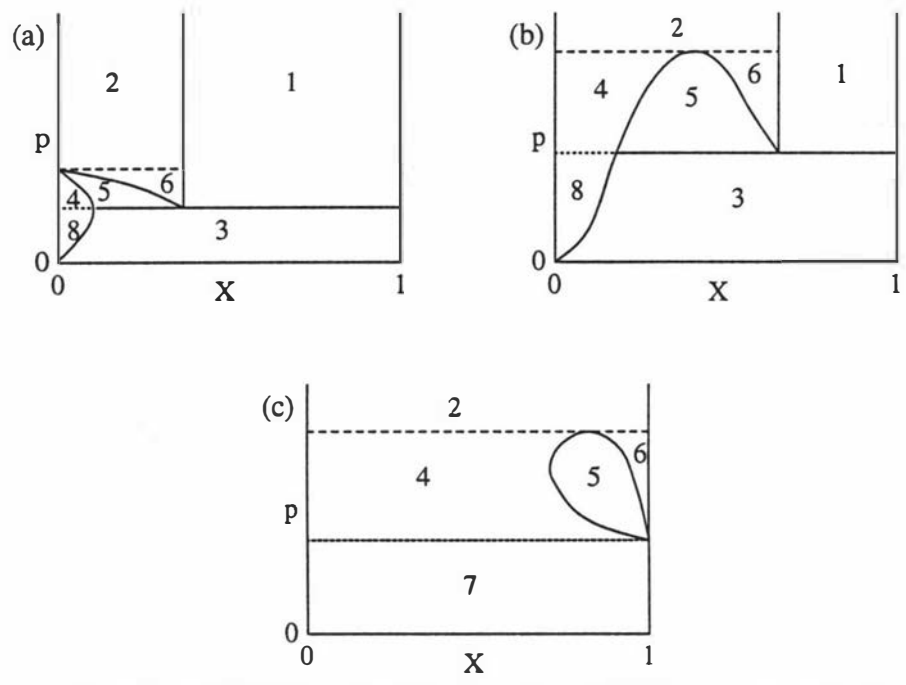

(a) $0 < T \leq 374.15$ °C (b) $374.15 < T < 800$ °C (c) $T \geq 800$ °C

$- - -$ $p_{CRIT}(T)$ $\cdots\cdots$ $p_{SAT}(T)$

Figure 3.1: Schematic isothermal cross-sections of the H_2O-NaCl state space showing the numbered regions (refer to Table 3.1), from [McKibbin and McNabb, 1993]. X is the mass fraction of sodium chloride and p is the pressure in bars absolute. $p_{CRIT}(T)$ and $p_{SAT}(T)$ are the critical and saturation pressures respectively. (a), (b) and (c) give the three different state space 'configurations'.

Table 3.1: State parameters for the eight regions in the system H_2O-NaCl (refer to Figure 3.1), adapted from [McKibbin and McNabb, 1993].

region	system state	T (°C)	p (bars absolute)	X
1	saturated liquid + solid	$T < 800$	$p > p_{SAT}(T)$	$X_{\ell\ sol}(T,p) \leq X < 1$
2	supercritical fluid	T	$p \geq p_{CRIT}(T)$	$X = X_f$, $0 < X < X_{\ell\ sol}(T,p)$
3	saturated gas + solid	$T < 800$	$p \leq p_{SAT}(T)$	$X_{g\ sol}(T,p) \leq X < 1$
4	subcritical gas	T	$p_{SAT}(T) < p < p_{CRIT}(T)$	$X = X_g$, $0 < X \leq X_{gs}(T,p)$
5	two-phase gas + liquid	T	$p_{SAT}(T) < p < p_{CRIT}(T)$	$X_{gs}(T,p) < X < X_{\ell s}(T,p)$
6	subcritical liquid	T	$p_{SAT}(T) < p < p_{CRIT}(T)$	$X = X_\ell$, $X_{\ell s}(T,p) \leq X < X_{\ell\ sol}(T,p)$
7	unsaturated gas $T \geq 800$	$T \geq 800$	$p \leq p_{SAT}(T)$	$X = X_g$, $0 < X < 1$
8	unsaturated gas $T < 800$	$T < 800$	$p \leq p_{SAT}(T)$	$X = X_g$, $0 < X < X_{g\ sol}(T,p)$

The rationale behind the naming of the different regions is as follows. (In the following discussion refer also to Table 3.1). Those regions that lie below the saturation pressure for brine, $p_{SAT}(T)$, i.e. Regions 3 and 8, see Figure 3.1 (a) and (b), are called 'gas', saturated plus solid NaCl and unsaturated respectively. The region (Region 7) that is below the saturation pressure for brine at $X = 1$, i.e. where $p_{SAT}(T) = p_{c\ sat}(T)$, see Figure 3.1 (c), is also called 'gas' (unsaturated). Region 6 is named 'liquid' (subcritical) since not only is it above $p_{SAT}(T)$ and below $p_{CRIT}(T)$, but it is also adjacent to the liquid boundary of the two-phase region (Region 5), see Figure 3.1. Similar to Region 6, Region 1 is above $p_{SAT}(T)$ and is also called 'liquid' (saturated plus solid NaCl), see Figure 3.1 (a) and (b). Region 4 is called 'gas' (subcritical)—it is adjacent to the gas boundary of Region 5, see Figure 3.1, it is above $p_{SAT}(T)$ and below $p_{CRIT}(T)$ and also for $T \leq 374.15$ at $X = 0$, see Figure 3.1 (a), it is below $p_{w\ sat}(T)$. Region 2 is above $p_{CRIT}(T)$, the critical pressure of brine, and is therefore called 'supercritical'. The fluid in Region 5 is two-phase (liquid + gas) and is therefore called 'two-phase'. Regions 4 and 8 in Figure 3.1 (a) increase in size as the temperature increases, but they are very small. Even at the upper temperature limit ($T = 374.15$ °C) of Figure 3.1 (a), the value of X at the point where the two region boundaries meet at $p_{SAT}(T)$, is only 4.7×10^{-5}. The very small size of Regions 3 and 8 (both gas regions) justifies the neglection of the solubility of NaCl in the gas phase as is assumed in the TOUGH2 subcritical module EWASG, see [Battistelli et al., 1993] and Subsection 1.2.2.

EWASG as first described in [Battistelli et al., 1993], accounts for salinity-induced vapour pressure lowering (VPL). Let us examine Figure 3.1 (a) in order to see if the eight-region state space model accounts for VPL due to salt. (Once temperatures become supercritical, salinity-induced VPL cannot be readily established since water is single-phase which is neither liquid nor vapour.) As discussed above, in Figure 3.1 (a), $p_{w\ sat}(T)$, the saturation pressure of water, is given by $p_{CRIT}(T)$ at $X = 0$. Therefore starting at pure water ($X = 0$) and $p_{CRIT}(T) = p_{w\ sat}(T)$ in Figure 3.1 (a), and increasing X (i.e. adding salt), clearly the pressures along the liquid and gas boundaries of the two-phase region (Region 5) decrease. (These boundaries are between Regions 4 and 5 for the gas boundary and between Regions 5 and 6 for the liquid boundary.) Therefore at subcritical temperatures the eight-region state space model accounts for salinity-induced VPL.

McKibbin and McNabb based their correlations mostly on experimental data

from [Sourirajan and Kennedy, 1962]. It is found that, although for some part of the state space the data of Sourirajan and Kennedy agree with the more recent data, there are other parts where the agreement is not particularly good. Although their data cover a relatively large temperature range, 350–700 °C, the maximum concentration of NaCl they considered was approximately 26 % by weight of solution (room temperature saturation for H_2O-NaCl liquid). Hence their data are not used here for the calculation of the revised correlations. The more recent data used are more self-consistent, i.e. the agreement among the different data sets is quite good, and are taken from: [Haas, 1976], [Phillips et al., 1981], [Gunter et al., 1983], [Bodnar et al., 1985], [Pitzer and Palaban, 1986], [Chou, 1987], [Sterner et al., 1988], [Knight and Bodnar, 1989],[Bischoff and Pitzer, 1989], [Tanger and Pitzer, 1989], [Anderko and Pitzer, 1993] and [Bodnar, 1994]. Not all of the data sets are used for correlation calculations. This is because some data set are overlapping, i.e. the data are similar, and one representative data set is chosen from one reference—usually the most recent one. The data are either experimental, or calculated by the authors from their theoretical equations. They are referred to as 'experimental data' and 'theoretically-calculated data', respectively. If we are unable to determine which of these categories the data are derived from, we simply call it 'data'. When a data source is quoted, it does not mean we are accepting the data points, but rather we are using the data points from the quoted source to compare them with data from other sources.

The rest of the chapter is devoted to explaining in some detail the different boundaries of the brine state space and developing the correlations that describe these boundaries. T is in °C, p is in bars absolute and $0 \leq X \leq 1$, with $X = 0$ being pure H_2O and $X = 1$ representing pure NaCl. Most of the graphs have a logarithmic scale for X. The correlation formulae can be found in Appendix A.

3.2 The three-phase surface

The three-phase surface lies beneath Region 5 (two-phase region) and above Region 3 (saturated gas + solid NaCl)—see Table 3.1 and Figure 3.1. It is bounded with respect to X by the vapour or gas saturation curve given by $X = X_{g\ SAT}(T)$ (the mass fraction of sodium chloride in the halite-saturated gas), and by $X = 1$ (pure salt)—see Figure 3.2. Figure 3.3 shows some of these features. $X = X_{g\ SAT}(T)$

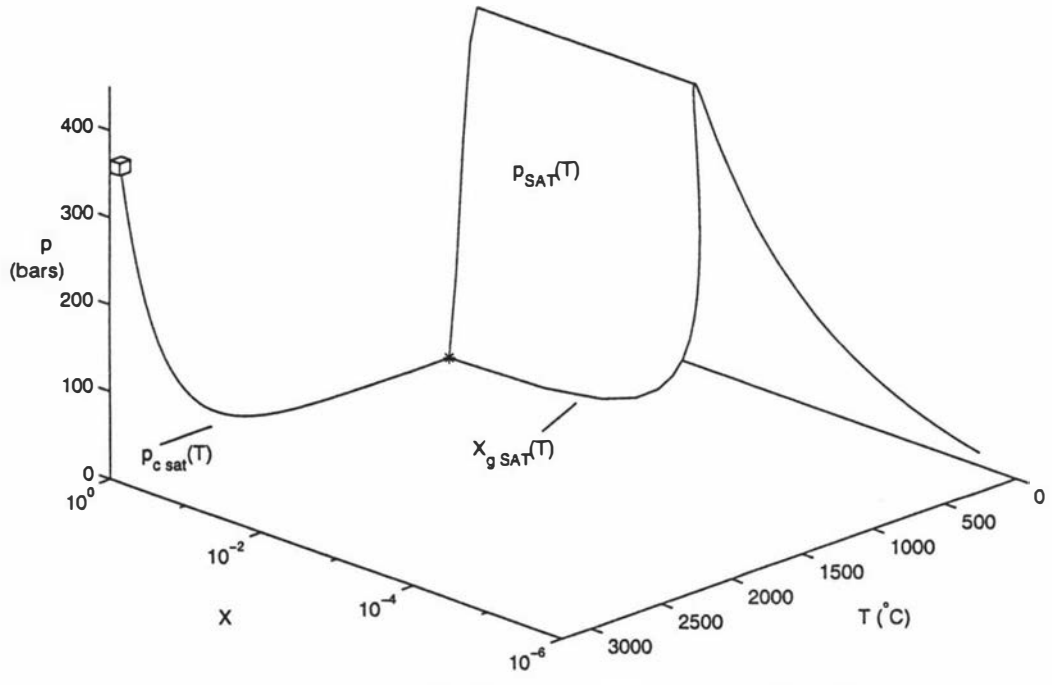

* triple point of NaCl ⌂ critical point of NaCl

Figure 3.2: An oblique view of the three-phase surface, $p_{SAT}(T)$, the gas saturation curve, $X_{g\ SAT}(T)$, and the saturation curve for sodium chloride, $p_{c\ sat}(T)$.

extends from the coexistence of halite and hydrohalite point, $(T, p) = (0.1\ °C, 0.005$ bars) $\approx$ (0 °C, 0 bars) to the triple point of NaCl (800 °C, 0 bars)—see Figure 3.2. The three-phase surface is given by $p = p_{SAT}(T)$, the saturation pressure for liquid-solid-gas equilibrium—see Figure 3.2 and Figure 3.4 for our correlation. Also shown in Figure 3.4 is the saturation curve for pure water, $p_{w\ sat}(T)$, and our correlation for the saturation curve for pure salt, $p_{c\ sat}(T)$ (also see Figure 3.2). As can be seen from Figure 3.4, there are some data for $p_{c\ sat}(T)$ up to the normal boiling point (1465 °C, 1 atm.) of NaCl. Above this point no data were discovered, which agrees with the observation made in [Anderko and Pitzer, 1992] that no vapour pressure data are available above the normal boiling point.

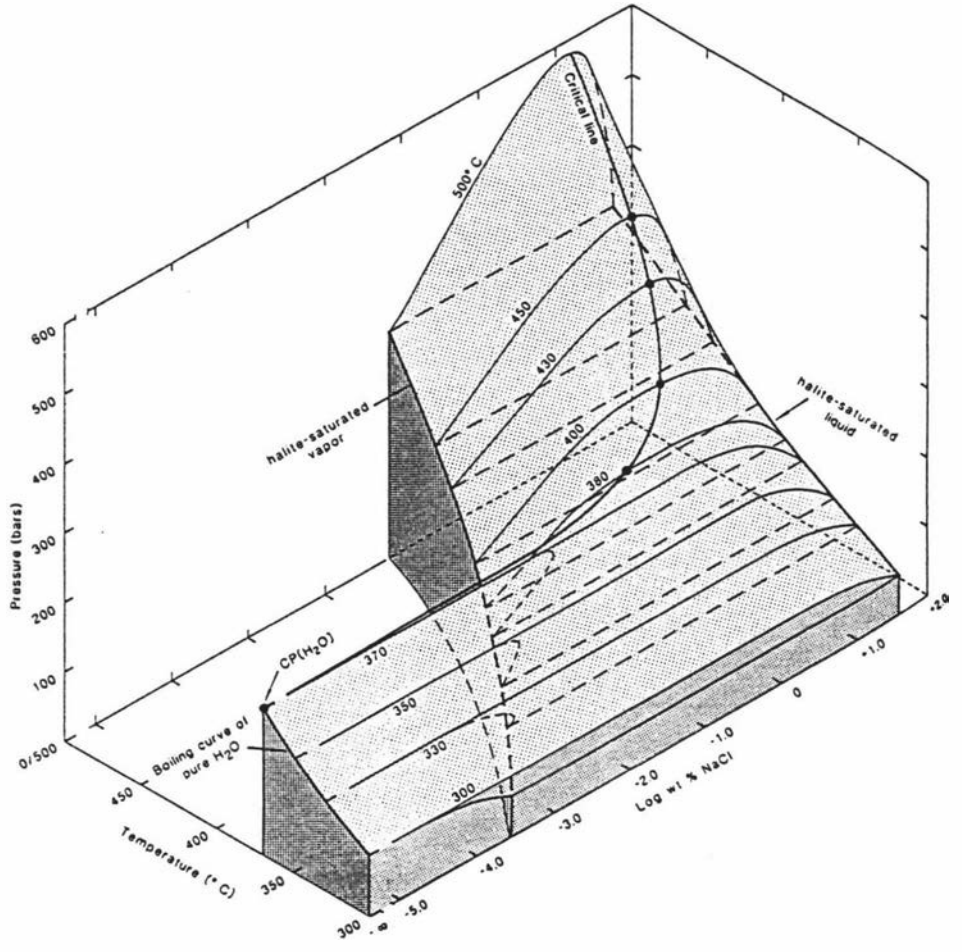

Figure 3.3: An oblique view of the system H_2O-NaCl from 300 to 500 °C, from [Bischoff and Pitzer, 1989].

The saturation curves for H_2O and NaCl extend from their triple points to their critical points. These points are well known for water, $(T, p) = (0\ °C, 0$ bars) approximately and (374.15 °C, 221.2 bars) respectively. The triple point for NaCl

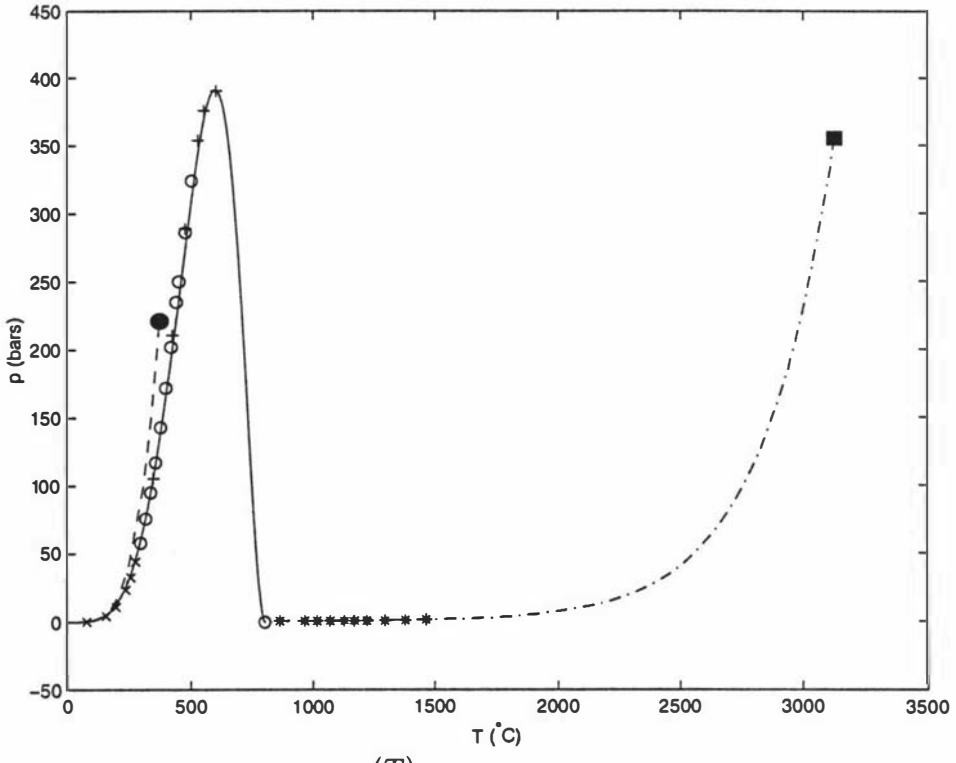

——— $p_{SAT}(T)$

– – – $p_{w\ sat}(T)$: saturation curve for H_2O

– · – · $p_{c\ sat}(T)$: saturation curve for NaCl

* data from [Kirshenbaum et al., 1962] and [Kaufmann, 1968]

× theoretically-calculated data from [Haas, 1976]

o experimental data from [Bischoff and Pitzer, 1989]

\+ theoretically-calculated data from [Tanger and Pitzer, 1989]

• critical point of H_2O ■ critical point of NaCl

Figure 3.4: Correlation for the saturation curve $p = p_{SAT}(T)$, the vapour pressure for liquid-gas-solid equilibrium.

is also well established, (800 °C, 0 bars). The agreement about the critical point for sodium chloride is not as good. For example, [McKibbin and McNabb, 1993] used the point (1075 °C, 930 bars), [Kirshenbaum et al., 1962] estimated it to be (3127 °C, 355 bars), [Bischoff and Pitzer, 1989] quoted (3600 °C, 260 bars), and [Anderko and Pitzer, 1992] calculated it to be (3568 °C, 182 bars) from their equation of state. [Pitzer, 1995] discussed some recent work done on the estimation of the critical temperature and stated that one could be quite confident that the critical temperature is in the range 2727–3127 °C and in [Pitzer, 1996] elaborated on why his 1992 estimate of 3568 °C was too high. Since we use a point on the saturation line for NaCl taken from [Kirshenbaum et al., 1962] in our correlation for the saturation line, and also use their data for the saturated density of salt (included in Chapter 4), it was decided that in order to be consistent, the critical point from Kirshenbaum et al. also be used, i.e. (3127 °C, 355 bars).

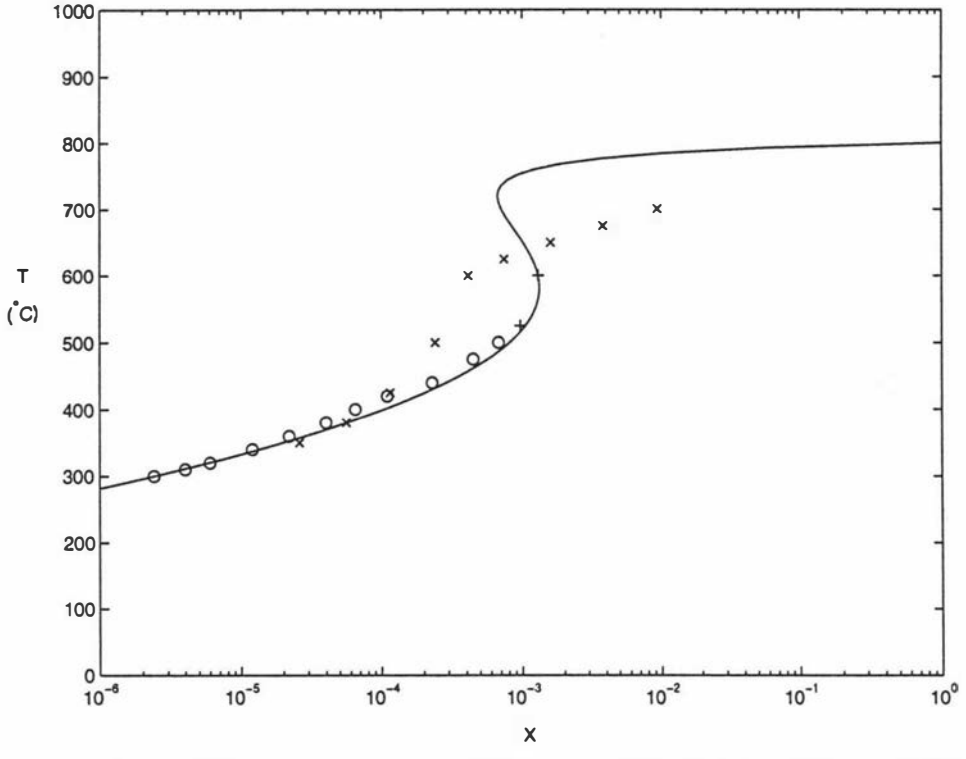

—— $X_{g\ SAT}(T)$ o experimental data from [Bischoff and Pitzer, 1989]
\+ theoretically-calculated data from [Tanger and Pitzer, 1989]
× experimental data from [Sourirajan and Kennedy, 1962]

Figure 3.5: Correlation for $X = X_{g\ SAT}(T)$, the mass fraction of NaCl in halite-saturated gas on the three-phase surface.

Our correlation for $X = X_{g\ SAT}(T)$ is shown in Figure 3.5. It illustrates the big difference between the data of [Sourirajan and Kennedy, 1962] and the data of the other recent papers. As can be seen from Figure 3.5, the recent data go up to 600 °C. The curve between 600 and 800 °C is calculated using Figure 3 from [Pitzer and Palaban, 1986] as a guide.

3.3 The halite-saturated gas (vapour) surface

This surface is between Regions 3 and 8—see Figure 3.1(a) and (b). It is given by $X_{g\ sol}(T,p)$, the maximum solubility of halite in water vapour, and Figure 3.6 shows the surface in relation to $p_{SAT}(T)$ and $X_{g\ SAT}(T)$.

Besides that of [Sourirajan and Kennedy, 1962], the only other data that could be found were the theoretically-calculated data of [Pitzer and Palaban, 1986], who show data for the temperature range 350–700 °C. For clarity, Figure 3.7 shows the data and correlations for $X_{g\ sol}$ for just three temperatures—350, 550 and 700 °C. The fit to the data is good at lower temperatures, but as the temperature increases the fit becomes less accurate.

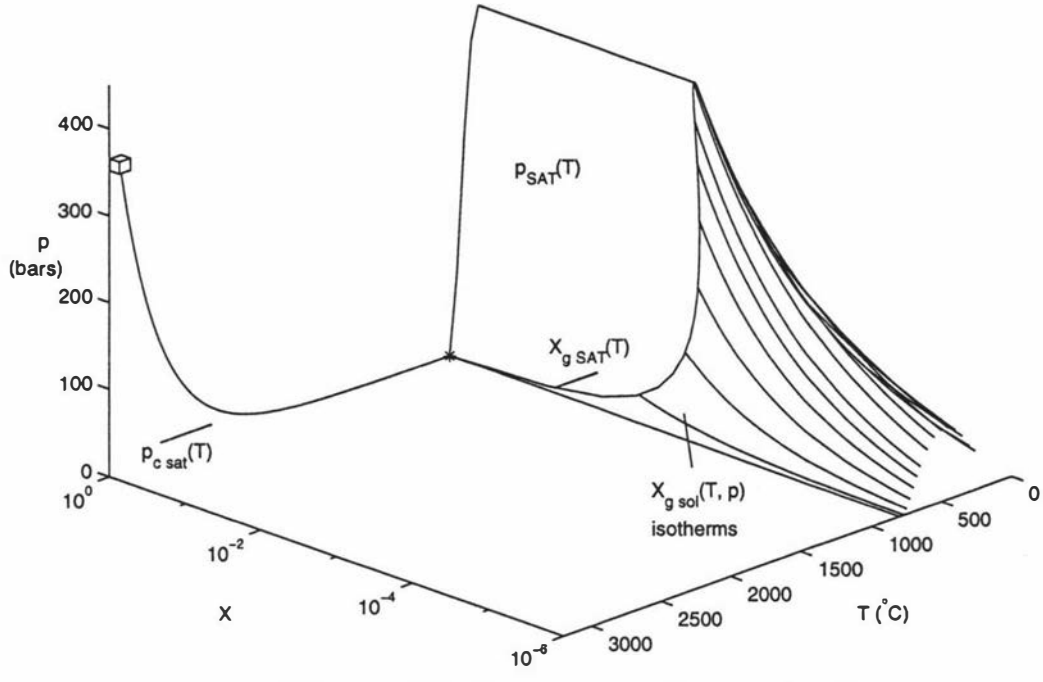

* triple point of NaCl ⌓ critical point of NaCl

Figure 3.6: An oblique view of the halite-saturated gas surface, $X_{g\ sol}(T,p)$, cf. Figure 3.2.

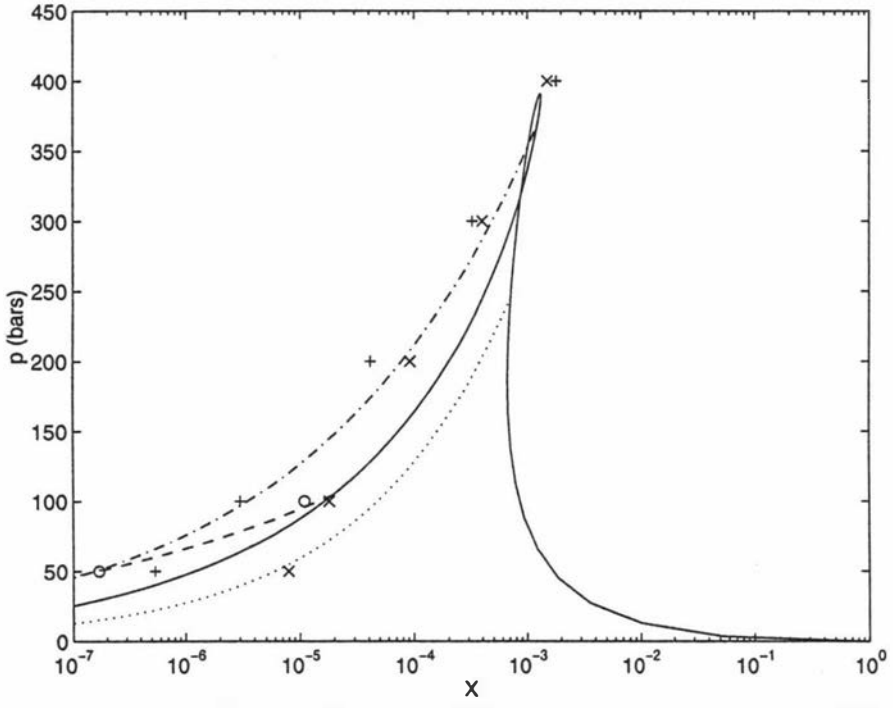

Figure 3.7: Correlation for $X = X_{g\ sol}(T,p)$, the maximum solubility of halite in water vapour. The data are from the theoretical calculations of [Pitzer and Palaban, 1986].

3.4 The critical curve

This curve extends from the critical point of water, (374.15 °C, 221.2 bars), to that of salt, (3127 °C, 355 bars), and is the apex of the liquid-gas (two-phase) region. Our choice of values for the critical point of salt is explained in Section 3.2. Figure 3.3 illustrates some of these features. Figure 3.8 shows our correlations for $p_{CRIT}(T)$ and $X_{CRIT}(T)$. According to [Bischoff and Pitzer, 1989], p_{CRIT} is estimated to reach a maximum of 2500 bars at a temperature of 2000 °C. The maximum point, given by the correlations we have developed, does not concur with that of Bischoff and Pitzer. However using the trend of data that is available, our correlations seem more compatible with known data than with the estimated maximum of Bischoff and Pitzer—see Figure 3.8(a).

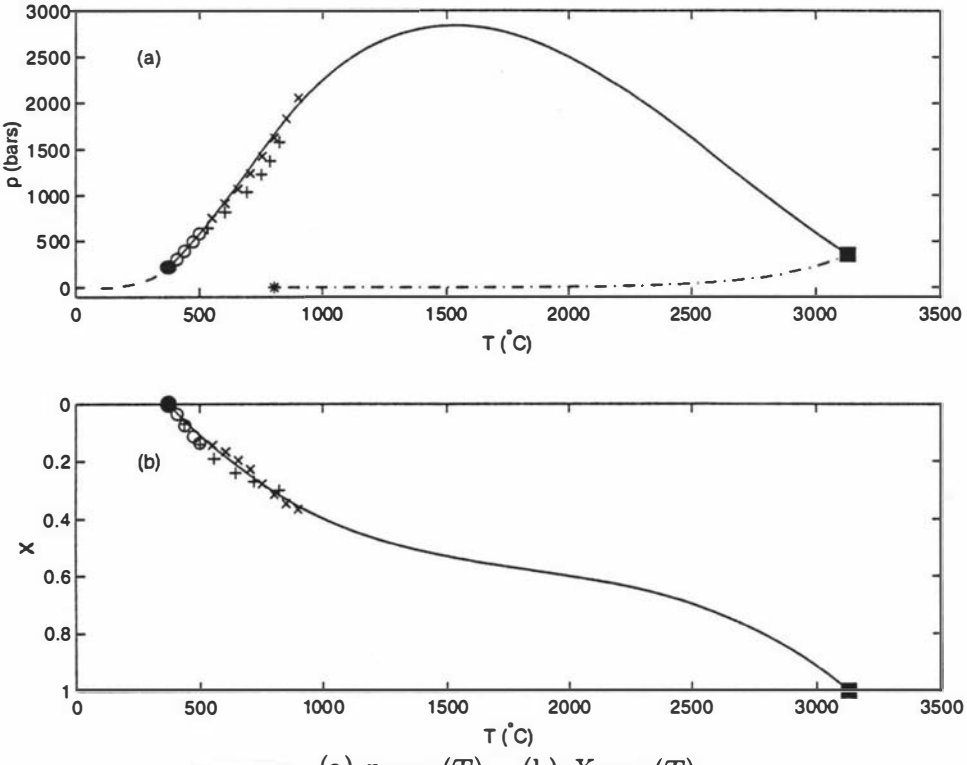

——— (a) $p_{CRIT}(T)$, (b) $X_{CRIT}(T)$

– – – $p_{w\ sat}(T)$: saturation curve for H_2O

– · – · $p_{c\ sat}(T)$: saturation curve for NaCl

o experimental data from [Bischoff and Pitzer, 1989]

\+ experimental data from [Knight and Bodnar, 1989]

× theoretically-calculated data from [Anderko and Pitzer, 1993]

• critical point of H_2O ■ critical point of NaCl * triple point of NaCl

Figure 3.8: Correlations for $p = p_{CRIT}(T)$ and $X = X_{CRIT}(T)$, the H_2O-NaCl critical curve. The theoretically-calculated data of [Tanger and Pitzer, 1989] follow the same trend as the above data points.

3.5 The halite-saturated liquid surface

This surface lies between Region 1 and Regions 2 and 6—see Figure 3.1(a) and (b). It is given by $X_{\ell\ sol}(T,p)$, the maximum solubility of halite in liquid water; the bottom edge of the surface runs along the top of the three-phase surface and is denoted by $X_{\ell\ SAT}(T)$—see Figures 3.3 and 3.9. Figure 7 of [Bodnar, 1994] shows $X_{\ell\ SAT}$ and $X_{\ell\ sol}$ for various values of X. It shows that for a given temperature, $X_{\ell\ sol} \approx X_{\ell\ SAT}$ as p increases above $p_{SAT}(T)$. It was assumed by Bodnar that the slope of the halite liquidus ($X_{\ell\ sol}$) was independent of pressure. We also assume this and make $X_{\ell\ sol} = X_{\ell\ SAT}$ for all p, i.e. $p > p_{SAT}(T)$. The data and correlations for $X_{\ell\ SAT}(T)$ are illustrated in Figure 3.10.

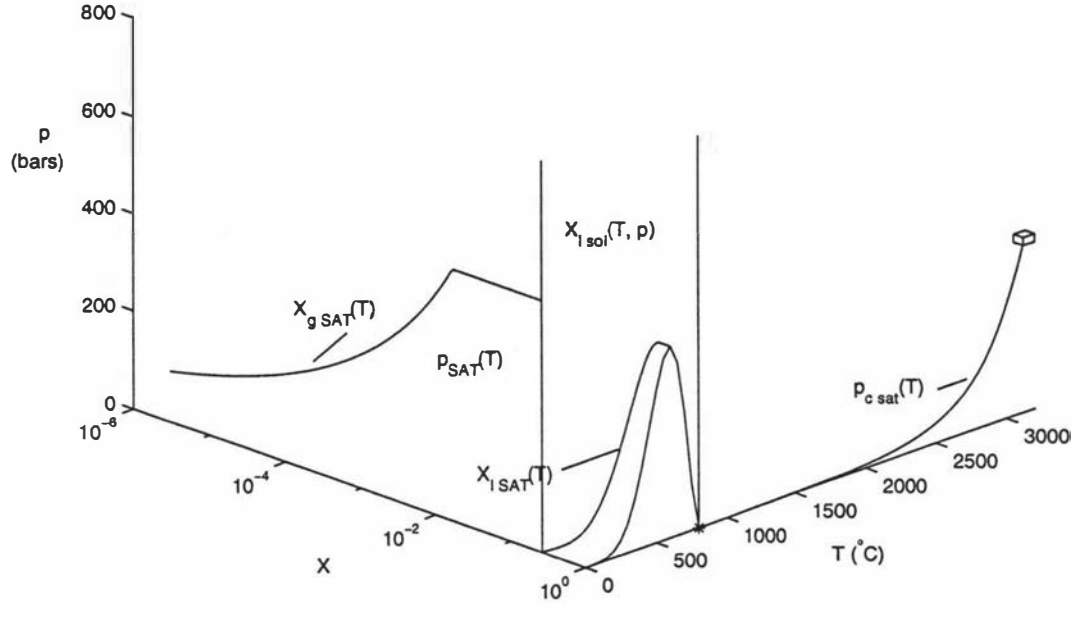

Figure 3.9: An oblique view of the halite-saturated liquid surface, $X_{\ell\ sol}(T,p)$ and $X_{\ell\ SAT}(T)$, cf. Figures 3.2 and 3.6.

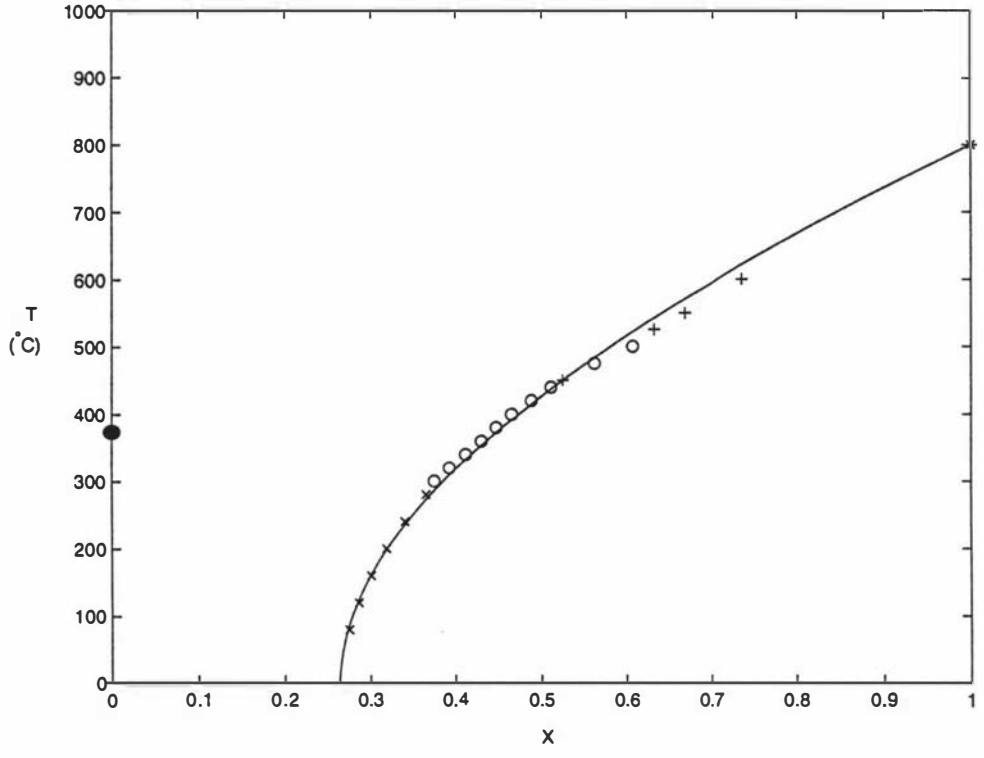

—— $X_{\ell\ SAT}(T)$ • critical point of H_2O * triple point of NaCl
× theoretically-calculated data from [Haas, 1976]
o experimental data from [Bischoff and Pitzer, 1989]
+ theoretically-calculated data from [Tanger and Pitzer, 1989]

Figure 3.10: Correlation for $X = X_{\ell\ SAT}(T)$ [$= X_{\ell\ sol}(T, p)$ for $p > p_{SAT}(T)$], the mass fraction of NaCl in saturated liquid water on the three-phase surface.

3.6 The two-phase region

This large region sits above the three-phase surface $[p_{SAT}(T)]$, for $T < 800$ °C, and above the saturation curve of sodium chloride $[p_{c\ sat}(T)]$, for $T \geq 800$ °C. Figures 3.3, 3.13 and 3.14 illustrate this. The region represents a mixture of gas and liquid, whose properties are determined by $X_{gs}(T,p)$ and $X_{\ell s}(T,p)$, the mass fraction of NaCl in the gas and liquid phases respectively of the two-phase fluid.

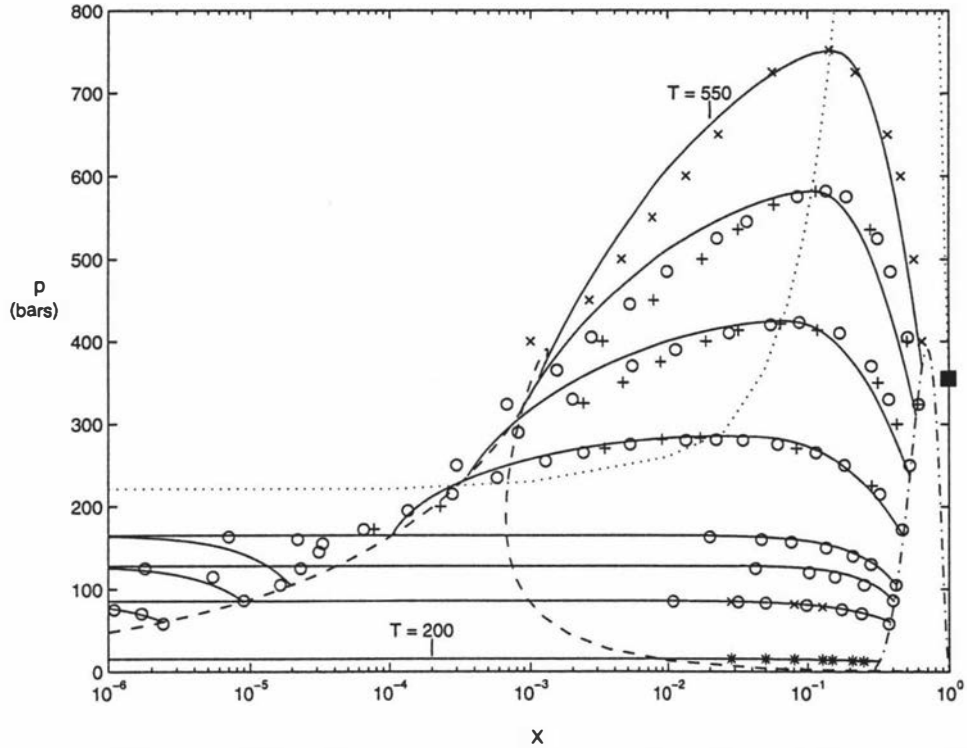

——— $X_{gs}(T,p)$ and $X_{\ell s}(T,p)$ · · · · · · proj. of $(X_{CRIT}(T), p_{CRIT}(T))$

– – – proj. of $(X_{g\ SAT}(T), p_{SAT}(T))$ — · — · proj. of $(X_{\ell\ SAT}(T), p_{SAT}(T))$

■ critical point of NaCl

* theoretically-calculated data from [Haas, 1976]

o experimental data from [Bischoff and Pitzer, 1989]

\+ theoretically-calculated data from [Tanger and Pitzer, 1989]

× theoretically-calculated data from [Anderko and Pitzer, 1993]

Figure 3.11: Correlations for $X_{gs}(T,p)$ and $X_{\ell s}(T,p)$ for $T \leq 550$ °C. Values are plotted as isotherms for $T = 200$, 300, 330, 350, 400, 450, 500 and 550 °C.

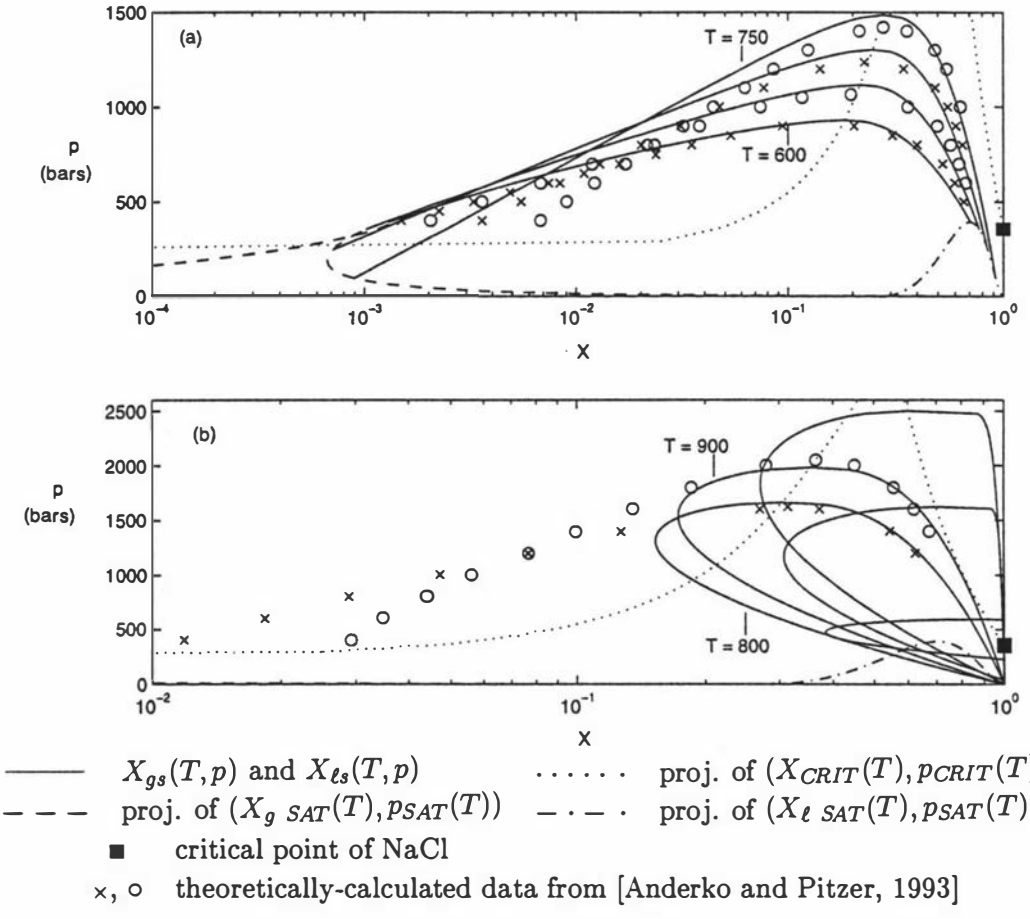

Figure 3.12: Correlations for $X_{gs}(T,p)$ and $X_{\ell s}(T,p)$ for $T \geq 600$°C. Values are plotted as isotherms for (a): T = 600, 650, 700 and 750 °C, and for (b): 800, 900, 2000, 2500 and 3000 °C.

Within this region:

$p_{SAT}(T) < p < p_{CRIT}(T)$	for all T
$X_{CRIT}(T) < X_{\ell s}(T,p) < X_{\ell\ SAT}(T)$	for all T
$X_{CRIT}(T) < X_{gs}(T,p) < X_{g\ SAT}(T)$	for $T \leq 374.15$ °C
$X_{g\ SAT}(T) < X_{gs}(T,p) < X_{CRIT}(T)$	for $374.15 < T < 800$ °C
$X_{gs}(T,p) < X_{CRIT}(T) < X_{g\ SAT}(T)$ or	
$X_{CRIT}(T) < X_{gs}(T,p) < X_{g\ SAT}(T)$	for $T \geq 800$ °C

Figures 3.11 and 3.12 show the data and correlations for X_{gs} and $X_{\ell s}$ for various T. The fit to the X_{gs} data is not as good as we would like, particularly at higher temperatures. However qualitatively the picture is correct, e.g. at higher temperatures when compared with Figure 8 of [Anderko and Pitzer, 1993]. It should be noted that for $X_{\ell s} > 0.68$ (and in fact for any properties where $X > 0.68$), the equation of state of [Anderko and Pitzer, 1993] gives values which are not accurate. This was discussed in [Pitzer and Jiang, 1996] and [Pitzer, 1997]. Hence our correlations for $X_{\ell s} > 0.68$ where $T \geq 600$ °C are extrapolations of our correlations for $X_{\ell s} \leq 0.68$, see Figure 3.12.

Figures 3.13 and 3.14 are attempts to show the two-phase region as well as the other surfaces and curves (discussed earlier in this chapter) that delineate the T-p-X state space.

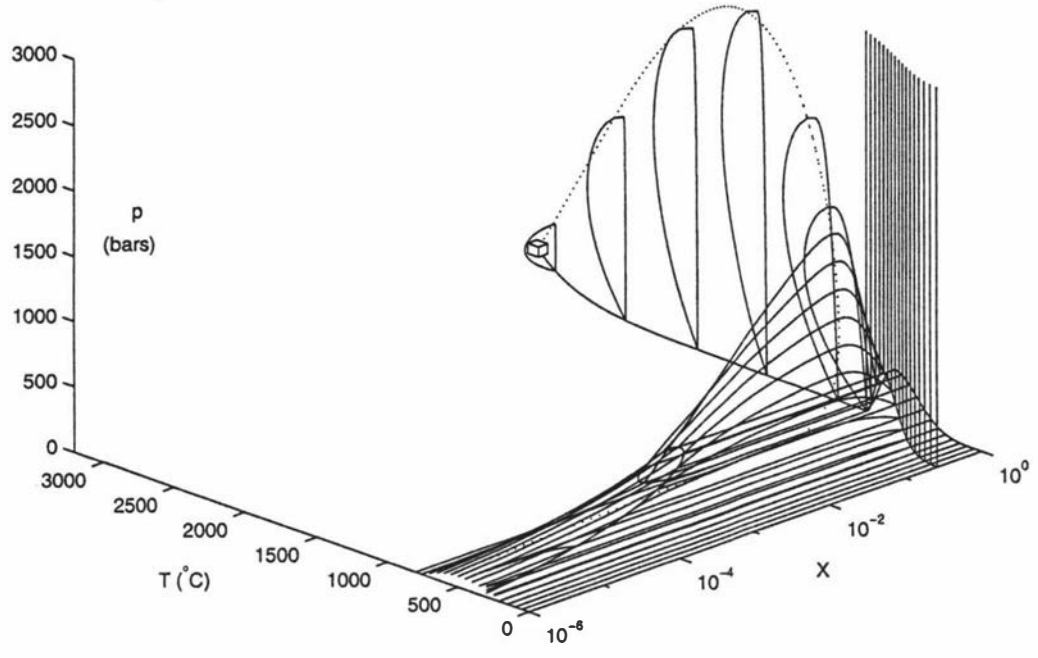

Figure 3.13: An oblique view of all the state space delineations (cf. Figures 3.2, 3.3, 3.6 and 3.9).

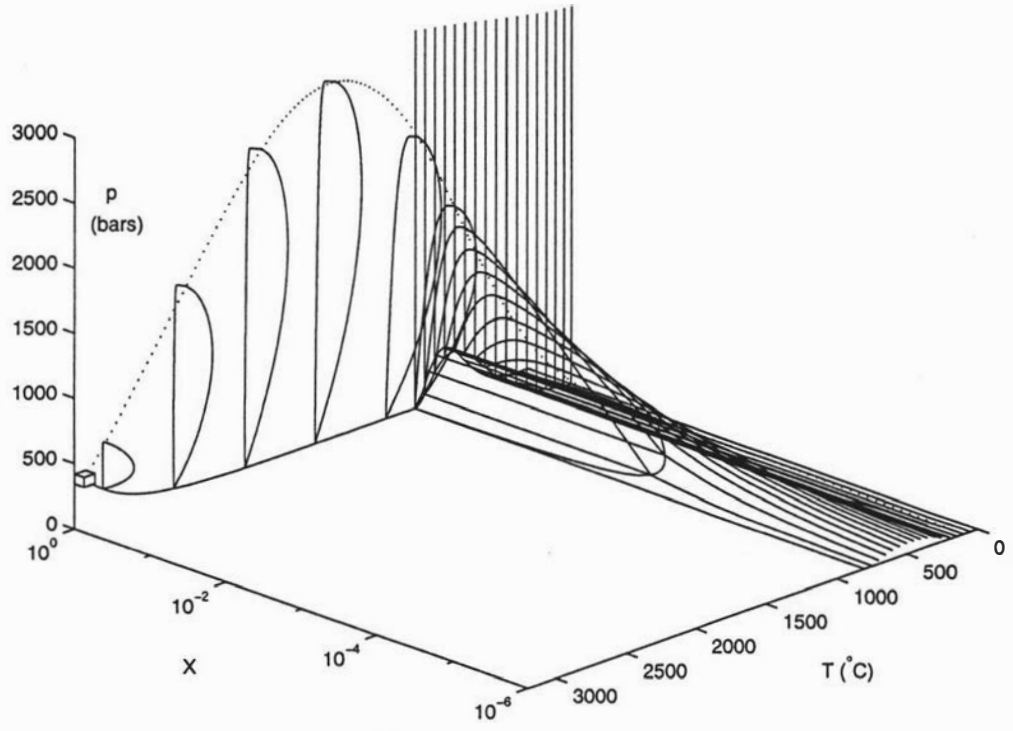

For key see Figure 3.13

Figure 3.14: Another oblique view of all the state space delineations (cf. Figures 3.2, 3.3, 3.6 and 3.9).

3.7 Summary

Correlations which delineate the brine T-p-X state space into eight different regions have been described. These regions correspond to brine being in different states. These states include single-phase liquid, single-phase gas, two-phase liquid and gas, and supercritical fluid. There are also regions where solid NaCl is in equilibrium with saturated brine liquid or gas. The correlations enable any chosen (T, p, X) value (or state point) to be classified and allocated to one of the eight regions by direct calculation rather than by data table interpolation.

When it comes to calculating the thermodynamic properties of density, enthalpy and viscosity (required for the solution of the partial differential equations described in Chapter 2), then these properties are determined according to which region the state point is in. Correlations which describe these properties are developed in the next chapter.

Chapter 4

The thermodynamic properties

4.1 Introduction

The properties required are density (ρ), specific enthalpy (h) and kinematic viscosity (ν) and are used in the equations that mathematically model the transport of heat and mass through a geothermal system, see Chapter 2. As discussed in Chapter 1, the only geothermal fluid-flow model where use is made of a subroutine which calculates one or more of the thermodynamic properties of brines at supercritical as well as subcritical temperatures, is one used for the density in [McNabb et al., 1993] and [McKibbin and McNabb, 1995a]. For that part of the T-p-X brine state space where $T \leq 374.15$ °C (the critical temperature of water) and $p < p_{w\ sat}$ (the saturation pressure of water), they use the density of pure water. For the rest of the state space, they use a subroutine for the density of brine based on data from [Haas, 1976], [Potter and Brown, 1977] and [Bischoff, 1991]—the upper temperature limit for this data is 500 °C. The subroutine is not used in this chapter for developing the correlations for density. For the enthalpy and viscosity, McNabb et al. and McKibbin & McNabb use pure water values.

Other authors have either approximated the brine property values with those of pure water or modelled subcritical brine flows and therefore used correlations for the three properties whose temperatures are subcritical. An example of the latter is the TOUGH2 module called EWASG, the latest version of which is described in [Battistelli et al., 1997]. Subsection 1.2.2 gives details on the subcritical correlations for ρ, h and ν that are described in [Battistelli et al., 1997]. None of the correlations for the three properties described in [Battistelli et al., 1993],

[Battistelli et al., 1997] or in any other work are used in this chapter, i.e. the correlations developed here are new.

This chapter develops new correlations for the ρ, h and μ (dynamic viscosity) of brine which cover the entire T-p-X state space (described in Chapter 3), and therefore extend to supercritical temperatures (and pressures). Since $\nu = \mu/\rho$, determining μ will enable us to calculate ν. These correlations are based on data taken from an extensive range of literature and are therefore, I believe, soundly-based. The correlations for our model fluid of brine are workable in the sense that they are able to be used in numerical simulation programs, but approximate in the sense that they do not everywhere exactly match the data for a pure H_2O-NaCl system. However, qualitatively our correlations are correct, and they match the pure water values ($X = 0$) for ρ, h and μ which are well known. The correlation formulae can be found in Appendices B and C.

Figure 4.1 modifies Figure 3.1 in that Region 2 is divided into two parts, namely, Region 2a where $0 < X < X_{CRIT}(T)$, and Region 2b where $X_{CRIT} \leq X < X_{\ell sol}(T,p)$—see Figure 4.1 and Table 4.1. This is a device to enable us to calculate the densities and specific enthalpies in Region 2.

Table 4.1 adds to the information shown in Table 3.1 by not only giving the thermodynamic properties required in each region, but also giving these properties as a function of the state or primary variables that are used to define the system in each of the regions. The number of state variables required for each region is given by the phase rule, see [Bear and Bachmat, 1991]. This rule is given by the equation:

$$v = 2 + n - r$$

where v is the number of independent variables which determine the state of the system, n is the number of components and r is the number of phases. For example, the two-phase region (Region 5), see Table 4.1, consists of 2 phases and 2 components, so that the number of independent state variables (v) required to define this region is two. Therefore ρ, h and μ are functions of T and p in Region 5, whereas in say Region 4 (single-phase gas), they are functions of T, p and X.

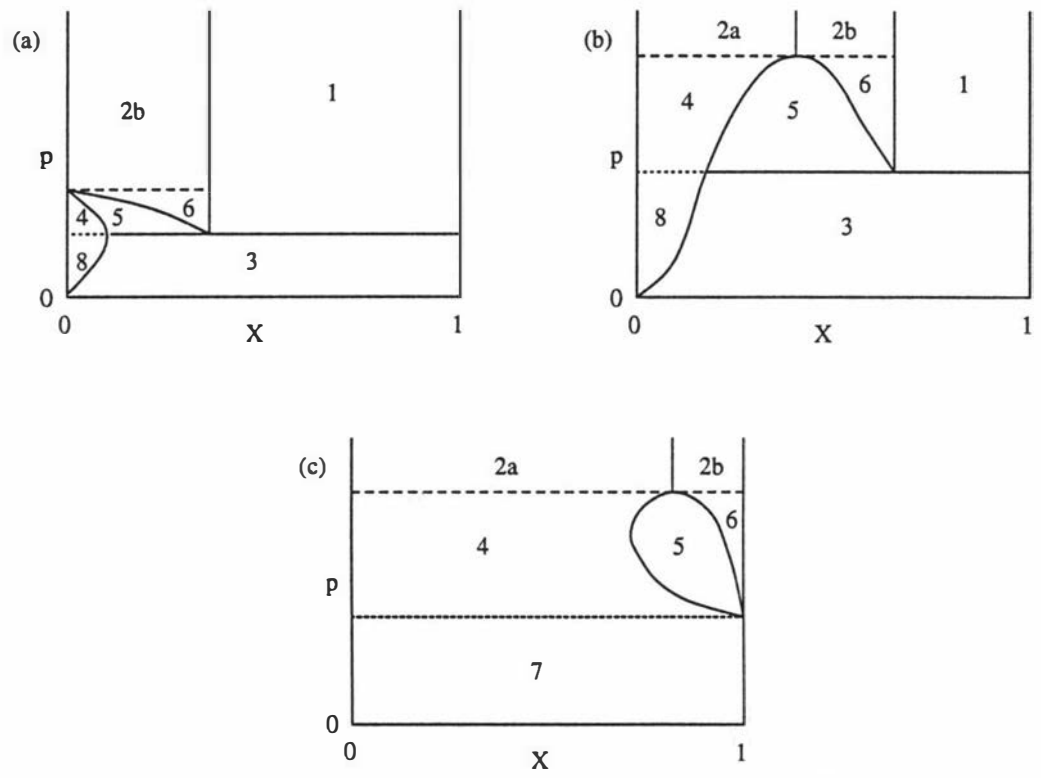

(a) $0 < T \leq 374.15$ °C (b) $374.15 < T < 800$ °C (c) $T \geq 800$ °C

$- - -$ $p_{CRIT}(T)$ $\cdots\cdots$ $p_{SAT}(T)$

Figure 4.1: Schematic isothermal cross-sections of the H_2O-NaCl state space showing the numbered regions (refer to Table 4.1), adapted from [McKibbin and McNabb, 1993]. X is the mass fraction of sodium chloride and p is the pressure in bars absolute. $p_{CRIT}(T)$ and $p_{SAT}(T)$ are the critical and saturation pressures respectively. See Chapter 3. This figure modifies Figure 3.1 by dividing Region 2 into two parts: 2a and 2b.

Table 4.1: State parameters and fluid properties required for the nine regions in the system H_2O-NaCl (refer to Figure 4.1), adapted from [McKibbin and McNabb, 1993].

region	system state	T (°C)	p (bars absolute)	X	fluid properties required
1	saturated liquid + solid	$T < 800$	$p > p_{SAT}(T)$	$X_{\ell\ sol}(T,p) \leq X < 1$	$\rho_{\ell\ sol}(T,p)$, $h_{\ell\ sol}(T,p)$, $\mu_{\ell\ sol}(T,p)$
2a 2b	supercritical fluid	T	$p \geq p_{CRIT}(T)$	$X = X_f$, 2a: $0 < X < X_{CRIT}(T)$, 2b: $X_{CRIT}(T) \leq X < X_{\ell\ sol}(T,p)$	$\rho(T,p,X)$, $h(T,p,X)$, $\mu(T,p,X)$
3	saturated gas + solid	$T < 800$	$p \leq p_{SAT}(T)$	$X_{g\ sol}(T,p) \leq X < 1$	$\rho_{g\ sol}(T,p)$, $h_{g\ sol}(T,p)$, $\mu_{g\ sol}(T,p)$
4	subcritical gas	T	$p_{SAT}(T) < p < p_{CRIT}(T)$	$X = X_g$, $0 < X \leq X_{gs}(T,p)$	$\rho_g(T,p,X)$, $h_g(T,p,X)$, $\mu_g(T,p,X)$
5	two-phase gas + liquid	T	$p_{SAT}(T) < p < p_{CRIT}(T)$	$X_{gs}(T,p) < X < X_{\ell s}(T,p)$	$\rho_{gs}(T,p)$, $\rho_{\ell s}(T,p)$, $h_{gs}(T,p)$, $h_{\ell s}(T,p)$, $\mu_{gs}(T,p)$, $\mu_{\ell s}(T,p)$
6	subcritical liquid	T	$p_{SAT}(T) < p < p_{CRIT}(T)$	$X = X_\ell$, $X_{\ell s}(T,p) \leq X < X_{\ell\ sol}(T,p)$	$\rho_\ell(T,p,X)$, $h_\ell(T,p,X)$, $\mu_\ell(T,p,X)$
7	unsaturated gas $T \geq 800$	$T \geq 800$	$p \leq p_{SAT}(T)$	$X = X_g$, $0 < X < 1$	$\rho_g(T,p,X)$, $h_g(T,p,X)$, $\mu_g(T,p,X)$
8	unsaturated gas $T < 800$	$T < 800$	$p \leq p_{SAT}(T)$	$X = X_g$, $0 < X < X_{g\ sol}(T,p)$	$\rho_g(T,p,X)$, $h_g(T,p,X)$, $\mu_g(T,p,X)$

4.2 Density

Of the three thermodynamic properties considered, most data is available for the density. The basic approach is that correlations are developed for the densities on the boundaries of the regions and linear interpolation is used between these boundary values in order to determine the densities within the different regions.

4.2.1 Water, X = 0

Using a formulation taken from [Arnold, 1970] that is discussed in [Kissling, 1995] and [White and Kissling, 1992], the density of water, $\rho_w(T, p)$, is calculated for $0 < T \leq 800$ °C and $0 < p < 1000$ bars. [White and Kissling, 1992] also discussed an alternative approximation for the thermodynamic properties provided by [Saul and Wagner, 1989] which enables the density (and other properties) to be calculated for $0 < T \leq 1000$ °C and $0 < p < 250,000$ bars. We use the Arnold formulation to calculate $\rho_w(T, p)$ for $0 < T \leq 800$ °C, $0 < p < 1000$ bars and the theoretical calculations of Saul and Wagner to calculate $\rho_w(T, p)$ for $800 < T \leq 1000$ °C, $0 < p < 1000$ bars—see Figure 4.2.

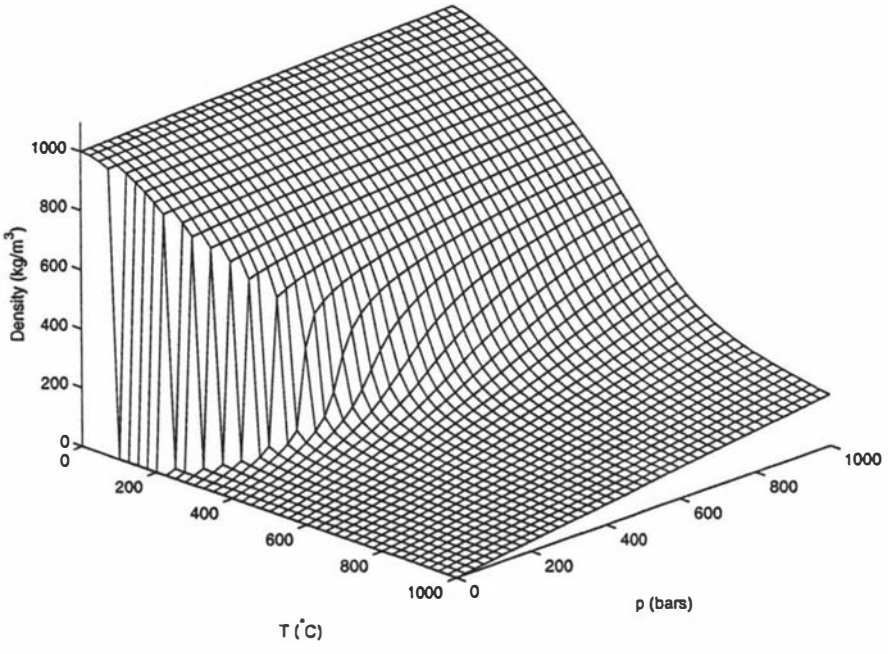

Figure 4.2: Density of water, $\rho_w(T, p)$, from [Saul and Wagner, 1989] and [Arnold, 1970], as discussed in [White and Kissling, 1992] and [Kissling, 1995].

4.2.2 Salt, X = 1

Three references, namely [Kirshenbaum et al., 1962], [Kaufmann, 1968] and [Lide, 1996], give equations for the density of liquid salt, $\rho_{cl}(T)$, from the melting point ($T = 800$ °C, p assumed to be 1 atm $\approx$ 1 bar) to higher temperatures. These equations all give similar values as can be seen from Figure 4.3. The equation of Kirshenbaum et al. which is based on experimental results, extends to the normal boiling point ($T = 1465$ °C, $p = 1$ atm $\approx$ 1 bar)—see Figure 4.4.

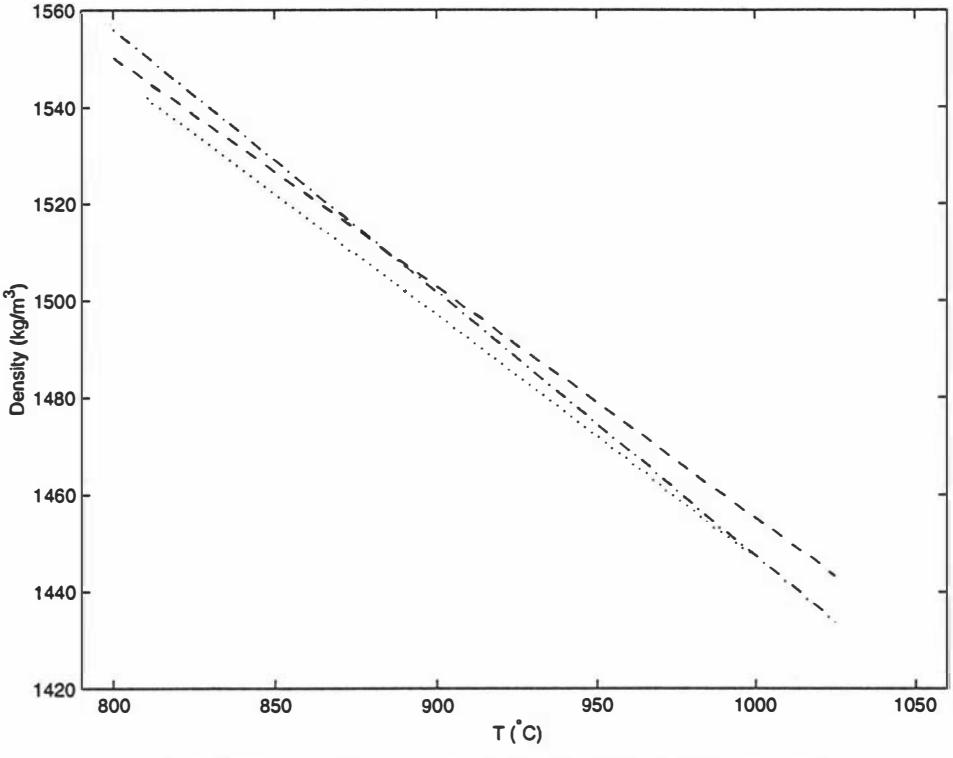

— — — correlation from [Kirshenbaum et al., 1962] based on experimental results
····· correlation from [Kaufmann, 1968] — · — · correlation from [Lide, 1996]

Figure 4.3: Density of liquid salt, $\rho_{cl}(T)$, at a pressure of approximately 1 bar.

Although saturation pressure for pure salt is less than 1 bar for $800 \leq T < 1465$ °C (see Figure 4.4), [Pitzer, 1997] stated that below pressures of 1 bar, changes in pressure have no significant effect on liquid density. Hence the equations described above for $\rho_{cl}(T)$ are valid for $\rho_{cl\ sat}(T)$, the saturated liquid density of sodium chloride. Since the temperature range of the equation of Kirshenbaum et al. extends further than that of Kaufmann and Lide, i.e. up to 1465 °C, and Kirshenbaum et al. also have data for $\rho_{cl\ sat}(T)$ when $T > 1465$ °C, we use data points

calculated from the experimentally-based equation of Kirshenbaum et al. mentioned above for $\rho_{c\ell\ sat}(T)$ where $800 \leq T \leq 1465$ °C—see Figure 4.5. Also, for $802 \leq T \leq 1397$ °C, data from their equation compared favourably with data calculated from an equation of state for pure salt that was developed in a paper by [Anderko and Pitzer, 1992]—see Table 2 of their paper.

[Anderko and Pitzer, 1993] have calculated from their equation of state, $\rho_{c\ell}(T,p)$ and $\rho_{c\ell\ sat}(T)$ at $T = 800$, 850 and 900 °C, where $\rho_{c\ell}(T,p)$ is calculated for some values of $p \geq p_{c\ sat}(T)$, the saturation pressure for sodium chloride. However as discussed in Chapter 3, this equation of state is not valid for $X > 0.68$, see [Pitzer and Jiang, 1996] and [Pitzer, 1997], so the density values for pure salt of [Anderko and Pitzer, 1993] are ignored.

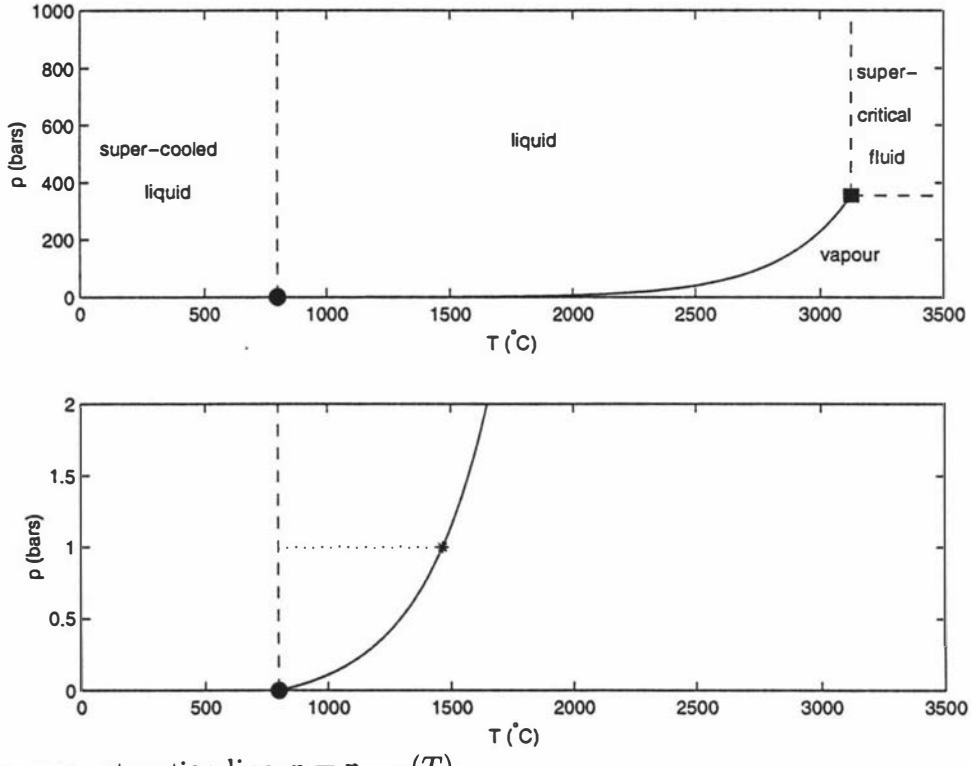

——— saturation line, $p = p_{c\ sat}(T)$

■ critical point at (3127 °C, 355 bars) • triple point at (800 °C, 0 bar)

· · · · · the line on which the equation of [Kirshenbaum et al., 1962] for $\rho_{c\ell}(T)$ is based

* the normal boiling point of NaCl, $(T,p) = (1465$ °C, 1 atm)

Figure 4.4: T-p diagram for salt. The naming of the 'super-cooled' region is taken from [Anderko and Pitzer, 1992].

[Kirshenbaum et al., 1962] have calculated the saturated liquid densities ($\rho_{c\ell\ sat}$) and saturated vapour densities ($\rho_{cg\ sat}$) of sodium chloride for temperatures ranging from $T = 1465$ °C (the normal boiling point) to $T = 2927$ °C. Their calculations are based on extrapolation of the experimental data of [Barton and Bloom, 1956] and the data of [Datz et al., 1961]. Using this data and their experimentally-based data for $\rho_{c\ell\ sat}(T)$ where $800 \leq T \leq 1465$ °C that was discussed above, we have developed correlations for $\rho_{c\ell\ sat}(T)$ and $\rho_{cg\ sat}(T)$—see Figure 4.5.

[Kirshenbaum et al., 1962] obtained the critical constants of temperature, pressure and density on a semi-empirical basis. They estimated the density at the critical point to be 220 kg/m^3, which occurs at the critical (T, p) = (3127 °C, 355 bars)—see Chapter 3. From their equation of state, [Anderko and Pitzer, 1992] calculated the critical density to be 539 cm^3/mol = 108 kg/m^3, at a critical (T, p) = (3568 °C, 182 bars). As discussed in Chapter 3, [Pitzer, 1995] stated that one could be quite confident that the critical temperature is in the range 2727–3127 °C. [Pitzer, 1995] also recommended a critical density for pure salt of 110 kg/m^3, but stated that the uncertainty remains great. Because Kirshenbaum et al. have self-consistent saturation line and critical point data, we will use their critical density just as we used their critical temperature and pressure in Chapter 3. Also the differences among the critical values of [Kirshenbaum et al., 1962], [Anderko and Pitzer, 1992] and [Pitzer, 1995] do not affect the qualitative descriptions, and affect the quantitative aspects only at very high temperatures.

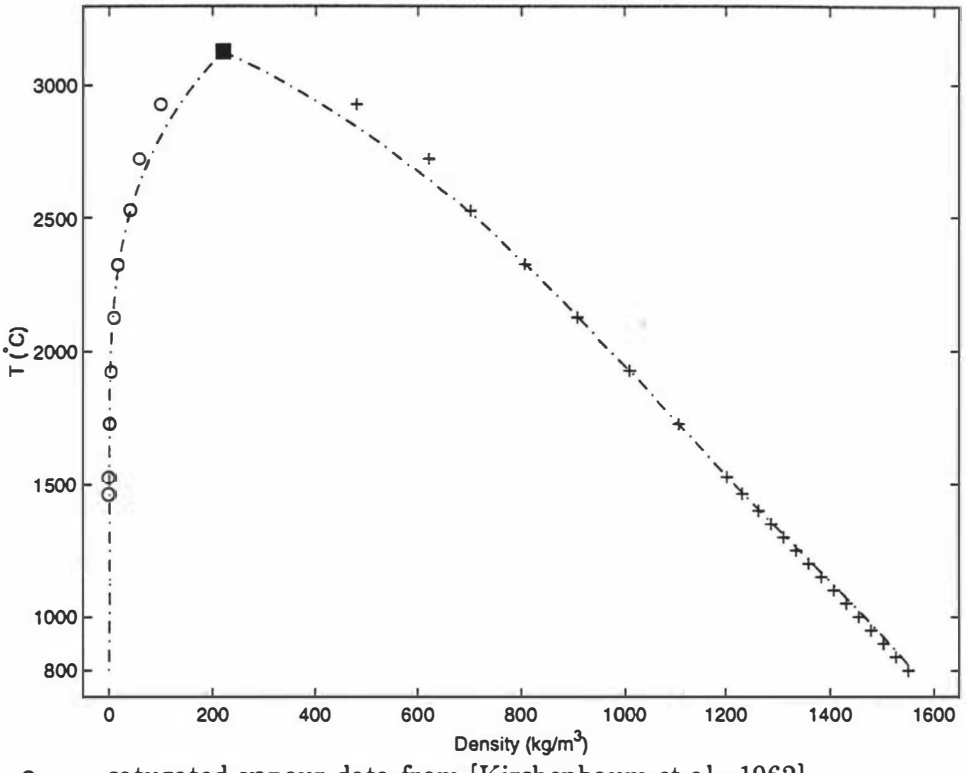

o saturated vapour data from [Kirshenbaum et al., 1962]

\+ saturated liquid data from [Kirshenbaum et al., 1962]

— · — · our correlations for the saturated densities, $\rho_{c\ell\ sat}(T)$ and $\rho_{cg\ sat}(T)$

■ critical density of NaCl, 220 kg/m^3, from [Kirshenbaum et al., 1962]

Figure 4.5: Saturated liquid and vapour densities of salt. The data points for $T \leq$ 1465 °C are calculated from an equation which [Kirshenbaum et al., 1962] based on experimental results. Their data for $T >$ 1465 °C are based on extrapolation of experimental results.

4.2.3 Brine, $0 < X < 1$

As we did in Chapter 3 for the state space data, many papers were examined and both experimental and theoretically-calculated data sets were discovered. Where these overlapped, one representative data set is chosen—usually the most recently published one.

Basically the data are of two types. Firstly data were found for the densities on the boundaries of the two-phase region (Region 5—see Figure 4.1), i.e. for $\rho_{bg\ sat} = \rho_{g\ SAT}$, $\rho_{b\ell\ sat} = \rho_{\ell\ SAT}$, ρ_{CRIT}, ρ_{gs} and $\rho_{\ell s}$, c.f. $X_{g\ SAT}$, $X_{\ell\ SAT}$, X_{CRIT}, p_{CRIT}, X_{gs} and $X_{\ell s}$ from Chapter 3. The second type of data found was that for the density of aqueous (liquid) NaCl solutions, $\rho_{b\ell}$.

Several references have $\rho_{g\ SAT}$ and $\rho_{\ell\ SAT}$, the saturated gas and liquid density respectively on the three-phase surface, as a function of T. These references include [Kaufmann, 1968], [Haas, 1976], [Chou, 1987] and [Bischoff, 1991]. Figure 4.6 shows some of their data and our correlations for that data.

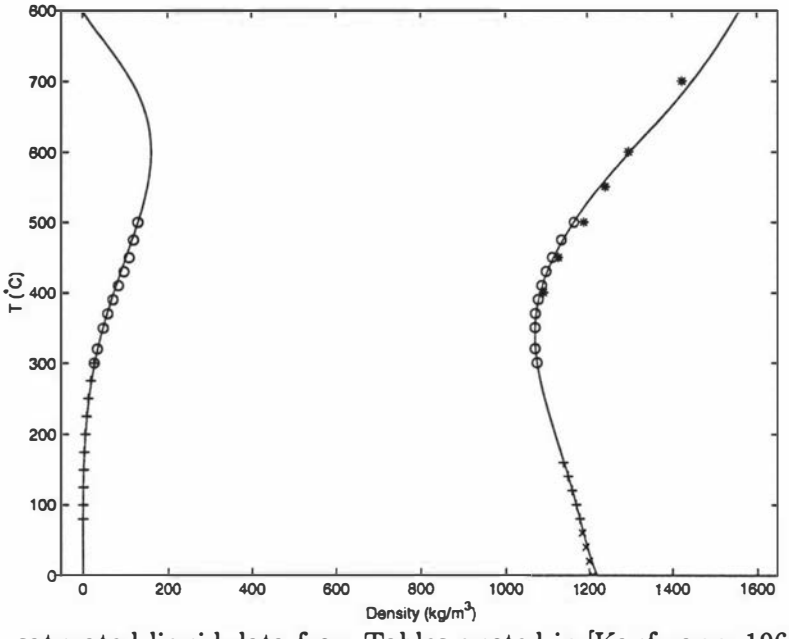

× saturated liquid data from Tables quoted in [Kaufmann, 1968]
\+ theoretically-calculated data from [Haas, 1976]
* theoretically-calculated saturated liquid data from [Chou, 1987]
o experimental data compiled by [Bischoff, 1991]
——— our correlations for the saturated densities, $\rho_{g\ SAT}(T)$ and $\rho_{\ell\ SAT}(T)$

Figure 4.6: Saturated liquid and vapour densities of brine, $\rho_{\ell\ SAT}(T)$ and $\rho_{g\ SAT}(T)$.

Data for the critical density of brine, $\rho_{CRIT}(T)$, is taken from three papers: [Knight and Bodnar, 1989], [Bischoff, 1991] and [Anderko and Pitzer, 1993]. As can be seen from Figure 4.7, Knight and Bodnar's data and that of Bischoff are similar, but the agreement between the data of Anderko and Pitzer and the data of the other two papers is not particularly good. Figure 4.8 shows a T-ρ projection of our correlations for $\rho_{g\ SAT}(T)$, $\rho_{\ell\ SAT}(T)$, $\rho_{CRIT}(T)$, $\rho_{cg\ sat}(T)$, $\rho_{c\ell\ sat}(T)$ (see Subsection 4.2.2) as well as $\rho_{wg\ sat}(T)$, $\rho_{w\ell\ sat}(T)$, the saturated gas and liquid densities for water. Figure 4.9 shows a p-ρ projection for the same correlations.

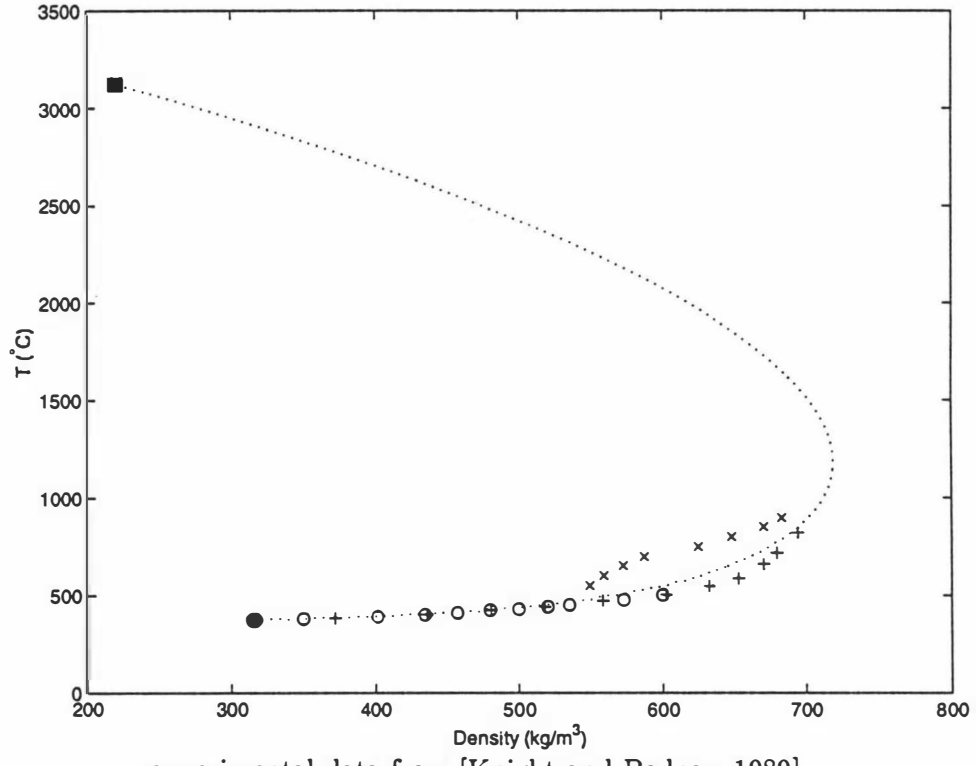

\+ experimental data from [Knight and Bodnar, 1989]
o experimental data compiled by [Bischoff, 1991]
× theoretically-calculated data from [Anderko and Pitzer, 1993]
····· our correlation, $\rho_{CRIT}(T)$
● critical density of H_2O ■ critical density of NaCl

Figure 4.7: Critical density for brine, $\rho_{CRIT}(T)$.

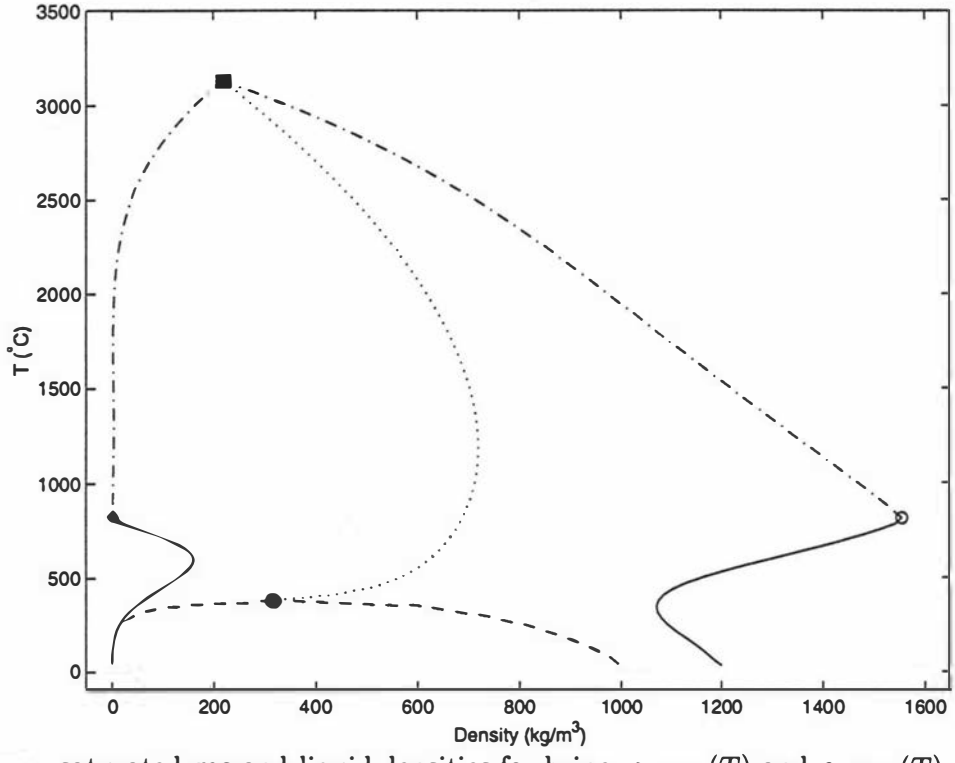

——— saturated gas and liquid densities for brine, $\rho_{g\ SAT}(T)$ and $\rho_{\ell\ SAT}(T)$

– – – saturated gas and liquid densities for water, $\rho_{wg\ sat}(T)$ and $\rho_{w\ell\ sat}(T)$

– · – · saturated gas and liquid densities for sodium chloride, $\rho_{cg\ sat}(T)$ and $\rho_{c\ell\ sat}(T)$

· · · · · critical density, $\rho_{CRIT}(T)$, of brine

* triple point density for NaCl gas ○ triple point density for NaCl liquid

● critical density of H_2O ■ critical density of NaCl

Figure 4.8: Temperature-density projection using our correlations.

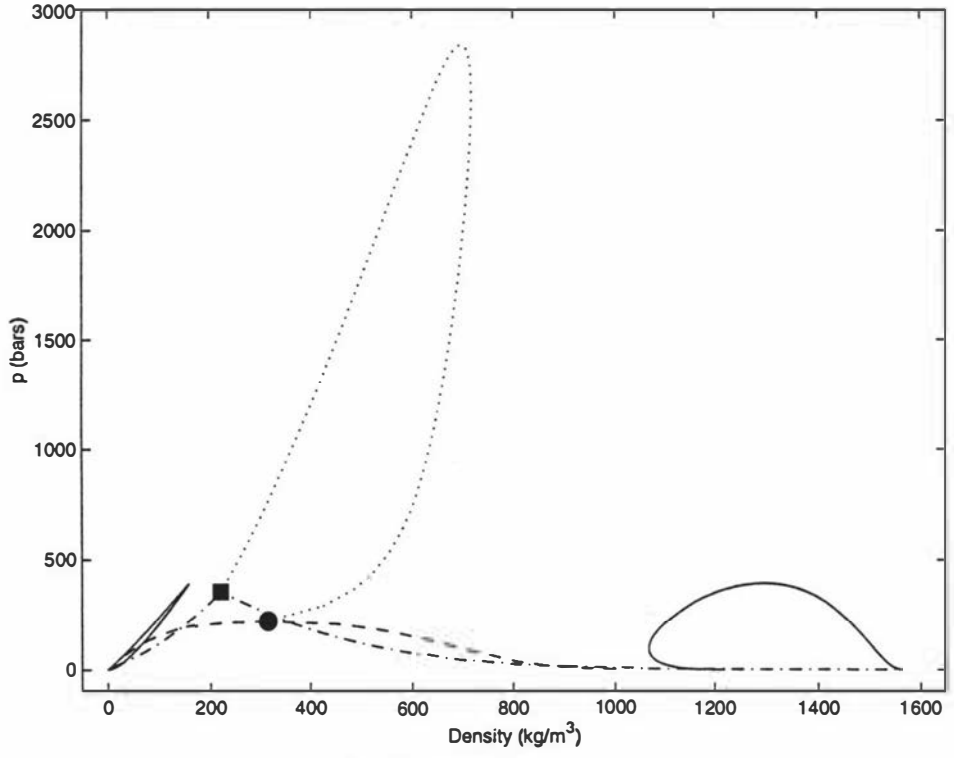

See Figure 4.8 for key

Figure 4.9: Pressure-density projection using our correlations. For key, see Figure 4.8.

For the two-phase brine fluid, the density of the gas and liquid phases are denoted by $\rho_{gs}(T,p)$ and $\rho_{\ell s}(T,p)$ respectively. [Haas, 1976], [Bischoff, 1991] and [Anderko and Pitzer, 1993] all have data for these densities; their temperature ranges are 80–300, 300–500 and 550–900 °C respectively. Figures 4.10 and 4.11 show some of this data and our correlations for various T values, while Figure 4.12 is a p-ρ projection showing our correlations for various T between 380 and 3000 °C. Note that Figures 4.10 – 4.12 show that for given T, $\rho_{\ell s}$ increases as p decreases. Conceptually this does not seem correct. However these figures are 2-D projections of a 4-D space (T-p-X-ρ) and in fact what is happening here is that $\rho_{\ell s}$ (and ρ_{gs}) increase with X. Figure 4.13 shows this for some data at various T.

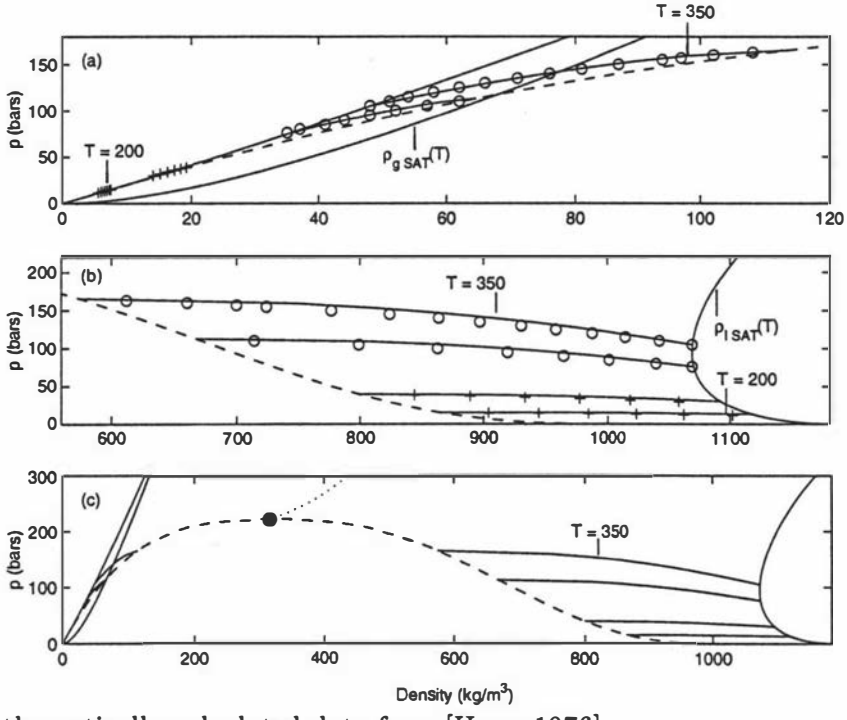

\+ theoretically-calculated data from [Haas, 1976]

o experimental data compiled by [Bischoff, 1991]

– – – proj. of saturated gas and liquid densities for water, $\rho_{wg\ sat}(T)$ and $\rho_{w\ell\ sat}(T)$

· · · · · proj. of critical density, $\rho_{CRIT}(T)$, of brine • critical density of H_2O

(a) data and our correlation for $\rho_{gs}(T,p)$

(b) data and our correlation for $\rho_{\ell s}(T,p)$

(c) our correlations for $\rho_{gs}(T,p)$ and $\rho_{\ell s}(T,p)$

Figure 4.10: Correlations for the density of the gas phase, $\rho_{gs}(T,p)$, and liquid phase, $\rho_{\ell s}(T,p)$, for the two-phase fluid for $T \leq 374.15$ °C. Values are plotted as isotherms for $T = 200$, 250, 320 and 350 °C.

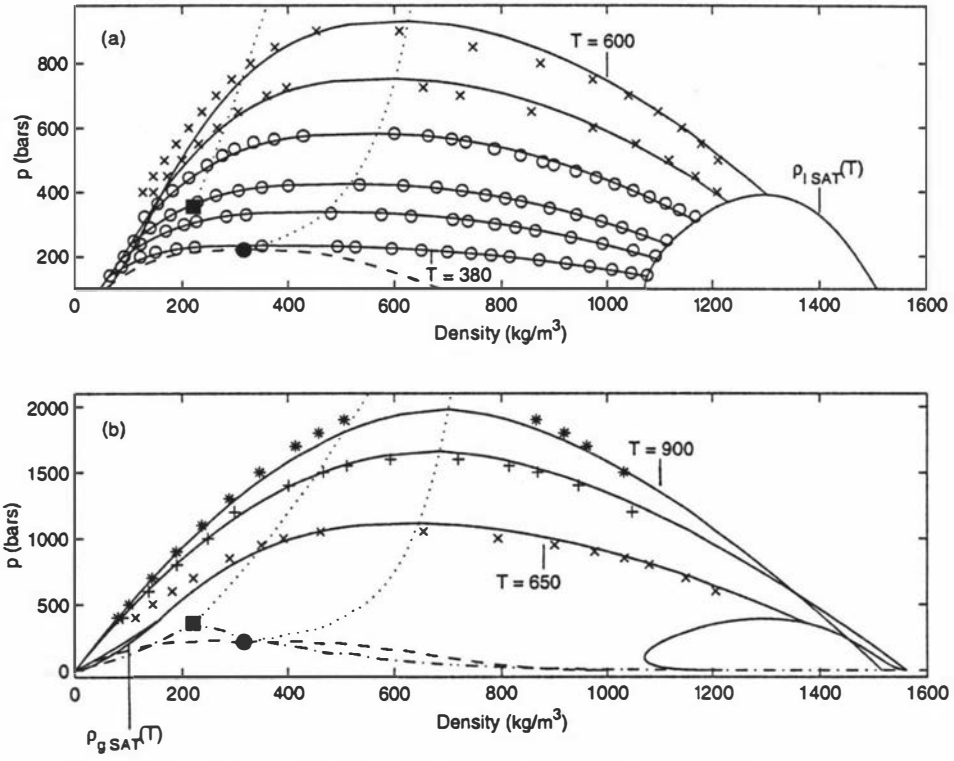

o experimental data compiled by [Bischoff, 1991]

×, +, * theoretically-calculated data from [Anderko and Pitzer, 1993]

— — — proj. of saturated gas and liquid densities for water, $\rho_{wg\ sat}(T)$ and $\rho_{w\ell\ sat}(T)$

— · — · proj. of saturated gas and liquid densities for sodium chloride, $\rho_{cg\ sat}(T)$ and $\rho_{c\ell\ sat}(T)$

· · · · · proj. of critical density, $\rho_{CRIT}(T)$, of brine

■ critical density of NaCl • critical density of H_2O

(a) data and our correlations for $\rho_{gs}(T,p)$ and $\rho_{\ell s}(T,p)$ for $374.15 < T \leq 600$ °C

(b) data and our correlation for $\rho_{gs}(T,p)$ and $\rho_{\ell s}(T,p)$ for $600 < T \leq 900$ °C

Figure 4.11: Correlations for the density of the gas phase, $\rho_{gs}(T,p)$, and liquid phase, $\rho_{\ell s}(T,p)$, for the two-phase fluid for $T > 374.15$ °C. Values are plotted as isotherms for $T = 380$, 420, 450, 500, 550, 600, 650, 800 and 900 °C.

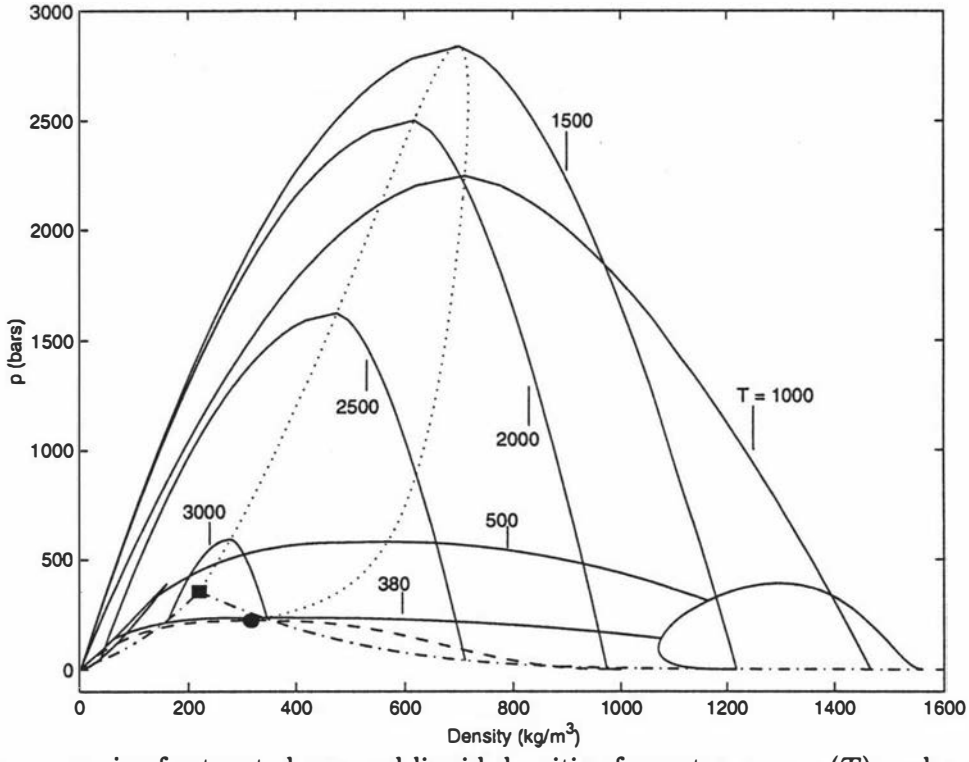

– – – proj. of saturated gas and liquid densities for water, $\rho_{wg\ sat}(T)$ and $\rho_{w\ell\ sat}(T)$

– · – · proj. of saturated gas and liquid densities for sodium chloride, $\rho_{cg\ sat}(T)$ and $\rho_{c\ell\ sat}(T)$

· · · · · proj. of critical density, $\rho_{CRIT}(T)$, of brine

■ critical density of NaCl

• critical density of H_2O

Figure 4.12: Pressure-density projection showing $\rho_{gs}(T,p)$ and $\rho_{\ell s}(T,p)$ for T = 380, 500, 1000, 1500, 2000, 2500 and 3000 °C.

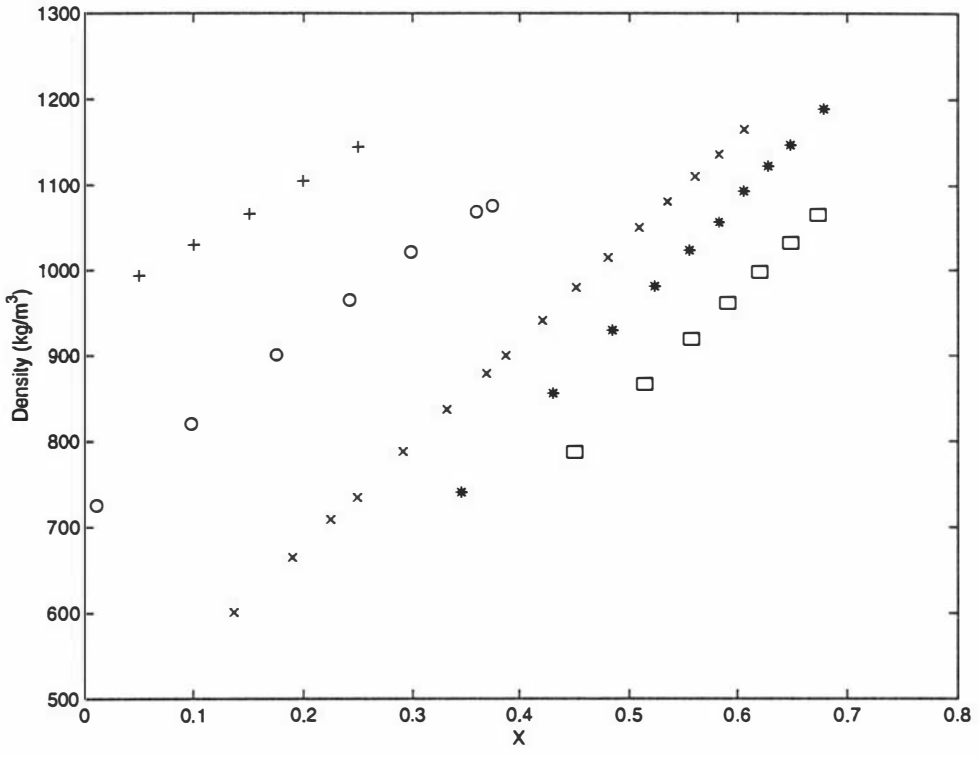

Figure 4.13: Some data for $\rho_{\ell s}$ at various T. The data for $T = 100$ °C are from the theoretical calculations of [Haas, 1976], for $T = 300$ and 500 °C from the experimental compilations of [Bischoff, 1991], and for $T = 700$ and 900 °C from the theoretical calculations of [Anderko and Pitzer, 1993].

There is a considerable amount of data for the density of liquid brine, $\rho_{b\ell}$. Most of it falls in that part of Region 2 where $X_{CRIT} \leq X < X_{\ell\ sol}$ (Region 2b, the 'liquid' part of supercritical brine)—see Figure 4.1, and the rest is in Region 6. Table 4.2 shows most of the references for the $\rho_{b\ell}$ data with their corresponding T, p, X ranges, and the region into which the data falls. The X value of most of the data falls well below $X_{\ell\ sol}(T,p)$, the maximum solubility of halite in liquid water, i.e. the boundary between Regions 1, 2b and 6—see Figure 4.1(a) and (b). Some of the data has X values which are just less than $X_{\ell\ sol}(T,p)$ and this is illustrated in Figure 4.14, but no data could be found for $\rho_{\ell\ sol}(T,p)$, the density of saturated liquid brine for $p > p_{SAT}(T)$.

Table 4.2: T-p-X ranges of the various data for the density of liquid brine, $\rho_{b\ell}$.

Reference	T (°C)	p (bars)	X	Region
[Ellis and Golding, 1963]	175–350	Not specified	0.0–0.15	–
[Kaufmann, 1968]	0–100	Not specified, presumably 1 atm $\approx$ 1 bar	0.01–0.26	2b and 6
[Potter and Brown, 1977]	25–500	$p_{\ell s}$–2000	0.01–0.25	2b and 6
[Phillips et al., 1981]	10–350	$p_{\ell s}$–500	0.01–0.23	2b and 6
[Rogers and Pitzer, 1982]	0–300	$p_{\ell s}$–1000	0.005–0.23	2b
[Pitzer et al., 1983]	0–300	$p_{\ell s}$–1000	0.005–0.26	2b
[Tanger and Pitzer, 1989]	300–500	$p_{\ell s}$–800	0.032–0.10	2b
[Anderko and Pitzer, 1993]	300–900	$p_{\ell s}$–5000	0.077–0.68	2b and 6
[Simonson et al., 1994]	25–250	70–400	0.01–0.24	2b
[Alkan et al., 1995]	Not specified	Not specified	Not specified	–
[Lide, 1996]	20	1 atm $\approx$ 1 bar	0–0.26	2b

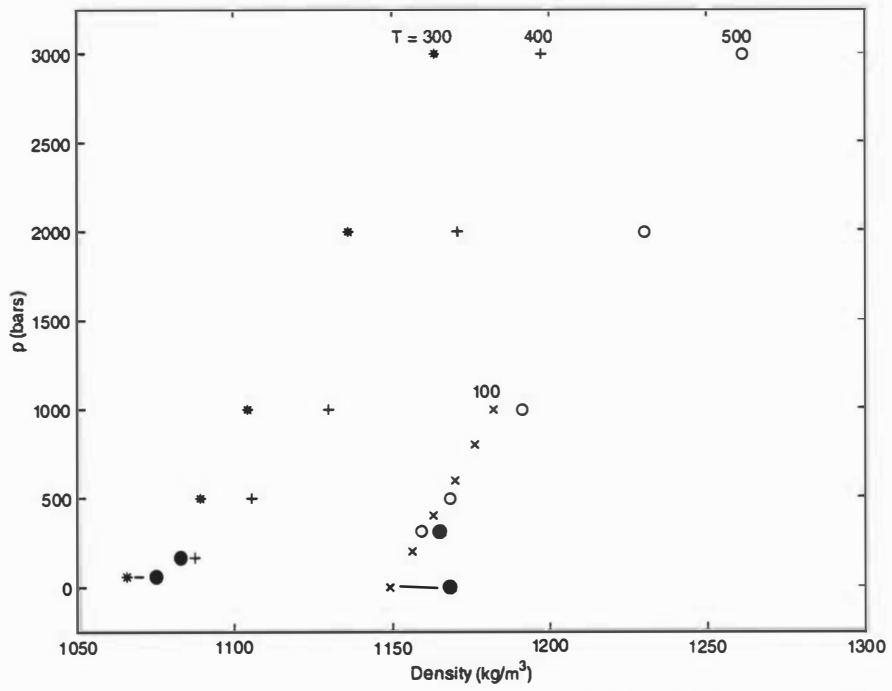

[T (°C), X, $X_{\ell\ sol}(T,p)$, character] = [100, 0.2596, 0.2783, ×], [300, 0.3640, 0.3856, ∗], [400, 0.4477, 0.4735, +], [500, 0.5815, 0.5816, ∘]

- proj. of the density of saturated liquid brine, $\rho_{\ell\ SAT}(T)$ at $X_{\ell\ SAT}(T)$, $p_{\ell\ SAT}(T)$, for the various T, where $\rho_{\ell\ SAT}$, $X_{\ell\ SAT}$ and $p_{\ell\ SAT}$ are calculated from our correlations.

Figure 4.14: Pressure-density projection for liquid brine, $\rho_{b\ell}$, for various T and X_ℓ, where X_ℓ is just less than $X_{\ell\ sol}(T,p)$. The data for T = 100 °C are from the theoretical calculations of [Pitzer et al., 1983]. The data for the other T are from [Anderko and Pitzer, 1993] which they calculated from their equation of state.

4.2.4 The density for the regions

Region 1

The density of the salt-saturated liquid in equilibrium with solid salt is given by

$$\rho(T, p, X_{\ell\ sol}(T, p)) = \rho_{\ell\ sol}(T, p)$$

As mentioned in Subsection 4.2.3, no data have been found in the literature for $\rho_{\ell\ sol}(T, p)$. Figure 4.14 shows some data for $\rho_{b\ell}$ for various T and X_ℓ, where X_ℓ is just less than $X_{\ell\ sol}(T, p)$. Assuming that $\rho_{\ell\ sol}(T, p)$ behaves in a similar way to the data of Figure 4.14, it can be seen that there is some variation of $\rho_{\ell\ sol}(T, p)$ with p for a given T. However, we will assume that, because this occurs over such a large p range, the variation is small enough in our model fluid for $\rho_{\ell\ sol}$ to remain constant for all p, and in fact equal $\rho_{\ell\ SAT}(T)$, i.e.

$$\rho_{\ell\ sol}(T, p) = \rho_{\ell\ sol}(T) = \rho_{\ell\ SAT}(T)$$

Region 3

Analogous to the correlation for $X_{g\ sol}(T, p)$, which is given as a fraction of $X_{g\ SAT}(T)$ (see Appendix A), the density of the salt-saturated brine gas, $\rho_{g\ sol}(T, p)$, is given as a fraction of $\rho_{g\ SAT}(T)$.

$$\rho_b = \rho_g(T, p, X_{g\ sol}(T, p)) = \rho_{g\ sol}(T, p) = \rho_{g\ SAT}(T)\frac{p}{p_{SAT}(T)}$$

Region 5

For this two-phase region, the density is given in terms of $\rho_{gs}(T, p)$, $\rho_{\ell s}(T, p)$ and S_ℓ, the liquid saturation, which is the volume fraction of liquid present in the fluid.

$$\rho_b = \rho_b(T, p) = (1 - S_\ell)\rho_{gs}(T, p) + S_\ell\rho_{\ell s}(T, p)$$

Regions 4, 7 and 8

For given T and p, linear interpolations are made between correlated values on the region boundaries, using X as the interpolation parameter.

Region 4: subcritical gas

$$\rho_b = \rho_g(T, p, X) = \rho_w(T, p) + \frac{X}{X_{gs}(T, p)}[\rho_{gs}(T, p) - \rho_w(T, p)]$$

Region 7: unsaturated gas, $T \geq 800$ °C

$$\begin{aligned} \rho_b &= \rho_g(T,p,X) \\ &= \rho_w(T,p) + \frac{X}{X_{g\ sol}(T,p)}[\rho_{g\ sol}(T,p) - \rho_w(T,p)] \\ &= \rho_w(T,p) + X[\rho_{g\ sol}(T,p) - \rho_w(T,p)] \end{aligned}$$

since $X_{g\ sol}(T,p) = 1$

Region 8: unsaturated gas, $T < 800$ °C

$$\rho_b = \rho_g(T,p,X) = \rho_w(T,p) + \frac{X}{X_{g\ sol}(T,p)}[\rho_{g\ sol}(T,p) - \rho_w(T,p)]$$

Regions 2 and 6

In order to match ρ (and h) in Region 4 (gas) and Region 6 (liquid) at the region boundaries, Region 2 has been divided into two parts: Region 2a where $0 < X < X_{CRIT}(T)$, and Region 2b where $X_{CRIT}(T) \leq X < X_{\ell\ sol}(T)$—see Figure 4.1.

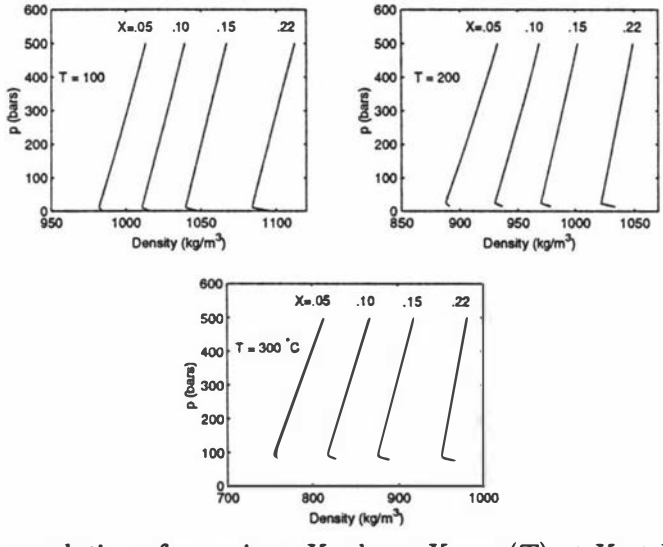

——— correlations for various X where $X_{CRIT}(T) < X < X_{\ell\ sol}(T,p)$

Figure 4.15: Density-pressure projections of brine data in Region 2b (supercritical 'liquid') and 6 (subcritical liquid), for various T and X. The correlations are based on that of [Phillips et al., 1981], which was developed using experimental values. The densities at the lowest pressure, $p_{\ell s}$, for each X are $\rho_{\ell s}(T,p)$, i.e. the densities along the liquid boundary of the two-phase region. $p_{\ell s}$ is calculated by inverting the formula for $X_{\ell s}$, which is given in Appendix A.

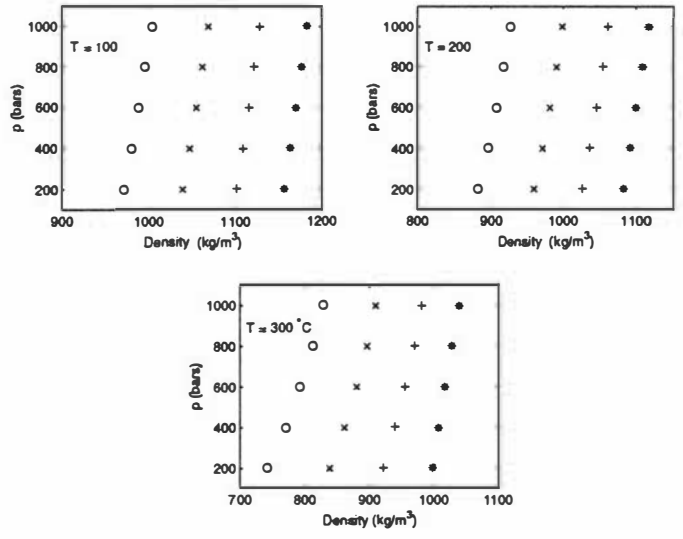

$\circ \quad X = 0.006 \quad \times \quad X = 0.105 \quad + \quad X = 0.189 \quad * \quad X = 0.260$

Figure 4.16: Density-pressure projections of brine data in Region 2b (supercritical 'liquid') and 6 (subcritical liquid), for various T and X. The data are from the theoretical calculations of [Pitzer et al., 1983].

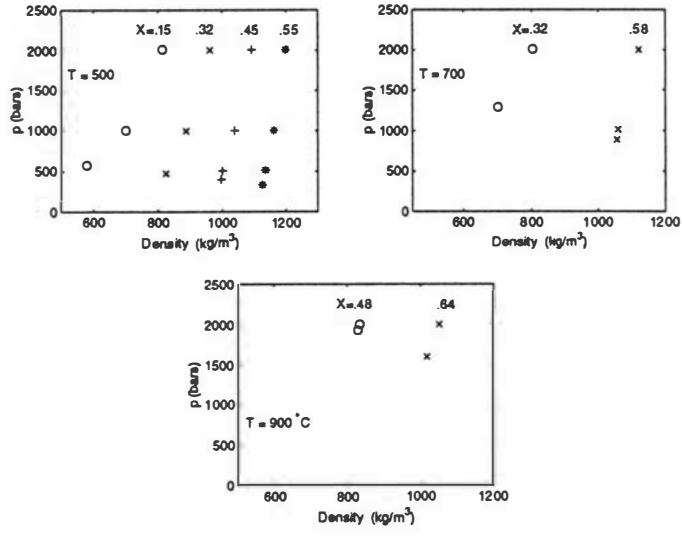

Figure 4.17: Density-pressure projections of brine data in Region 2b (supercritical 'liquid') and 6 (subcritical liquid), for various T and X. The data are from [Anderko and Pitzer, 1993] which they calculated from their equation of state. The densities at the lowest pressure, $p_{\ell s}$, for each X are $\rho_{\ell s}(T, p)$, i.e. the densities along the liquid boundary of the two-phase region. $p_{\ell s}$ is calculated by inverting the formula for $X_{\ell s}$, which is given in Appendix A.

Regions 2b and 6

As mentioned above there is a considerable amount of data for Region 2b and some for Region 6—see Table 4.2. Some of the data have inconsistencies. For example, [Potter and Brown, 1977], for $T = 300$ °C, have for some X values, $\rho_{\ell s}$ (at $p < 100$ bars) $> \rho$ (at $p = 100$ bars). Physically this seems counter-intuitive. Figures 4.15 to 4.17 show that there is some variation of density with pressure for various T and X in Regions 2b and 6. Note the inconsistency in Figure 4.15 where $\rho_{\ell s} > \rho$ for some values of $p > p_{\ell s}$.

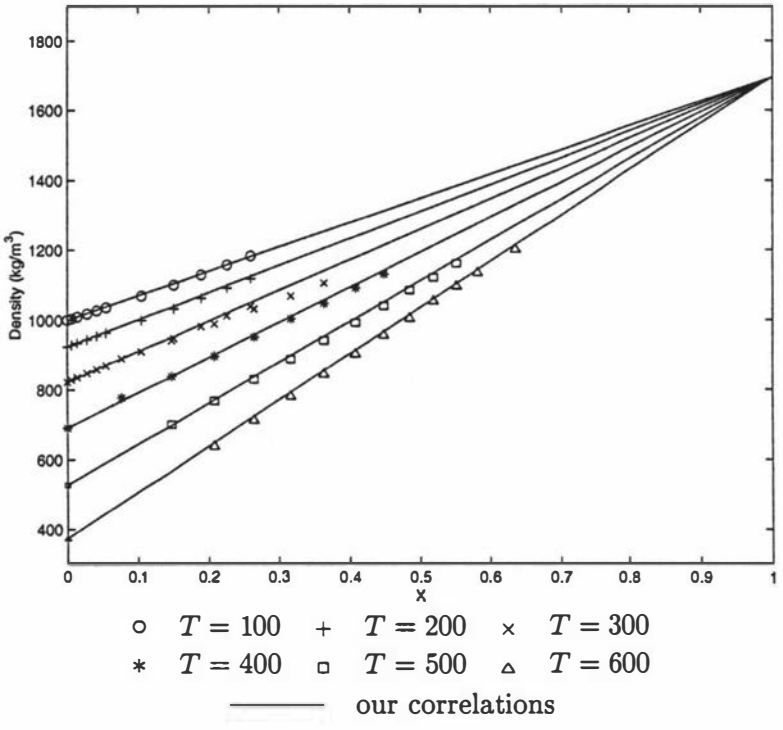

Figure 4.18: The density of brine at $p = 1000$ bars, i.e. in Region 2b (supercritical 'liquid'), for various T and X. The data for $T = 100$, 200, 300 °C, $X > 0$, are from the theoretical calculations of [Pitzer et al., 1983]. The data for $T = 300$, 400, 500, 600 °C, $X > 0$, are from [Anderko and Pitzer, 1993] which they calculated from their equation of state. $\rho_{\ell s}$ at $X = 0$ (ρ_w) is calculated from the formulation discussed in Subsection 4.2.1.

Recalling that in Region 2b and 6, $p \geq p_{\ell s}$ for all T and X, the density in these regions is now calculated as follows. Figure 4.18 shows the density of brine in Region 2b (and 2a) at $p = 1000$ bars for various T and X. For a given T, the relationship between X and ρ is closely linear. A correlation for $\rho_{1000}(T, X)$, the

density at $p = 1000$ bars, is given in terms of T and X by:

$$\begin{aligned}\rho_{1000}(T,X) &= \rho_b(T, p = 1000, X) \\ &= \rho_w(T, p = 1000) + X[1695 - \rho_w(T, p = 1000)]\end{aligned}$$

The value of $p = 1000$ bars is chosen since this is the maximum pressure to which our correlation for $\rho_w(T,p)$ extends. For $p \leq 1000$ bars, we linearly interpolate between $\rho_{\ell s}$ and ρ_{1000} in order to calculate the densities in Regions 2b and 6:

$$\rho_b(T,p,X) = \rho_{\ell s}(T, p_{\ell s}(T,X)) + \frac{p - p_{\ell s}(T,X)}{1000 - p_{\ell s}(T,X)}[\rho_{1000}(T,X) - \rho_{\ell s}(T, p_{\ell s}(T,X))]$$

Mostly $\rho_{1000} > \rho_{\ell s}$, but if this inequality is not true then we take $\rho_b = \rho_{\ell s}$. If $p > 1000$ bars and there is a sufficiently large positive difference (taken here as ≥ 500) between 1000 and $p_{\ell s}$, the density is taken to be ρ_{1000}. If $1000 - p_{\ell s}$ becomes too small (< 500) or negative, i.e. if $p_{\ell s}$ gets too close to 1000 or is greater than 1000, then $1000 - p_{\ell s}$ is adjusted so that there is always a sufficiently large positive difference (here, 500) between 1000 and $p_{\ell s}$. If adjustment is required, then ρ_b does not become constant at ρ_{1000} as soon as p is just greater than 1000, but rather at some $p = p_{\ell s} + 500$ bars. This feature, some data at various T and X, and our correlations that have just been described are illustrated in Figures 4.19 – 4.23.

Region 2a

Linear interpolation is used between $\rho_w(T,p)$ and an interpolated value of ρ (say ρ_{2b}) based on the Region 2b and 6 regime outlined above at $X = X_{CRIT}$, i.e. where $p_{\ell s}(T,X) = p_{CRIT}(T)$, $\rho_{\ell s}(T,p) = \rho_{CRIT}(T)$, and $\rho_{1000}(T,X) = \rho_{1000}(T, X_{CRIT})$. Therefore the density in Region 2a is calculated as follows:

$$\begin{aligned}\rho_b &= \rho_b(T,p,X_{CRIT}(T)) \\ &= \rho_w(T,p) + \frac{X}{X_{CRIT}(T)}[\rho_{2b}(T,p,X_{CRIT}(T)) - \rho_w(T,p)]\end{aligned}$$

Therefore based on which of the nine regions the state point is in, densities can be calculated for the entire T-p-X brine state space.

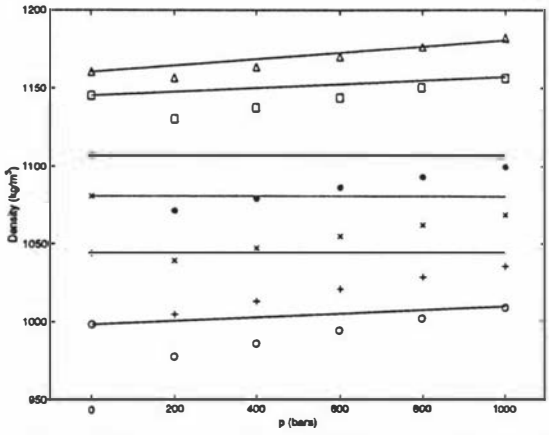

o $X = 0.014$ + $X = 0.055$ × $X = 0.105$
* $X = 0.149$ □ $X = 0.226$ △ $X = 0.260$
——— our correlations

Figure 4.19: The density of brine in Region 2b (supercritical 'liquid') and 6 (subcritical liquid) at $T = 100$ °C for various p and X. The data for $p \geq 200$ are from the theoretical calculations of [Pitzer et al., 1983]. In Figures 4.19 – 4.23 the densities at the lowest pressure, $p_{\ell s}$, for each X are $\rho_{\ell s}(T, p)$, i.e. the densities along the liquid boundary of the two-phase region. $\rho_{\ell s}$ is calculated using our correlations for $\rho_{\ell s}$—see Appendix B.1. $p_{\ell s}$ is calculated by inverting the formula for $X_{\ell s}$ which is given in Appendix A.

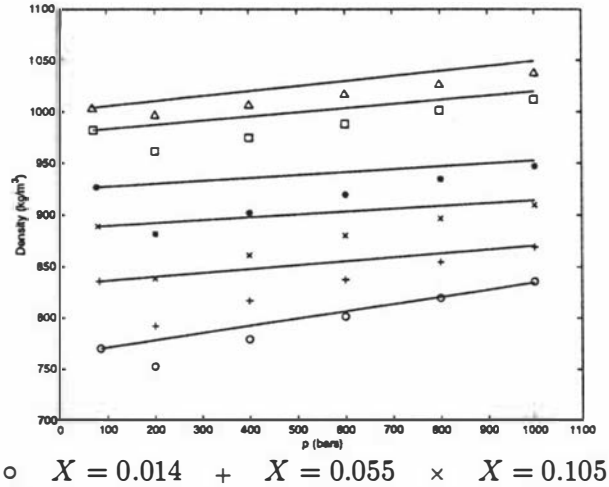

o $X = 0.014$ + $X = 0.055$ × $X = 0.105$
* $X = 0.149$ □ $X = 0.226$ △ $X = 0.260$
——— our correlations

Figure 4.20: The density of brine in Region 2b (supercritical 'liquid') and 6 (subcritical liquid) at $T = 300$ °C for various p and X. The data for $p \geq 200$ are from the theoretical calculations of [Pitzer et al., 1983].

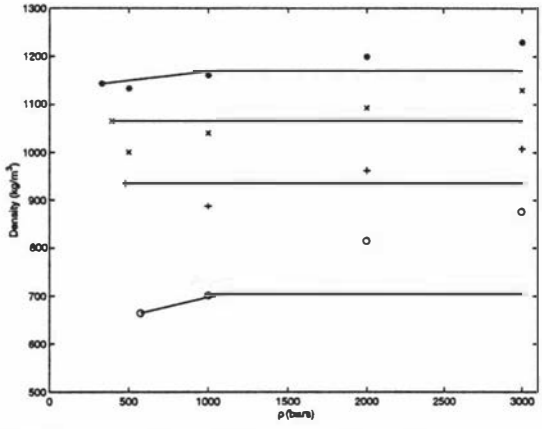

o $X = 0.15$ + $X = 0.32$ × $X = 0.45$ * $X = 0.55$

——— our correlations

Figure 4.21: The density of brine in Region 2b (supercritical 'liquid') and 6 (subcritical liquid) at $T = 500$ °C for various p and X. The data are from the theoretical calculations of [Anderko and Pitzer, 1993].

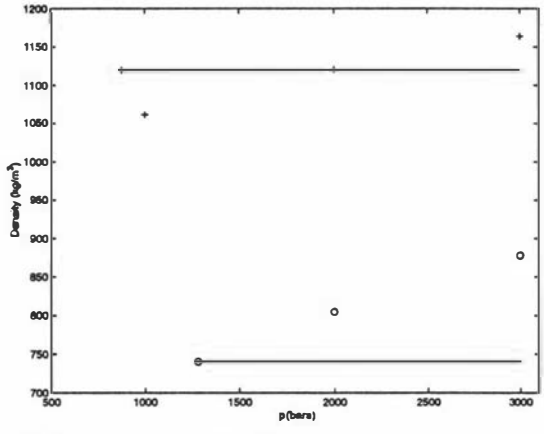

o $X = 0.32$ + $X = 0.58$ ——— our correlations

Figure 4.22: The density of brine in Region 2b (supercritical 'liquid') and 6 (subcritical liquid) at $T = 700$ °C for various p and X. The data are from the theoretical calculations of [Anderko and Pitzer, 1993].

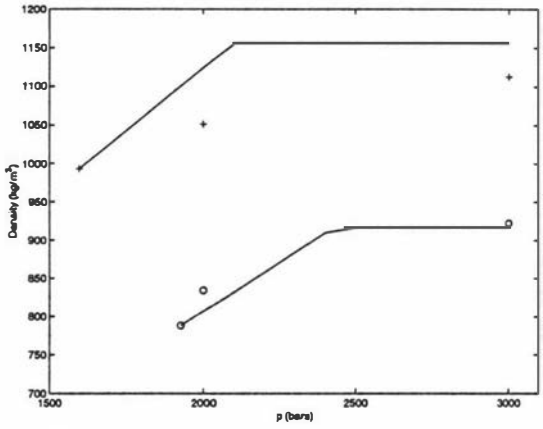

o $X = 0.48$ + $X = 0.64$ ——— our correlations

Figure 4.23: The density of brine in Region 2b (supercritical 'liquid') and 6 (subcritical liquid) at $T = 900$ °C for various p and X. The data are from the theoretical calculations of [Anderko and Pitzer, 1993].

Figures 4.24 – 4.26 are isothermal projections of the four dimensional T-p-X-ρ space. The three temperatures (250, 500, 1000 °C) that are used in order to illustrate our model for the density, are typical temperatures corresponding to Figures 4.1(a), 4.1(b) and 4.1(c) respectively. The densities are calculated using the equations given in Appendix C. Region 5 is 'prohibited' in the sense that a point in Region 5 is attainable only by a mixture of the two fluid phases at the given temperature and pressure. In Regions 1 and 3, the brine is saturated with respect to solid salt. Therefore X for the fluid remains constant in Regions 1 and 3. For pictorial clarity the density values in Region 5 are set to zero in Figures 4.24 – 4.26. The caption for each of these figures describes which of the nine regions the state point is in, as the densities are calculated for various p and X at the given T. Note the logarithmic scale for X in Figures 4.24 and 4.25 and the linear scale for X in Figure 4.26.

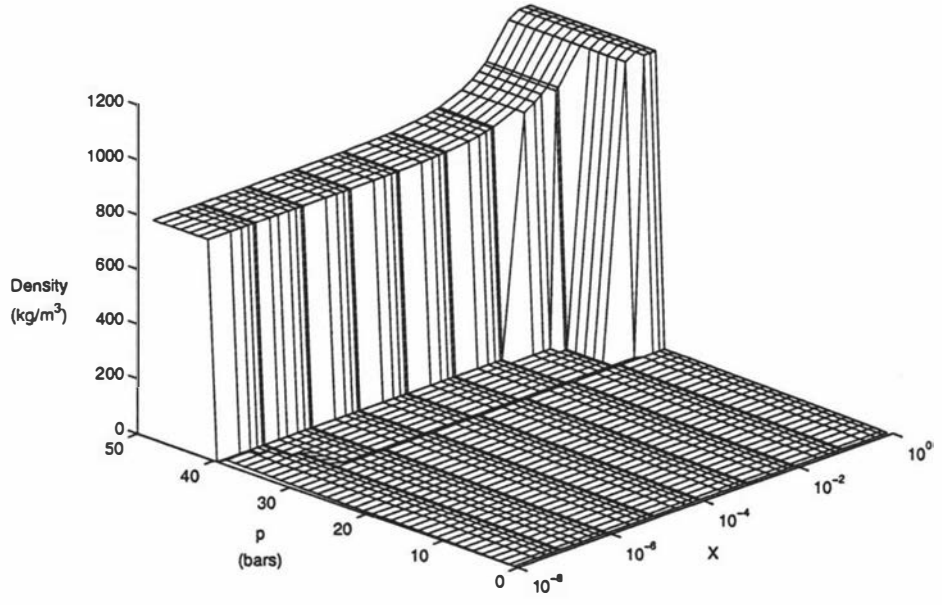

Figure 4.24: The density of brine for $T = 250$ °C. For pictorial clarity ρ is set to zero in Region 5. Pressure lines are plotted for $p = 0.5,\ 1.2\ (1.2)\ 48.0$ bars.

As X increases from 1×10^{-8} to 1×10^{0}:

For $p = 0.5$–19.2, the state point is in Region 3 for all X.

For $p = 20.4$–30.0, the state point starts in Region 8 and finishes in Region 3.

For $p = 31.2$, the state point starts in Region 4, then it moves to Region 5 and finishes in Region 1.

For $p = 32.4$–38.4, the state point starts in Region 4, then it moves to Region 5, then to Region 6 and finishes in Region 1.

For $p = 39.6$, the state point starts in Region 5, then it moves to Region 6 and finishes in Region 1.

For $p = 40.8$–48.0, the state point starts in Region 2b and finishes in Region 1.

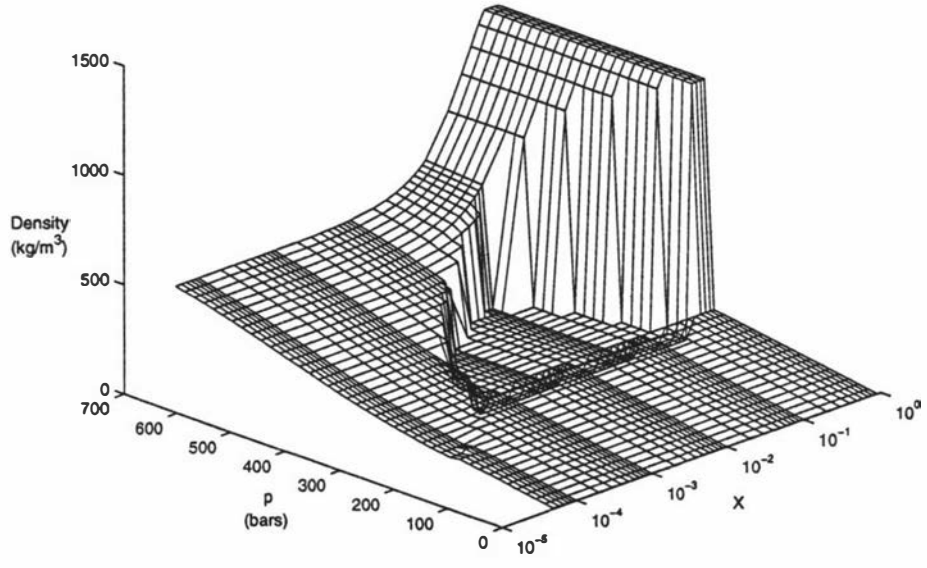

Figure 4.25: The density of brine for $T = 500$ °C. For pictorial clarity ρ is set to zero in Region 5. Pressure lines are plotted for $p = 1,\ 17.5\ (17.5)\ 700$ bars.

As X increases from 1×10^{-5} to 1×10^{0}:

For $p = 1$–175, the state point is in Region 3 for all X.

For $p = 192.5$–297.5, the state point starts in Region 8 and finishes in Region 3.

For $p = 315$–350, the state point starts in Region 4, then it moves to Region 5 and finishes in Region 1.

For $p = 367.5$–577.5, the state point starts in Region 4, then it moves to Region 5, then to Region 6 and finishes in Region 1.

For $p = 595$–700, the state point starts in Region 2a, then it moves to Region 2b and finishes in Region 1.

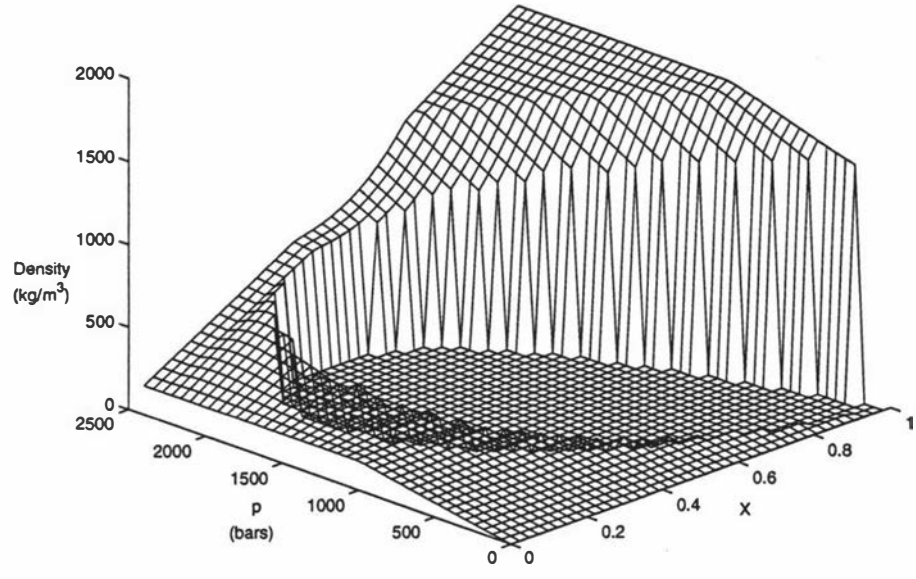

Figure 4.26: The density of brine for $T = 1000$ °C. For pictorial clarity ρ is set to zero in Region 5. Pressure lines are plotted for $p = 1,\ 60\ (60)\ 2400$ bars.

As X increases from 0 to 1:

For $p = 1$, the state point is in Region 4 for all X.

For $p = 60$ and 120, the state point starts in Region 4 and finishes in Region 5.

For $p = 180$–2220, the state point starts in Region 4, then it moves to Region 5 and finishes in Region 6.

For $p = 2280$–2400, the state point starts in Region 2a and finishes in Region 2b.

4.3 Specific enthalpy

A similar approach to that used for density is adopted for the enthalpy calculations, i.e. correlations are developed for the specific enthalpies on the boundaries of the regions and linear interpolation is used between these boundary values in order to determine the enthalpies in the different regions. However there are not as much data available in the literature for the enthalpy as there are for the density.

4.3.1 Water, X = 0

The specific enthalpy of water, $h_w(T, p)$, is calculated from an approximation given by [Saul and Wagner, 1989] that is discussed in [White and Kissling, 1992]. The reference state is the triple point of water, $(T, p) = (0\ °C, 0\ \text{bars})$ approximately. The formulation from Saul and Wagner gives h_w in terms of T and $\rho_w(T, p)$, i.e.

$$h_w = h_w(T, \rho_w(T, p)) = h_w(T, p)$$

See Figure 4.27.

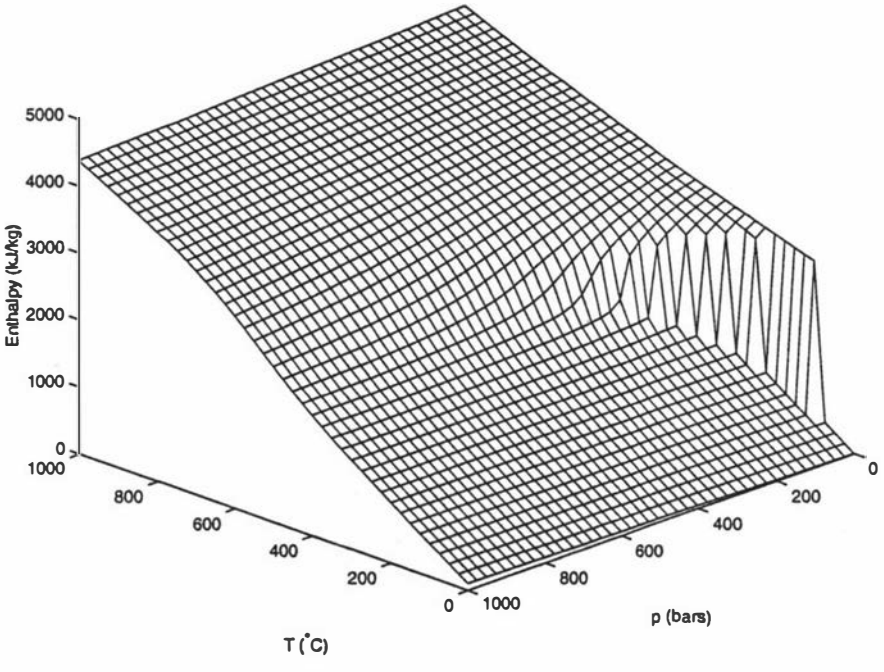

Figure 4.27: Specific enthalpy of water, $h_w(T, p)$, from [Saul and Wagner, 1989], as discussed in [White and Kissling, 1992]. Reference $(T, p) = (0\ °C, 0\ \text{bars})$.

4.3.2 Salt, X = 1

There are little data available for the enthalpy of pure sodium chloride, h_c. [Kaufmann, 1968] and [Stull and Prophet, 1971] both have some data for the molar enthalpy of liquid sodium chloride. The reference temperature in both cases is 25 °C, and the reference pressure is $p = 1$ atm ≈ 1 bar for the Stull and Prophet data and presumably $p = 1$ atm or bar for the Kaufmann data. The data points that fall between 800 and 1465 °C (the normal boiling point) are close to the saturation line for sodium chloride—see Figure 4.4. It is assumed they are on the saturation line, i.e. that they are data points for $h_{c\ell\ sat}(T)$, the saturated liquid specific enthalpy for sodium chloride. In order to establish some points for $h_{cg\ sat}(T)$ (the saturated gas specific enthalpy for sodium chloride), the enthalpy of vapourisation is added to $h_{c\ell\ sat}(T)$ at 1465 °C in order to give $h_{cg\ sat}(T)$ at this same temperature. The same enthalpy of vapourisation is added to $h_{c\ell\ sat}(T)$ at $T = 800$ °C to give $h_{cg\ sat}(T)$ at that temperature. Linear interpolation is now used to approximate $h_{c\ell\ sat}(T)$ and $h_{cg\ sat}(T)$ and the value where they meet at the critical temperature of sodium chloride (3127 °C) is taken to be the critical specific enthalpy of pure sodium chloride. (No published data could be found for this). Figure 4.28 shows the data along with our correlations.

4.3.3 Brine, 0 < X < 1

As for the density, enthalpy data were found for the boundaries of the two-phase region (Region 5—see Figure 4.1) and also a data set was found for the enthalpy of aqueous NaCl solutions.

For the specific enthalpies on the boundaries of Region 5, i.e. the specific enthalpies of the gas phase, $h_{gs}(T,p)$, and liquid phase, $h_{\ell s}(T,p)$, of the two-phase fluid, [Tanger and Pitzer, 1989] have some data for $300 \leq T \leq 600$ °C which they calculated from their equation of state. Their reference state is $(T,\ p) =$ (0 °C, 1 bar). [Haas and Potter, 1977] have some data for $h_{gs}(T,p)$ and $h_{\ell s}(T,p)$ for $T \leq 325$ °C and [Phillips et al., 1981] for $h_{\ell s}(T,p)$ where $T \leq 300$ °C. The reference state for the enthalpies taken from these two papers is $(T,\ p) =$ (0 °C, 0 bars) and their data are from theoretical calculations. The paper by Tanger and Pitzer and that by Haas and Potter have data also for the saturated liquid and gas specific enthalpies of brine, $h_{g\ SAT}(T)$ and $h_{\ell\ SAT}(T)$, and the critical specific

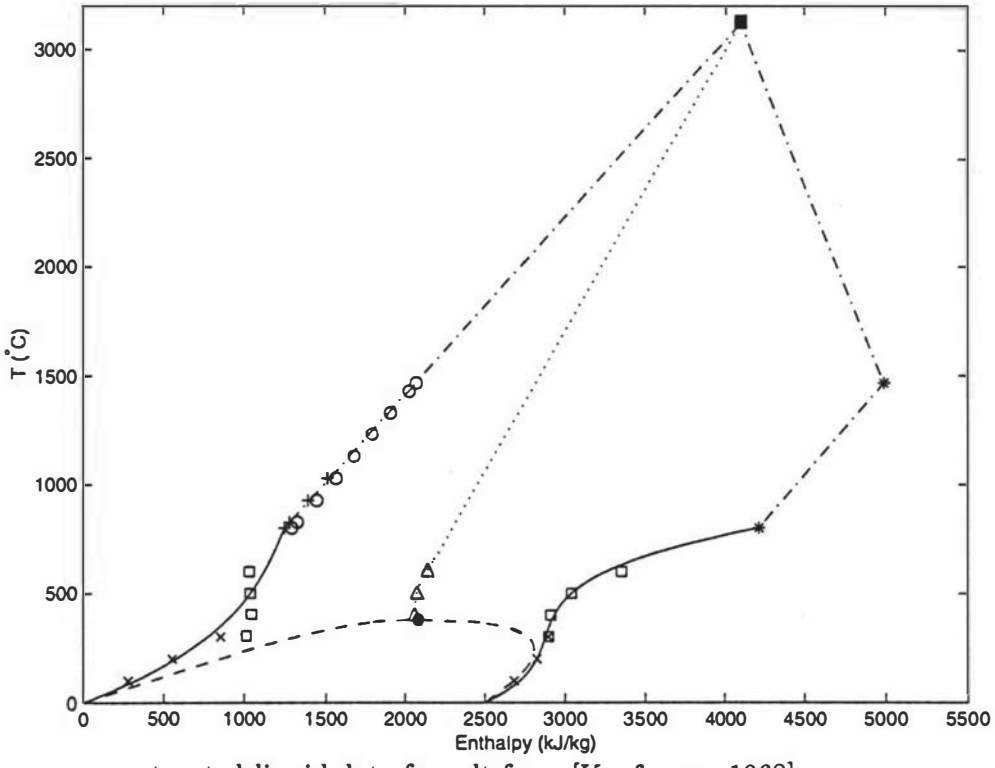

\+ saturated liquid data for salt from [Kaufmann, 1968]. Reference (T, p) = (25 °C, 0 bars).

o saturated liquid data for salt from [Stull and Prophet, 1971]. Reference (T, p) = (25 °C, 0 bars).

* saturated vapour data for salt from our calculations which are based on data from [Kaufmann, 1968] and [Stull and Prophet, 1971]

□ theoretically-calculated saturated liquid and vapour data for brine from [Tanger and Pitzer, 1989]. Reference (T, p) = (0 °C, 1 bar).

△ theoretically-calculated critical data from [Tanger and Pitzer, 1989]

× theoretically-calculated saturated liquid and vapour data for brine from [Haas and Potter, 1977]. Reference (T, p) = (0 °C, 0 bars).

——— our correlations for the saturated brine specific enthalpies, $h_{\ell\ SAT}(T)$ and $h_{g\ SAT}(T)$

— · — · our correlations for the saturated specific enthalpies of salt, $h_{c\ell\ sat}(T)$ and $h_{cg\ sat}(T)$

····· our correlation for the critical specific enthalpy, $h_{CRIT}(T)$

— — — saturated gas and liquid specific enthalpies for water, $h_{wg\ sat}(T)$ and $h_{w\ell\ sat}(T)$

• critical specific enthalpy of H_2O ■ critical specific enthalpy of NaCl

Figure 4.28: The critical specific enthalpy of brine and the saturated liquid and vapour specific enthalpies of water, brine and salt.

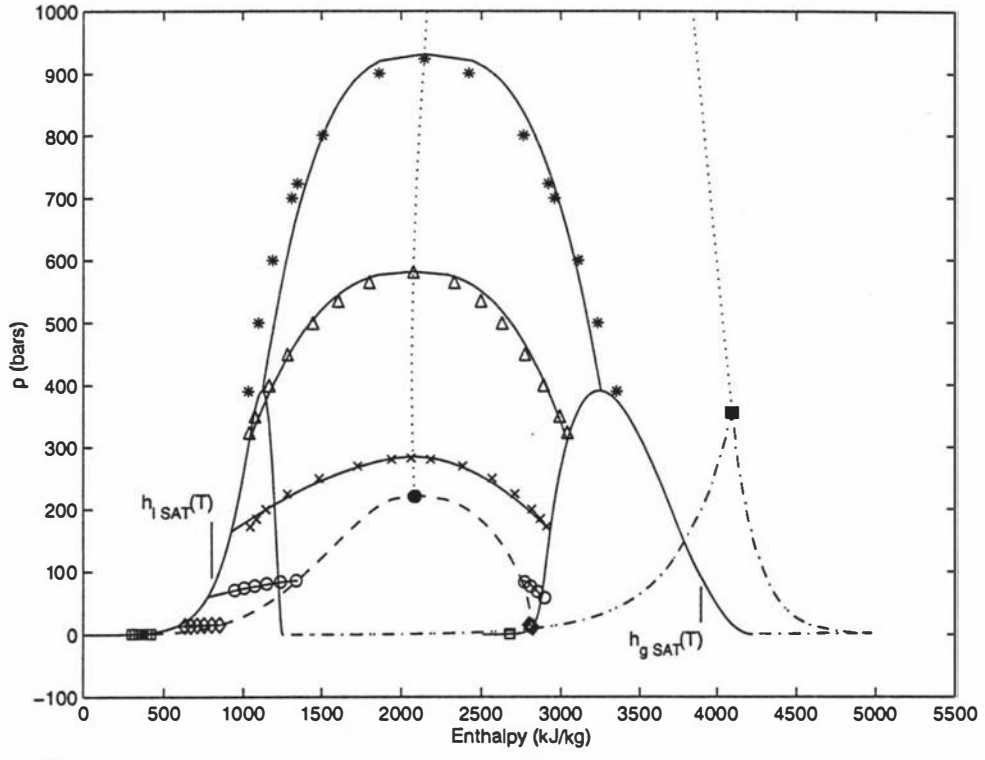

*

□, ◇, ○, ×, △, * T = 100, 200, 300, 400, 500 and 600 °C respectively

——— our correlations for $h_{gs}(T,p)$ and $h_{\ell s}(T,p)$

— — — proj. of saturated gas and liquid specific enthalpies for water, $h_{wg\ sat}(T)$ and $h_{w\ell\ sat}(T)$

— · — · proj. of saturated gas and liquid specific enthalpies for sodium chloride, $h_{cg\ sat}(T)$ and $h_{c\ell\ sat}(T)$

· · · · · proj. of critical specific enthalpy, $h_{CRIT}(T)$, of brine

● critical specific enthalpy of H_2O

■ critical specific enthalpy of NaCl

Figure 4.29: Correlations for the specific enthalpies of the gas phase, $h_{gs}(T,p)$, and liquid phase, $h_{\ell s}(T,p)$, for the two-phase fluid. Values are plotted as isotherms for T = 100 (100) 600 °C. The data for T = 400–600 °C are from [Tanger and Pitzer, 1989] whose reference (T, p) = (0 °C, 1 bar). For T = 100, 200 and 300 °C, the data for $h_{gs}(T,p)$ are from [Haas and Potter, 1977] and for $h_{\ell s}(T,p)$ the data are from [Phillips et al., 1981]. The reference (T, p) = (0 °C, 0 bars) for both papers. All data are from theoretical calculations.

enthalpy of brine, $h_{CRIT}(T)$. Figures 4.28 and 4.29 show the data and our correlations for these various enthalpies. [Michaelides, 1981] has a correlation for $h_{\ell s}(T,p)$, which according to [Battistelli et al., 1997], is valid for $100 \leq T \leq 350$ °C. Like our correlation for $h_{\ell s}(T,p)$, Michaelides's correlation closely fits Phillips et al.'s data for $T \leq 300$ °C—see Figure 4.29 for our correlation.

[Pitzer et al., 1983] have data for the enthalpy of aqueous NaCl solutions (Regions 2b and 6). Their reference state is (T, p) = (25 °C, 177 bars).

Although there are some differences among the reference states for the specific enthalpies of water, salt and brine, we assume, with the exception of those for the data of [Pitzer et al., 1983], that the differences are negligible for our purposes.

4.3.4 The specific enthalpy for the regions

Region 1

As for the density there are no data available for the enthalpy of fluid in Region 1, the halite-saturated liquid enthalpy. Therefore, as with the density, the enthalpy for this region is assumed to equal the saturated liquid specific enthalpy on the three-phase surface, i.e.

$$h_{\ell\ sol}(T,p) \;=\; h_{\ell\ SAT}(T)$$

Regions 2 and 6

Regions 2b and 6

It was hoped to use the data of [Pitzer et al., 1983] in order to develop correlations for Regions 2b and 6. As their reference state is considerably different to that for the rest of the data, attempts were made to reconcile their data with the other data. Despite these attempts, the Pitzer et al. data remained inconsistent with the rest of the data sets. It was decided therefore to assume that the enthalpies in Regions 2b and 6 are independent of pressure and let the enthalpies in these regions equal those on the liquid surface of the two-phase region, i.e. $h_{\ell s}(T,p)$.

Region 2a

Since X_{CRIT} is in Region 2b (it is the lower X limit), then the enthalpies in Region 2b at $X = X_{CRIT}(T)$ equal $h_{\ell s}(T, p_{CRIT}(T)) = h_{CRIT}(T)$. To calculate the

enthalpies in Region 2a, linear interpolation is used between $h_w(T,p)$ and $h_{CRIT}(T)$ as follows:

$$\begin{aligned} h_b &= h_b(T,p,X) \\ &= h_w(T,p) + \frac{X}{X_{CRIT}(T)}[h_{CRIT}(T) - h_w(T,p)] \end{aligned}$$

Regions 3, 4, 5, 7 and 8

For these regions, a similar approach to that described in Subsection 4.2.4 for the brine density is used in order to determine the specific enthalpies. This is outlined as follows.

Region 3

The specific enthalpy of the salt-saturated brine gas, $h_{g\ sol}(T,p)$, is given as a fraction of $h_{g\ SAT}(T)$.

$$h_b = h_g(T,p,X_{g\ sol}(T,p)) = h_{g\ sol}(T,p) = h_{g\ SAT}(T)\frac{p}{p_{SAT}(T)}$$

Region 4

Linear interpolation in X is used between $h_w(T,p)$ and $h_{gs}(T,p)$:

$$h_b = h_g(T,p,X) = h_w(T,p) + \frac{X}{X_{gs}(T,p)}[h_{gs}(T,p) - h_w(T,p)]$$

Region 5

Recall that the density in this region is given by:

$$\rho_b = \rho_b(T,p) \quad = \quad (1 - S_\ell)\rho_{gs}(T,p) + S_\ell\rho_{\ell s}(T,p) \tag{4.1}$$

Since h is a mass measure, it is calculated by:

$$\rho_b h_b = \rho_b(T,p)h_b(T,p) = (1 - S_\ell)\rho_{gs}(T,p)h_{gs}(T,p) + S_\ell\rho_{\ell s}(T,p)h_{\ell s}(T,p)$$

where ρ_b is given by Equation (4.1). Dividing through by ρ_b enables h_b for Region 5 to be determined.

Regions 7 and 8

Linear interpolation in X is used between $h_w(T,p)$ and $h_{g\ sol}(T,p)$:

$$h_b = h_g(T,p,X) = h_w(T,p) + \frac{X}{X_{g\ sol}(T,p)}[h_{g\ sol}(T,p) - h_w(T,p)]$$

In Region 7, $X_{g\ sol}(T,p) = 1$.

Therefore based on which of the nine regions the state point is in, specific enthalpies can be calculated for the entire T-p-X brine state space. Figures 4.30 – 4.32 are isothermal projections of the four dimensional T-p-X-h space. The enthalpies are calculated using the equations given in Appendix C. The same three representative temperatures (250, 500 and 1000 °C) are used as for the density. Similarly h is set to zero in Region 5 for pictorial clarity—see Subsection 4.2.4.

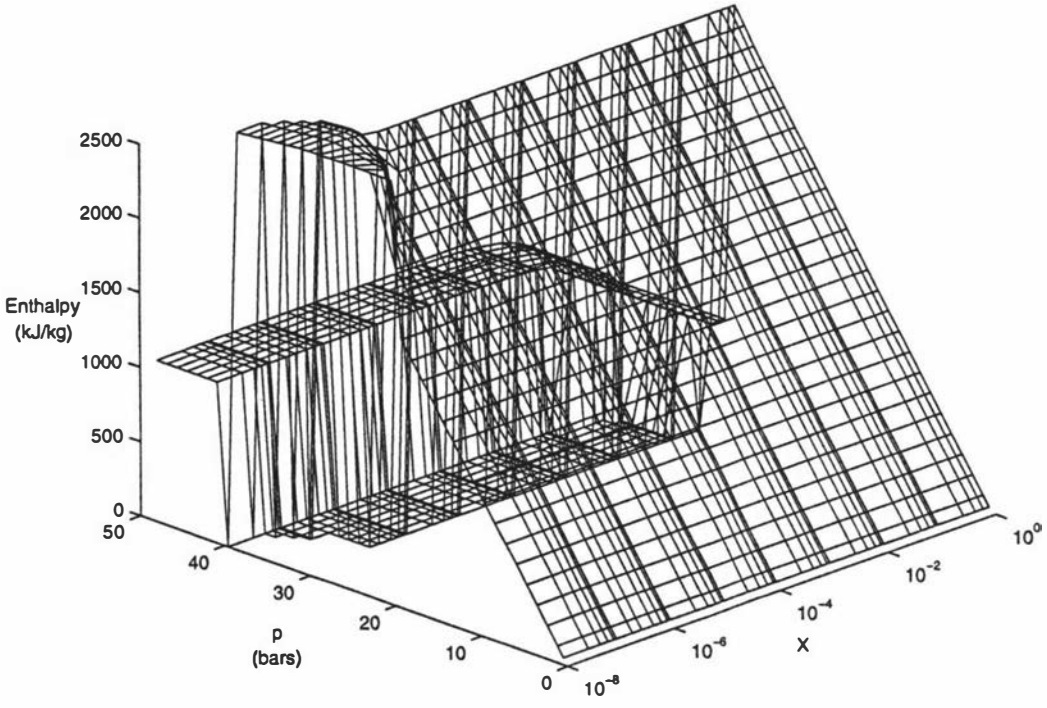

Figure 4.30: The specific enthalpy of brine for $T = 250$ °C. For pictorial clarity h is set to zero in Region 5. Note the logarithmic scale for X. For the regions traversed, see the caption for Figure 4.24.

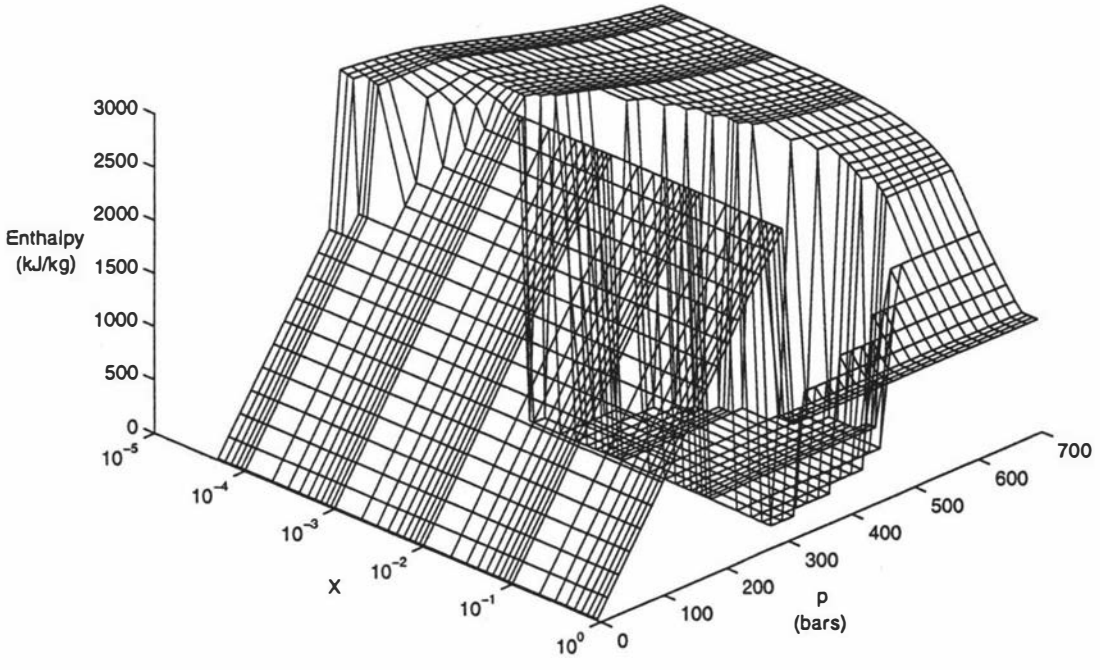

Figure 4.31: The specific enthalpy of brine for $T = 500$ °C. For pictorial clarity h is set to zero in Region 5. Note the logarithmic scale for X. For the regions traversed, see the caption for Figure 4.25.

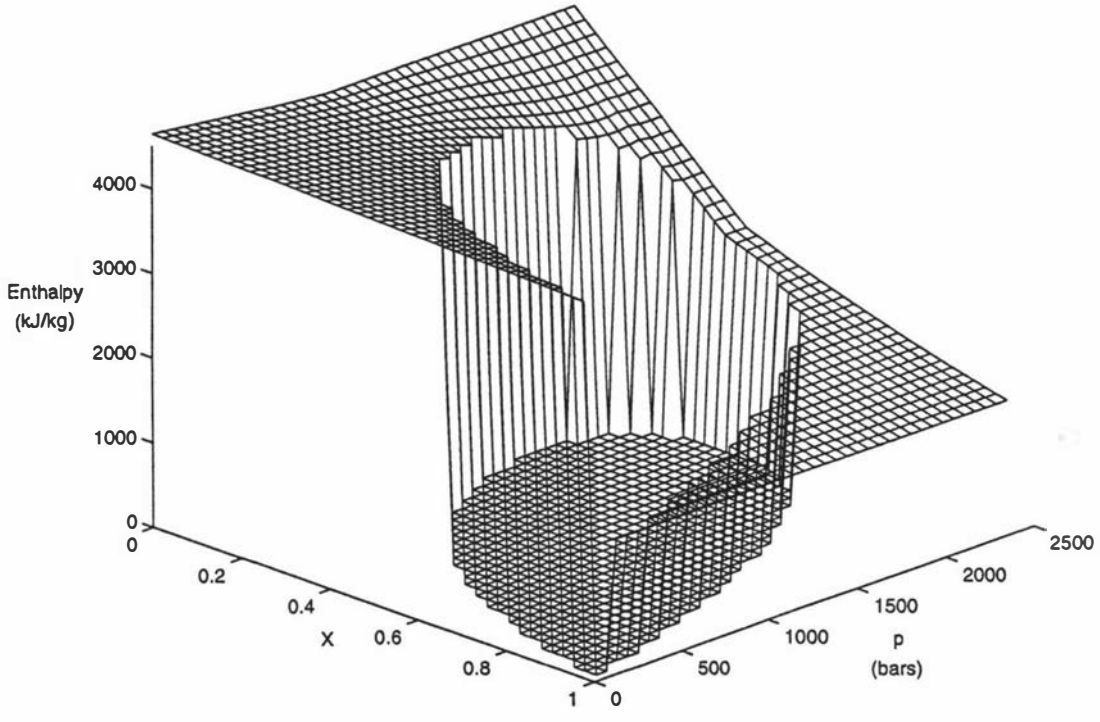

Figure 4.32: The specific enthalpy of brine for $T = 1000\,^{\circ}\mathrm{C}$. For pictorial clarity h is set to zero in Region 5. Note the linear scale for X. For the regions traversed, see the caption for Figure 4.26.

4.4 Dynamic viscosity

Because of the scarcity of data for the dynamic viscosity, particularly at higher temperatures, a different approach to the one used for the density and specific enthalpy is adopted. Rather than interpolating across regions from one region boundary to another, a weighted interpolation is used across the entire T-p-X state space.

4.4.1 Water, X = 0

Based on expressions given by [Schmidt, 1979] which are discussed in [Kissling, 1995], the dynamic viscosity of water (μ_w) is able to be calculated (at least) over the T-p range shown in Figure 4.33, and is a function of temperature and density (ρ_w), i.e.

$$\mu_w = \mu_w(T, \rho_w(T, p)) = \mu_w(T, p)$$

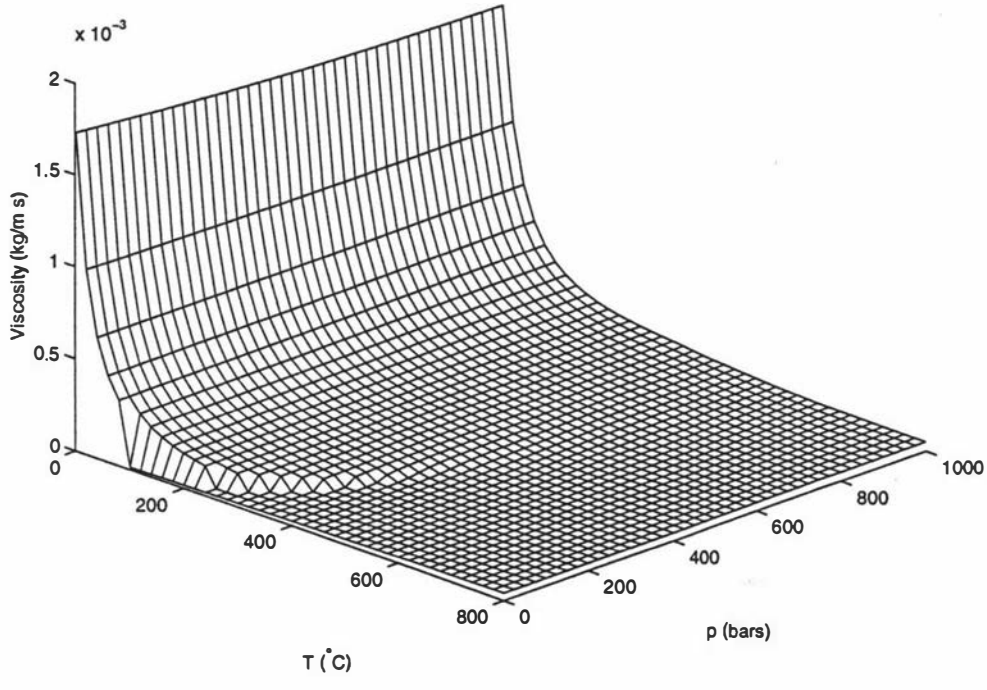

Figure 4.33: Dynamic viscosity of water, $\mu_w(T, p)$, from [Schmidt, 1979], as discussed in [Kissling, 1995].

4.4.2 Salt, X = 1

There are very little data available for pure sodium chloride. Data and a formula for the dynamic viscosity of molten (liquid) sodium chloride, $\mu_{c\ell}$, for a limited range of temperature were found in [Kaufmann, 1968], [Janz, 1988] and [James and Lord, 1992]. It is assumed that the pressure is 1 bar. Figure 4.34 shows the data and a line drawn using Janz's formula, plus a plot of our correlation for $\mu_{c\ell}(T)$. Our correlation is assumed to apply for all p, i.e. not only for liquid sodium chloride, where $p \geq p_{c\ sat}(T)$, but also for sodium chloride gas, where $p < p_{c\ sat}(T)$. It is unlikely however, that $p < p_{c\ sat}(T)$ at these elevated temperatures ($T \geq 800$ °C), so μ_{cg} (the dynamic viscosity of sodium chloride gas) will probably never be required.

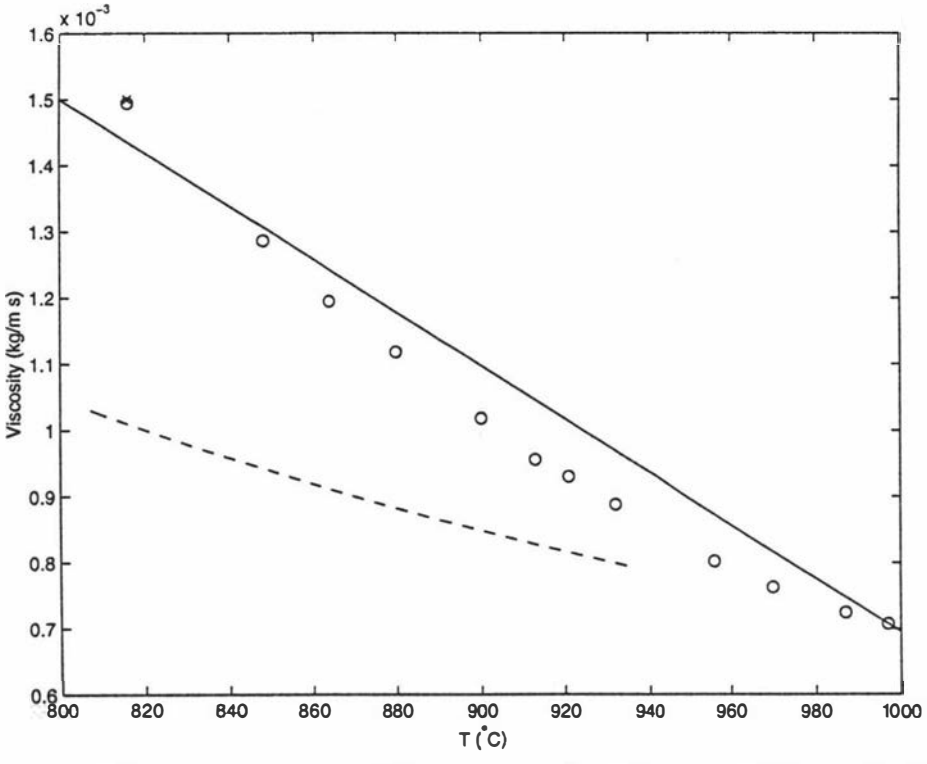

o data from [Kaufmann, 1968] × data from [James and Lord, 1992]
– – – line drawn from formula given in [Janz, 1988]
——— our correlation

Figure 4.34: Dynamic viscosity of NaCl liquid, $\mu_{c\ell}(T)$, at 1 bar. Saturation temperature at 1 bar is 1465 °C.

4.4.3 Brine, $0 < X < 1$

There are not a lot of data available here either, and for the most part the validity ranges for the T, p and X values of this data are not specified. [Potter, 1978], [Phillips et al., 1981], [Alkan et al., 1995] and [Oldenburg et al., 1995] all have correlations which incorporate μ_w.

[Potter, 1978] developed a theoretical model for NaCl solutions which enables the dynamic viscosity of brine (μ_b) to be calculated using the same formulation as that used for μ_w. He does this by using an equation which relates the temperature of brine to that of water at the same pressure. He then uses this calculated water temperature in a formulation for μ_w to give μ_b.

[Phillips et al., 1981] developed a theoretically-based correlation for the dynamic viscosity of aqueous NaCl solutions. They have:

$$\begin{aligned} \mu_b &= \mu_b(T, X, \mu_w(T,p)) \\ &= \mu_b(T, p, X) \end{aligned}$$

[Alkan et al., 1995] have a correlation for the dynamic viscosity of NaCl solutions based on an 'average' geothermal brine (one that is nearly equal to NaCl solution). It has the form:

$$\begin{aligned} \mu_b &= \mu_b(X, \mu_w(T,p)) \\ &= \mu_b(T, p, X) \end{aligned}$$

[Oldenburg et al., 1995] use an empirically-fitted correlation where

$$\mu_b = \mu_w(T,p)[1 + a_1 X + a_2 X^2 + a_3 X^3] \tag{4.2}$$

The a_i's are constants. Equation 4.2 is taken from [Herbert et al., 1988] who study groundwater flow where salt is dissolved in the groundwater. Herbert et al.'s correlation for μ is

$$\mu_b = 1.002 \times 10^{-3}[1 + a_1 X + a_2 X^2 + a_3 X^3] \tag{4.3}$$

This is valid for all X, i.e. $0 \leq X \leq 1$. When $X = 0$, we have pure water and $\mu_b = \mu_w = 1.002 \times 10^{-3}$ kg/m s. The only reference to temperature in Herbert et al.'s paper is in Figure 1, where they compare their correlation for the density of brine with some data at $T = 20$ °C and $p = 1$ atmosphere. Therefore I assume that

Table 4.3: Ranges of T-p-X validity for the various correlations for the dynamic viscosity of brine, μ_b.

Reference	T (°C)	p (bars)	X	Accuracy compared to exptl. data
[Potter, 1978]	Up to 325	Not specified	0 - 0.26	±1% for data up to 150°C
[Phillips et al., 1981]	10 - 350	1 - 500	0 - 0.23	±2%
[Ershaghi et al., 1983]	50 - 275	Not specified	0.01 - 0.17	Not specified
[Alkan et al., 1995]	Not specified	Not specified	Not specified	Not specified
[Oldenburg et al., 1995]	Not specified	Not specified	0 - 1	Not specified

$\mu_w = 1.002 \times 10^{-3}$ kg/m s is the dynamic viscosity of water at (T, p) = (20 °C, 1 atmosphere). This is in fact the case when checked using the expression for μ_w given by [Schmidt, 1979], see Subsection 4.4.1. Oldenburg et al. do not mention the valid temperature range for Equation 4.2, but in their paper they have an example that has temperatures between 200 and 300 °C. Presumably, therefore, Equation 4.2 is valid for these temperatures. I am unsure about the validity of using Equation 4.3 as Oldenburg et al. do for $T > 20$ °C, i.e. for $\mu_w \neq 1.002 \times 10^{-3}$ kg/m s.

[Ershaghi et al., 1983] developed a correlation for the dynamic viscosity of NaCl solutions based on experimental work they did. Here

$$\mu_b = \mu_b(T, X)$$

[Lide, 1996] have data for the dynamic viscosity of aqueous NaCl solutions. X ranges from 0 to 0.26 (room temperature saturation for H_2O-NaCl liquid), and T and p are at 20 °C and 1 bar respectively. Figure 4.35 shows this data along with those correlations whose validity range includes 20 °C and 1 bar. Clearly the correlation of [Phillips et al., 1981] best fits the data from Lide. Because of this and the fact that Phillips et al. specify the T, p and X validity ranges, see Table 4.3, it was decided to use their correlation as a basis for developing a correlation which extrapolates to higher T, p, X values.

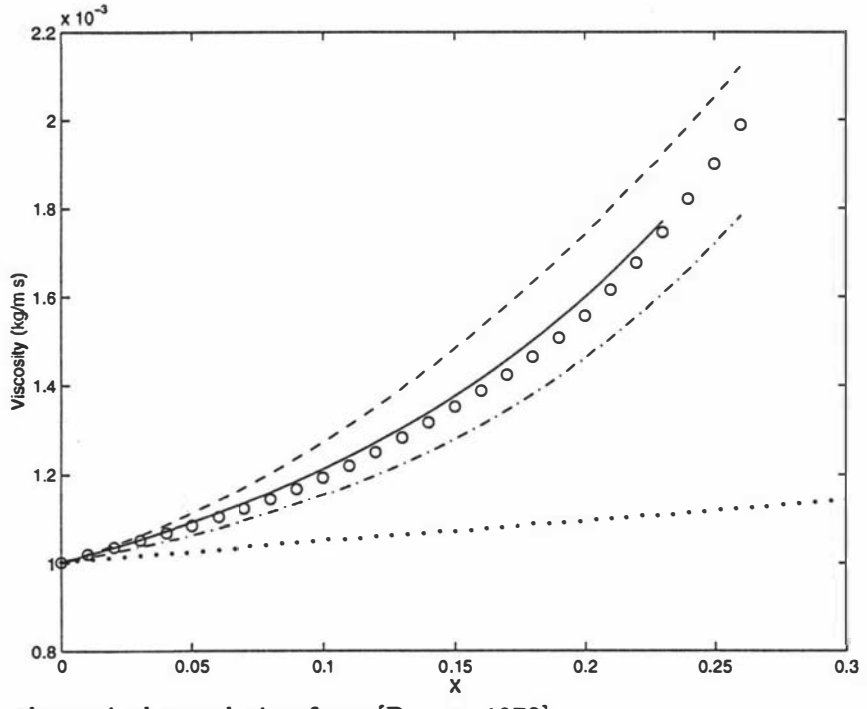

— · — · theoretical correlation from [Potter, 1978]

——— theoretical correlation from [Phillips et al., 1981]

— — — correlation from [Alkan et al., 1995] based on an 'average' geothermal brine (one that is nearly equal to NaCl solution)

· · · · · empirically-fitted correlation from [Oldenburg et al., 1995], this correlation extends to $X = 1$ (pure NaCl).

o data from [Lide, 1996]

Figure 4.35: Dynamic viscosity of aqueous NaCl solutions at 20 °C and 1 bar.

4.4.4 Development of correlations for the brine state space

For $T \geq 800$ °C, the viscosity values are assumed to be given by a linear interpolation between the values of water ($X = 0$) and those of pure salt ($X = 1$). For lower temperatures, in order to qualitatively fit the correlation of [Phillips et al., 1981], a linear extrapolation from water values is used. In order that there be continuity at $T = 800$, the actual calculated dynamic viscosity is a weighted average of the two linear equations—see Appendix B.3. Figure 4.36 compares the correlation of Phillips et al. with our correlation for some selected temperatures.

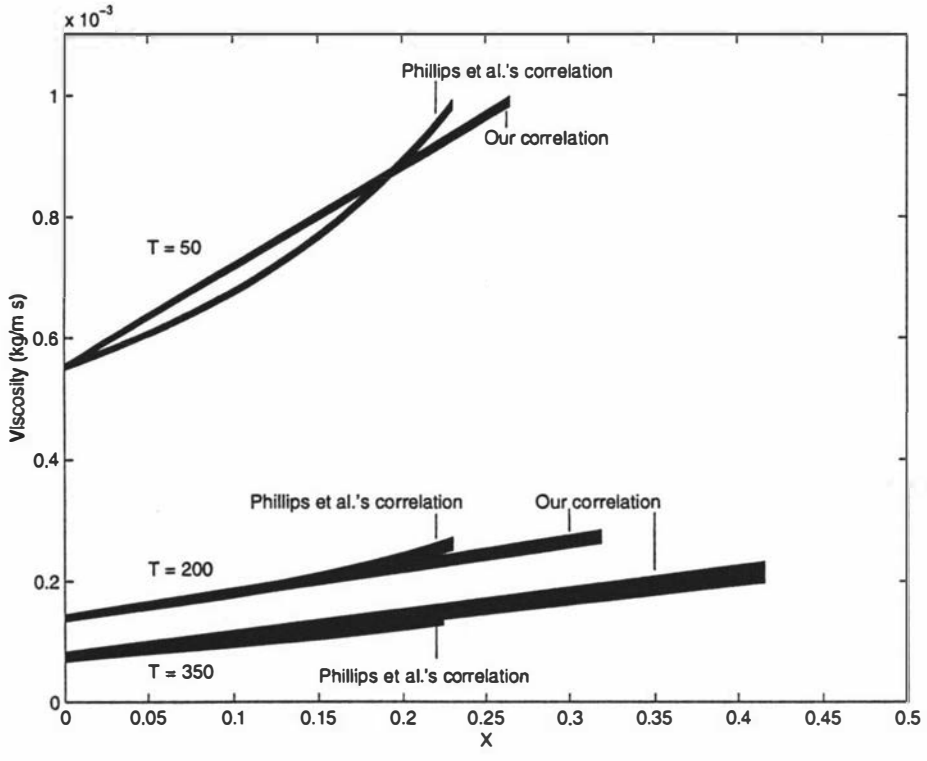

Figure 4.36: Dynamic viscosity of brine for $T = 50$, 200, and 350 °C, $p \leq 500$ bars. Compares our correlation (see Appendix B.3) with that of [Phillips et al., 1981].

For $T \leq 374.15$ °C and $p < p_{CRIT}(T) = p_{w\ sat}(T)$, see Figure 4.1(a), $\mu_w(T, p)$ in our correlation returns the value for the gas phase (see Figure 4.33), since for these T and p values water is in the gas phase; recall that our brine correlation is extrapolated from water values. This is correct for Region 4 (subcritical gas) and Region 8 (unsaturated gas), but not for Region 6 (subcritical liquid). The gas phase value for $\mu_w(T, p)$ is quite different from the liquid phase value which

corresponds to $p \geq p_{CRIT}(T) = p_{w\ sat}(T)$, see Figure 4.33. Therefore in Region 6 it is assumed that,

$$\mu_b(T, p, X) \;=\; \mu_b(T, p_{CRIT}(T), X)$$

that is for Region 6, the viscosity does not change with pressure and equals the viscosity at the critical pressure. This assumption ensures that for Region 6 with $T \leq 374.15$ °C and $p < p_{CRIT} = p_{w\ sat}$, we get the liquid values for μ_w.

Once the temperature becomes supercritical, i.e. $T > 374.15$ °C, water of course does not have two phases. However in order to be consistent and to ensure that we obtain the more 'liquid-like' values for μ_w in Region 6, the above assumption holds for $T > 374.15$ °C, i.e. $\mu_b(T, p, X) = \mu_b(T, p_{CRIT}(T), X)$ for $T > 374.15$ °C also.

Figures 4.37 – 4.39 are isothermal projections of the four dimensional T-p-X-μ space. The same three representative temperatures (250, 500 and 1000 °C) are used as for the density and specific enthalpy, with μ being set to zero in Region 5 for pictorial clarity—see Subsection 4.2.4. The viscosities are calculated using the equations given in Appendix C.

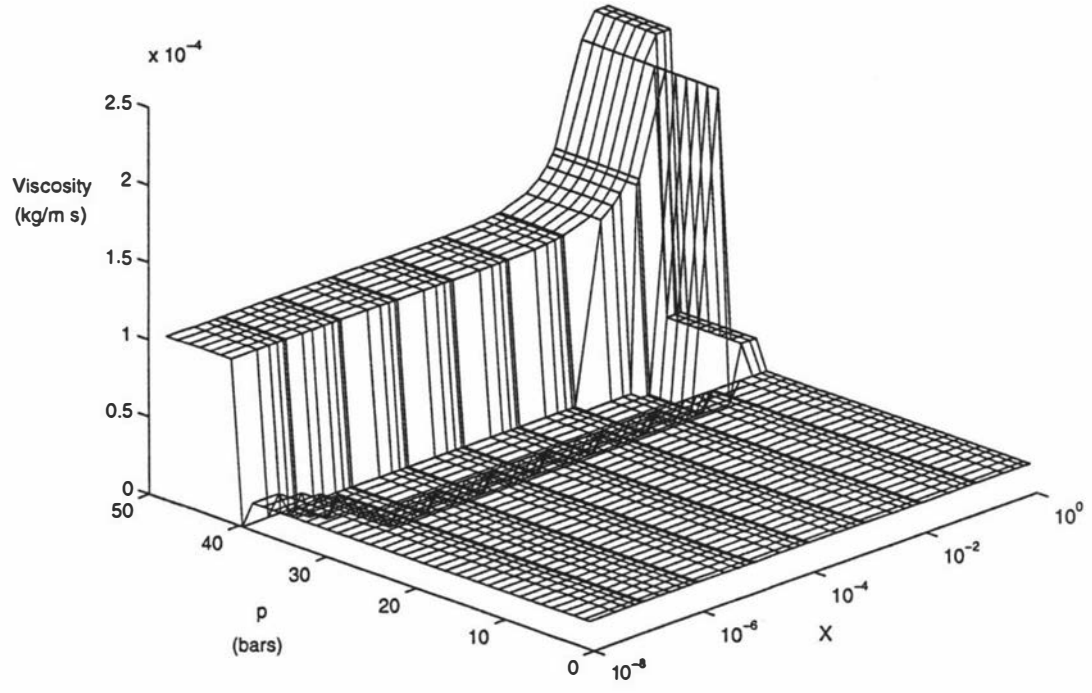

Figure 4.37: The dynamic viscosity of brine for $T = 250$ °C. For pictorial clarity μ is set to zero in Region 5. Note the logarithmic scale for X. For the regions traversed, see the caption for Figure 4.24.

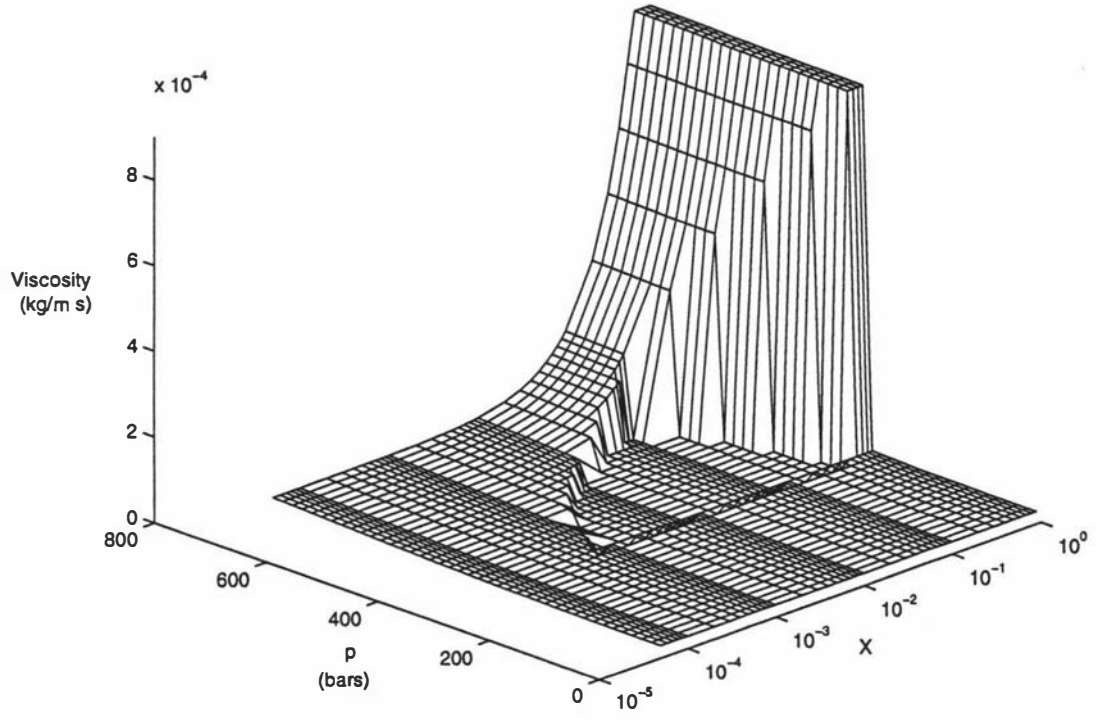

Figure 4.38: The dynamic viscosity of brine for $T = 500$ °C. For pictorial clarity μ is set to zero in Region 5. Note the logarithmic scale for X. For the regions traversed, see the caption for Figure 4.25.

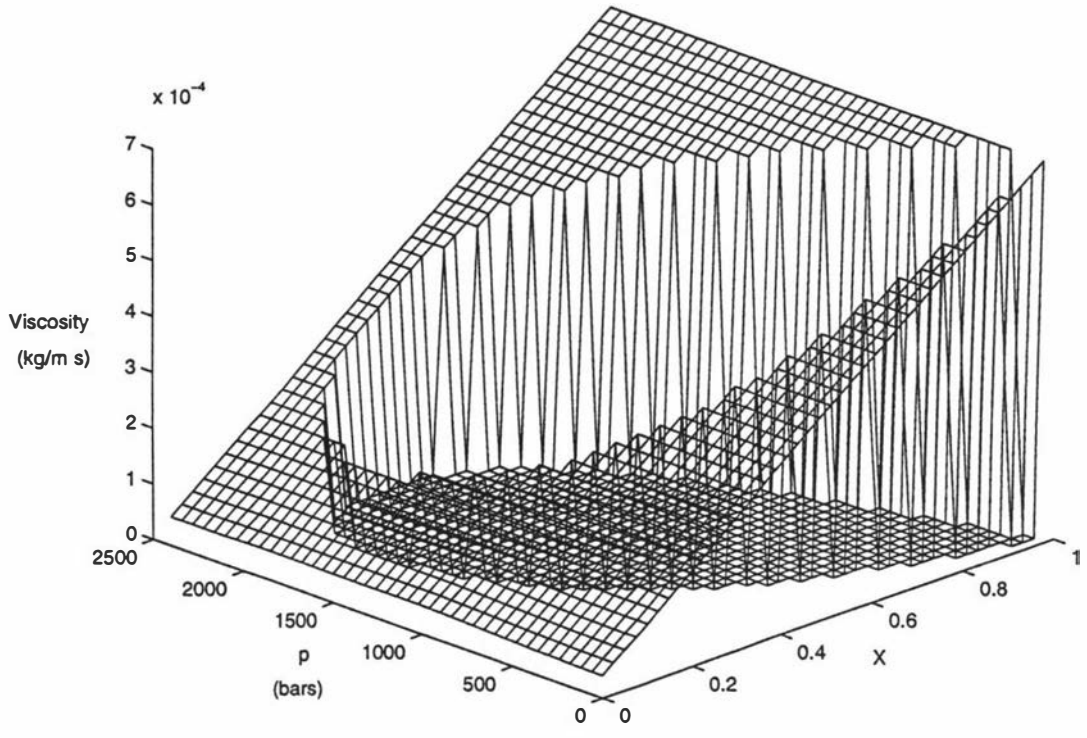

Figure 4.39: The dynamic viscosity of brine for $T = 1000$ °C. For pictorial clarity μ is set to zero in Region 5. Note the linear scale for X. For the regions traversed, see the caption for Figure 4.26.

4.5 Summary

This chapter has described newly-developed correlations for ρ, h and μ of brines over a wide T-p-X range, whose qualitative behaviour is correct. For example, given T, both the density and dynamic viscosity mostly increase with p and X (see Figures 4.24 – 4.26 and 4.37 – 4.39). Some of the published data has diverging trends and this has made it difficult to determine some of the correlations. For example, in Figures 4.19 – 4.22, $\rho_{\ell s}(T,p)$ is often greater than some values of ρ_b, where $p_{\ell s}(T,X)$ is less than the pressures at which ρ_b is measured. At higher temperatures particularly, our correlations do not fit the data as well as we would like, but qualitatively our correlations remain correct. However as pointed out in the discussion on our model fluid (see Section 2.1), the composition of geothermal fluids is not accurately known, and we are modelling such fluids by representing their solutes by the main solute, NaCl. Therefore it may not matter if our correlations do not fit the data for pure H_2O-NaCl systems exactly, as long as the qualitative aspects are accounted for and are accurate.

The combined set of correlations set out in this chapter and the previous one enable the state space delineations and the thermodynamic properties of the H_2O-NaCl system to be readily calculated from simple algebraic formulae in terms of the primary state variables T, p and X. The correlations will enable us to model the flow of deep geothermal brines as well as flows that are closer to the Earth's surface. The correlations for the thermodynamic properties on the boundaries of the state space are given in Appendix B, while the equations that calculate the thermodynamic properties for the regions are set out in Appendix C.

The next step is to incorporate the formulae in computer subroutines which may be used in the numerical simulation of fluid flow in geothermal systems. The next chapter does this for the relatively simple case of steady 1-D flows.

Chapter 5

Simulations

5.1 Introduction

The relatively simple case of 1-D steady (fluid flow does not change over time) flow is described in this chapter and then used to test our correlations for the state space delineations and the thermodynamic properties. By 'test', we mean that two examples of such flows, each with different sets of boundary conditions and parameters, are chosen in such a way that six of the nine regions describing the brine state space are traversed by the state points, and hence we are able to check that the correlations are working (giving plausible results) in these regions. In order to model flow through regions where deposition (or dissolution) of sodium chloride occurs, then for these 1-D steady-state examples, some assumptions are made concerning the nature of the flow and the rock matrix. Being 1-D makes the examples theoretical and also their boundary conditions and parameters are probably not typical of real geothermal systems. The equations used in this chapter to describe these vertical steady flows, are special cases of the multidimensional time-dependent ones given in Chapter 2, where we developed our model. The work in this chapter further develops the modelling outlined in [McKibbin and McNabb, 1995a].

5.2 Equations describing vertical flow

In this section, we take the conservation equations of mass, linear momentum and energy, that were developed in Chapter 2, in order to describe the fluid flow through a fluid-saturated porous medium, and rewrite them for vertical (z-direction) flows

with no sources or sinks.

The conservation of mass is described by Equations (2.3) and (2.4) from Subsection 2.3.2. For water and sodium chloride, these are, respectively:

$$\frac{\partial A_m^w}{\partial t} + \nabla \cdot \mathbf{Q}_m^w - q_m^w = 0$$

$$\frac{\partial A_m^c}{\partial t} + \nabla \cdot \mathbf{Q}_m^c - q_m^c = 0$$

For the meaning of the symbols in the above equations and in the rest of this section, refer to Chapter 2 or the nomenclature list at the beginning of the thesis.

Rewriting the above equations for the case of vertical (z) flow with no sources or sinks gives:

$$\frac{\partial A_m^w}{\partial t} + \frac{\partial Q_m^w}{\partial z} = 0 \tag{5.1}$$

$$\frac{\partial A_m^c}{\partial t} + \frac{\partial Q_m^c}{\partial z} = 0 \tag{5.2}$$

Substituting for A_m^w and A_m^c, the mass of water and sodium chloride per unit volume, from Equations (2.6) and (2.7) respectively, we have:

$$\frac{\partial}{\partial t}\{\phi\varepsilon[S_\ell(1-X_\ell)\rho_\ell + (1-S_\ell)(1-X_g)\rho_g]\} + \frac{\partial}{\partial z}Q_m^w = 0 \tag{5.3}$$

$$\frac{\partial}{\partial t}\{\phi\varepsilon[S_\ell X_\ell \rho_\ell + (1-S_\ell)X_g\rho_g] + \phi(1-\varepsilon)\rho_c\} + \frac{\partial}{\partial z}Q_m^c = 0 \tag{5.4}$$

The vertical mass fluxes per unit area, Q_m^w and Q_m^c are, from Subsection 2.3.2,

$$Q_m^w = Q_{m\ell}^w + Q_{mg}^w = (1-X_\ell)Q_{m\ell} + (1-X_g)Q_{mg} \tag{5.5}$$

$$Q_m^c = Q_{m\ell}^c + Q_{mg}^c = X_\ell Q_{m\ell} + X_g Q_{mg} \tag{5.6}$$

The mass fluxes corresponding to the liquid and gas phases, $Q_{m\ell}$ and Q_{mg}, are given by Equations (2.10) and (2.11):

$$Q_{m\ell} = Q_{m\ell}^w + Q_{m\ell}^c = k_{r\ell}\frac{k}{\nu_\ell}(-\frac{\partial p}{\partial z} + \rho_\ell g) \tag{5.7}$$

$$Q_{mg} = Q_{mg}^w + Q_{mg}^c = k_{rg}\frac{k}{\nu_g}(-\frac{\partial p}{\partial z} + \rho_g g) \tag{5.8}$$

For the conservation of energy, the analogous equation to Equations (5.1) and (5.2) is (see Equation (2.12) in Subsection 2.3.2):

$$\frac{\partial A_e}{\partial t} + \frac{\partial Q_e}{\partial z} = 0 \tag{5.9}$$

Substituting for A_e, the energy per unit volume of the fluid-saturated porous medium, from Equation (2.13), we obtain:

$$\frac{\partial}{\partial t}[(1-\phi)\rho_r u_r + \phi\{\varepsilon[S_\ell \rho_\ell u_\ell + (1-S_\ell)\rho_g u_g] + (1-\varepsilon)\rho_c u_c\}] + \frac{\partial}{\partial z}Q_e = 0 \tag{5.10}$$

Q_e, the energy flux per unit area, is given by Equation (2.14):

$$Q_e = Q_{m\ell} h_\ell + Q_{mg} h_g - K\frac{\partial T}{\partial z} \tag{5.11}$$

5.3 Steady vertical flow for the regions

In all the regions where the fluid is unsaturated with respect to NaCl, i.e. Regions 2a, 2b, 4, 5, 6, 7 and 8 (see Figure 4.1 and Table 4.1 of Chapter 4), the voidage (ε) equals 1. All the other terms in the expressions for A_m^w, A_m^c and A_e are either also constant or independent of time (flow is assumed to be steady)—see Equations (5.3), (5.4) and (5.10). Equations (5.3), (5.4) and (5.10) become:

$$\frac{dQ_m^w}{dz} = 0 \Rightarrow Q_m^w = \textit{constant} \tag{5.12}$$

$$\frac{dQ_m^c}{dz} = 0 \Rightarrow Q_m^c = \textit{constant} \tag{5.13}$$

$$\frac{dQ_e}{dz} = 0 \Rightarrow Q_e = \textit{constant} \tag{5.14}$$

In the other two regions (Regions 1 and 3) where deposition or dissolution of NaCl may occur, ε and ϕ may vary with depth and time, i.e. $\varepsilon = \varepsilon(z,t)$, $\phi = \phi(z,t)$ and $0 < \varepsilon \leq 1$. In these regions the time derivative terms are not identically zero.

We assume that Regions 2a and 2b (the supercritical regions) are single-phase liquid, that K, k, ρ_r and ρ_c are constants and that the specific internal energies of the solid rock and sodium chloride are given by:

$$u_i = \int_0^T c_i(\tau)d\tau$$

where $i = r$ (rock) or c (sodium chloride) and c_i is the specific heat (at constant volume) of i. The solution method is now described for each of the regions. These methods enable vertical T, p and X profiles to be obtained after being given an initial state point, or (T, p, X) point, in the brine state space.

5.3.1 Single-phase liquid (Regions 2a, 2b and 6)

Here $Q_{mg} = 0$ and $X = X_\ell$. Therefore from Equations (5.5), (5.6), (5.12) and (5.13), we have:

$$\begin{aligned} Q_m^w &= Q_{m\ell}^w = (1-X)Q_{m\ell} = constant = m_w \\ Q_m^c &= Q_{m\ell}^c = XQ_{m\ell} = constant = m_c \end{aligned}$$

Therefore $X = X_\ell$ is constant, and

$$m_c = \frac{X}{1-X} m_w \tag{5.15}$$

Equations (5.11) and (5.14) give us:

$$Q_e = Q_{m\ell} h_\ell - K\frac{dT}{dz} = constant = q \tag{5.16}$$

In these regions $k_{r\ell} = 1$ and $k_{rg} = 0$, so that Equation (5.7) becomes:

$$Q_m = Q_{m\ell} = m_w + m_c = \frac{k}{\nu_\ell}\left(-\frac{dp}{dz} - \rho_\ell g\right) \tag{5.17}$$

since g, the acceleration due to gravity, is acting downwards in the negative z direction.

Therefore from Equation (5.16) we obtain:

$$\begin{aligned} \frac{dT}{dz} &= \frac{1}{K}(Q_{m\ell} h_\ell - q) \\ &= \frac{1}{K}[(m_w + m_c)h_\ell - q] \\ &= \frac{1}{K}\left[\left(\frac{1}{1-X}\right) m_w h_\ell - q\right] \end{aligned}$$

And Equation (5.17) gives us:

$$\begin{aligned} \frac{dp}{dz} &= -\frac{\nu_\ell}{k}(m_w + m_c) - \rho_\ell g \\ &= -\frac{\nu_\ell}{k}\left(\frac{1}{1-X}\right) m_w - \rho_\ell g \end{aligned}$$

Numerical integration gives vertical T and p profiles. X remains constant with depth, while $S_\ell = 1$ and $\varepsilon = 1$.

5.3.2 Single-phase gas (Regions 4, 7 and 8)

In these regions $Q_{m\ell} = 0$, $X = X_g$ is constant, $k_{rg} = 1$ and $k_{r\ell} = 0$. We obtain similar equations to those above, but subscript ℓ is replaced by g. Similarly vertical T and p profiles are obtained and X is constant with depth. $S_\ell = 0$ and $\varepsilon = 1$.

5.3.3 Two-phase gas + liquid (Region 5)

The situation here is not as straightforward as that pertaining to the single-phase regions. ε remains 1, but $0 < S_\ell < 1$ and $X_{gs} < X < X_{\ell s}$. $(X_\ell = X_{\ell s}, X_g = X_{gs})$. S_ℓ, X, k_{rg} and $k_{r\ell}$ are unknown and need to be determined. This will be discussed shortly.

From Equations (5.5) and (5.12) we have:

$$\begin{aligned} Q_m^w &= Q_{m\ell}^w + Q_{mg}^w \\ &= (1 - X_{\ell s})Q_{m\ell} + (1 - X_{gs})Q_{mg} = constant = m_w \end{aligned} \tag{5.18}$$

And Equations (5.6) and (5.13) give us:

$$\begin{aligned} Q_m^c &= Q_{m\ell}^c + Q_{mg}^c \\ &= X_{\ell s}Q_{m\ell} + X_{gs}Q_{mg} = constant = m_c \end{aligned} \tag{5.19}$$

As in the single-phase regions, m_c is calculated from X and m_w using Equation (5.15). From Equations (5.11) and (5.14) we obtain:

$$Q_e = Q_{m\ell}h_{\ell s} + Q_{mg}h_{gs} - K\frac{dT}{dz} = constant = q \tag{5.20}$$

The mass fluxes for each phase are obtained from Equations (5.7) and (5.8):

$$Q_{m\ell} = Q_{m\ell}^w + Q_{m\ell}^c = k_{r\ell}\frac{k}{\nu_{\ell s}}\left(-\frac{dp}{dz} - \rho_{\ell s}g\right) \tag{5.21}$$

$$\Rightarrow \frac{dp}{dz} = -\frac{\nu_{\ell s}}{k_{r\ell}k}Q_{m\ell} - \rho_{\ell s}g \tag{5.22}$$

$$Q_{mg} = Q_{mg}^w + Q_{mg}^c = k_{rg}\frac{k}{\nu_{gs}}\left(-\frac{dp}{dz} - \rho_{gs}g\right) \tag{5.23}$$

$$\Rightarrow \quad \frac{dp}{dz} = -\frac{\nu_{gs}}{k_{rg}k}Q_{mg} - \rho_{gs}g \tag{5.24}$$

We now have two expressions for dp/dz (for the single-phase regions we only had one), and they need to be equal for consistency. The consistency condition is found by using Equations (5.18), (5.19), (5.21) and (5.23) and one method is as follows. Equations (5.18) and (5.19) are summed to give:

$$m_w + m_c = Q_{m\ell} + Q_{mg} \tag{5.25}$$

Expressions for $Q_{m\ell}$ and Q_{mg} from Equations (5.21) and (5.23) are substituted into Equation (5.25) and this is now solved for dp/dz. $Q_{m\ell}$ and Q_{mg} from Equations (5.21) and (5.23) are substituted into Equation (5.19), and this is also solved for dp/dz. These two expressions for dp/dz are equated to obtain the consistency condition:

$$\begin{aligned} k_{r\ell}k_{rg}(\rho_{\ell s} - \rho_{gs})(X_{\ell s} - X_{gs}) - (k_{r\ell}X_{\ell s}\nu_{gs} + k_{rg}X_{gs}\nu_{\ell s})\frac{m_w + m_c}{gk} \\ +(k_{r\ell}\nu_{gs} + k_{rg}\nu_{\ell s})\frac{m_c}{gk} = 0 \end{aligned} \tag{5.26}$$

The unknowns in Equation (5.26), $k_{r\ell}$ and k_{rg}, are functions of S_ℓ, where $0 < S_\ell < 1$. For given T and p, S_ℓ is adjusted so that Equation (5.26) is satisfied. The vertical pressure gradient, dp/dz, is then given by either Equation (5.22) or (5.24); numerical integration is used to obtain a value for p at a nearby point on the column.

In order to obtain dT/dz and then use numerical integration to obtain a new T value, Equation (5.20) is rearranged to give

$$\frac{dT}{dz} = \frac{1}{K}(Q_{m\ell}h_{\ell s} + Q_{mg}h_{gs} - q)$$

and $Q_{m\ell}$ and Q_{mg} are obtained from Equations (5.21) and (5.23) after dp/dz has been determined.

Unlike the single-phase regions, X varies with depth in this two-phase region, and is constrained by $X_{\ell s}$ and X_{gs}, i.e. $X_{gs} < X < X_{\ell s}$. Each new value of X is calculated using Equation (2.8) from Subsection 2.3.2 with $\varepsilon = 1$, i.e.,

$$X = \frac{S_\ell X_{\ell s}\rho_{\ell s} + (1 - S_\ell)X_{gs}\rho_{gs}}{S_\ell \rho_{\ell s} + (1 - S_\ell)\rho_{gs}} \tag{5.27}$$

5.3.4 Saturated liquid + solid sodium chloride (Region 1)

In this region, where the liquid is saturated with NaCl, deposition or dissolution of NaCl may occur and, as discussed above, ε and ϕ then vary with time and depth so that Equations (5.12) - (5.14) are not valid. Here $Q_{mg} = 0$, $X_{\ell\ sol}(T,p) = X_{\ell\ SAT}(T) \leq X < 1$ and $S_\ell = 1$. In order to provide a consistent solution through all the regions for steady vertical flows, it needs to be assumed for Region 1 (and also Region 3, see below) that the mass flux of water, Q_m^w, is constant with depth and further that the rock matrix expands in order to accomodate deposition. (If deposition of salt occurs, then eventually the pore spaces will diminish and permeability will be compromised, maybe to the extent of there being no flow.) These assumptions may be non-physical and in reality, flow incorporating deposition is most likely to be non-steady, and requires fully 3-D time-dependent analysis.

From Equation (5.3), we obtain:

$$\frac{\partial}{\partial t}[\phi\varepsilon(1 - X_{\ell\ SAT})\rho_{\ell\ SAT}] + \frac{d}{dz}Q_m^w = 0 \tag{5.28}$$

As stated above, Q_m^w is assumed constant with depth, and the flow and fluid salinity distribution do not vary with time; Equation (5.28) then becomes:

$$\begin{aligned} & \frac{\partial}{\partial t}[\phi\varepsilon(1 - X_{\ell\ SAT})\rho_{\ell\ SAT}] = 0 \\ \Rightarrow\ & (1 - X_{\ell\ SAT})\rho_{\ell\ SAT}\frac{\partial}{\partial t}(\phi\varepsilon) = 0 \\ \Rightarrow\ & \frac{\partial}{\partial t}(\phi\varepsilon) = 0 \end{aligned} \tag{5.29}$$

As discussed in Subsection 2.3.2 of Chapter 2, the product $\phi\varepsilon$ gives the volume available for fluid flow within the rock matrix, and from Equation (5.29) we know that this volume, or effective porosity as it is known, remains constant with time in our model. In order for this to hold, it is assumed that the rock matrix expands as discussed above. The effective porosity may vary with depth however. (In this steady state model, only deposition occurs and not dissolution.)

Similar to the single-phase liquid case, see Subsection 5.3.1, except that here $m_c \neq constant$, we have:

$$\begin{aligned} Q_m^w &= Q_{m\ell}^w = (1 - X_{\ell\ SAT})Q_{m\ell} = constant = m_w \\ Q_m^c &= Q_{m\ell}^c = X_{\ell\ SAT}Q_{m\ell} = m_c \end{aligned}$$

Therefore

$$m_c = \frac{X_{\ell\ SAT}}{1 - X_{\ell\ SAT}} m_w \tag{5.30}$$

And

$$Q_m = Q_{m\ell} = m_w + m_c = \frac{k}{\nu_{\ell\ SAT}} \left(-\frac{dp}{dz} - \rho_{\ell\ SAT} g \right)$$

$$\Rightarrow \frac{dp}{dz} = -\frac{\nu_{\ell\ SAT}}{k} \left(\frac{1}{1 - X_{\ell\ SAT}} \right) m_w - \rho_{\ell\ SAT} g \tag{5.31}$$

Equation (5.11) gives:

$$Q_e = (m_w + m_c) h_{\ell\ SAT} - K \frac{dT}{dz} = q$$

$$\Rightarrow \frac{dT}{dz} = \frac{1}{K} \left[\left(\frac{1}{1 - X_{\ell\ SAT}} \right) m_w h_{\ell\ SAT} - q \right] \tag{5.32}$$

Numerical integration gives vertical T and p profiles. The profile for the mass fraction of sodium chloride in the saturated liquid is given by $X_{\ell\ sol}(T, p) = X_{\ell\ SAT}(T)$. For details on the calculation of ε and X (which lies between $X_{\ell\ SAT}$ and 1 and includes the solid NaCl precipitate), see [McKibbin and McNabb, 1995a].

The deposition rate of NaCl, or volumetric expansion rate, is the relative change in volume per unit time and since ϕ is small, is given closely by $\partial\phi/\partial t$, see [McKibbin and McNabb, 1998]. The conservation of mass for the NaCl component of the fluid, from Equation (5.4), gives:

$$\frac{\partial}{\partial t} [\phi \varepsilon X_{\ell\ SAT} \rho_{\ell\ SAT} + \phi(1 - \varepsilon) \rho_c] + \frac{d}{dz} Q_m^c = 0$$

Using Equations (5.29) and (5.30) and the assumption that the flow is steady, then this equation reduces to:

$$\rho_c \frac{\partial \phi}{\partial t} + \frac{dm_c}{dz} = 0$$

$$\Rightarrow \frac{\partial \phi}{\partial t} = -\frac{1}{\rho_c} \frac{dm_c}{dz} = -\frac{m_w}{\rho_c (1 - X_{\ell\ SAT})^2} \frac{dX_{\ell\ SAT}}{dz} \tag{5.33}$$

Letting $q = Q_e$ as above, we can calculate dq/dz from Equation (5.10) as follows:

$$\frac{\partial}{\partial t}[(1-\phi)\rho_r u_r + \phi\varepsilon\rho_{\ell\ SAT} u_{\ell\ SAT} + \phi(1-\varepsilon)\rho_c u_c] + \frac{dq}{dz} = 0$$

Since the flow is assumed to be steady and using Equations (5.29) and (5.33), this equation becomes:

$$\frac{\partial}{\partial t}[\phi(\rho_c u_c - \rho_r u_r)] + \frac{dq}{dz} = 0$$

$$\Rightarrow \quad \frac{dq}{dz} = (\rho_r u_r - \rho_c u_c)\frac{\partial \phi}{\partial t}$$

$$= \frac{\rho_c u_c - \rho_r u_r}{\rho_c}\frac{dm_c}{dz}$$

Numerical integration is used to determine a new q value.

5.3.5 Saturated gas + solid sodium chloride (Region 3)

Here $Q_{m\ell} = 0$, $X_{g\ sol} \leq X < 1$, $0 < \varepsilon(z,t) \leq 1$, $k_{rg} = 1$, $k_{r\ell} = 0$ and $S_\ell = 0$. Using the same assumptions as for Region 1, we obtain similar equations to those for Region 1 (see above), with subscript $\ell\ SAT$ replaced by $g\ sol$. Similarly, vertical T, p, X, q and deposition rate profiles can be obtained.

5.4 Examples

In this section we implement our correlations for the state space delineations and the thermodynamic properties by using them in two different examples of steady vertical flow through a model geothermal system. The equations that describe such flows were developed in the previous section. As discussed in the Introduction to this chapter, six of the nine regions (see Figure 4.1 and Table 4.1 of Chapter 4) are covered in these examples, so that our correlations for the state space delineations and the thermodynamic properties are tested over much of the state space. This approach is similar to that described in [McKibbin and McNabb, 1995a].

We make no distinction between Regions 2a and 2b, i.e. we revert back to combining them and calling them Region 2 as we do in Chapter 3. Recall from Chapter 4, that splitting Region 2 up into 2a and 2b is merely a device which enables us to match the densities and specific enthalpies of Region 4 (gas phase) and Region 6 (liquid phase) at the region boundaries.

The boundary conditions and parameters required for the examples are:

- an initial (T, p, X) point
- the mass flux of the water (m_w)
- the heat flux (q)
- the formulae or curves (X curves or Corey curves, see [Pruess, 1987] for example) and the residual liquid and gas saturations $(S_{\ell r}, S_{gr})$ which are used to calculate the relative permeabilities $(k_{r\ell}, k_{rg})$
- the permeability (k)
- the thermal conductivity (K)

The two examples are theoretical since they are 1-D, not 3-D, and the boundary conditions and parameters chosen are most likely not typical of real geothermal systems. As discussed in the previous section, some non-physical assumptions have been made in those regions where deposition of salt occurs, i.e. Regions 1 and 3.

5.4.1 Case I

Here

- The initial (T, p, X) = (70 °C, 400 bars, 0.032) at a depth of 0 m (the sea floor). We integrate down to 1000 m.
- $m_w = 1 \times 10^{-7}$ kg/m^2 s
- $q = 1.36$ J/m^2 s
- X curves are used with $S_{\ell r} = 0.30$ and $S_{gr} = 0.10$
- $k = 2 \times 10^{-15}$ m$^2 \approx 2$ millidarcy
- $K = 2$ W/m K

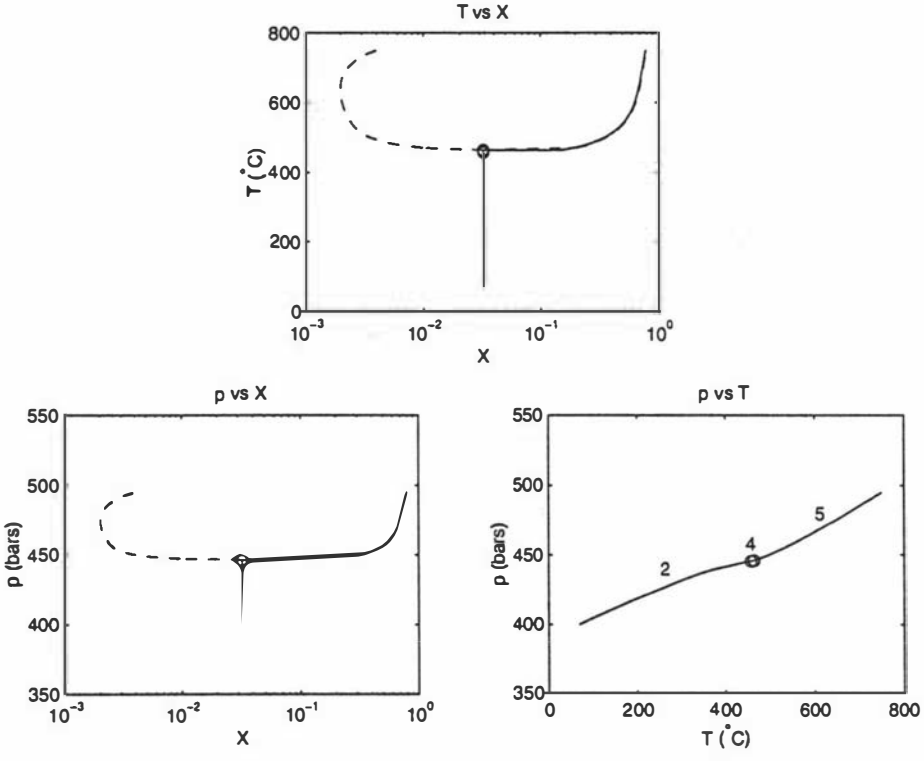

Figure 5.1: 2-D projections of the T-p-X brine state space showing three different perspectives of the state-space trajectory in Case I. The dashed lines represent $X_{\ell s}$ and X_{gs}; the numbers 2, 4 and 5 are the region numbers—see Figure 3.1 and Table 3.1 of Chapter 3.

[McNabb et al., 1993] simulated the flow of brine over a mid-ocean ridge magmatic hot plate and in this example we use similar boundary conditions and parameters to theirs, i.e. the initial state point is on the sea floor where the fluid is assumed to be sea water at $(T, p) = (70\ ^\circ\text{C}, 400\ \text{bars})$ whose salinity is about 3.2 %.

The dashed lines in Figures 5.1 and 5.2 represent $X_{\ell s}$ and X_{gs} of the two-phase region, with the continuous line in Region 5 being the X value obtained from Equation (5.27) of Subsection 5.3.3. This X value lies between $X_{\ell s}$ and X_{gs}, see Table 3.1 of Chapter 3, and we call it the effective X value. Our simulation shows that down to a depth of 600 m, the brine is supercritical (Region 2), but below this depth the fluid is two-phase with the effective X becoming large—see Figure 5.2. This X is close to $X_{\ell s}$ and S_ℓ is about 0.9, so that in this two-phase region we have concentrated brine liquid just on the point of boiling. Another point to note is that co-flow is occuring (as opposed to counter-flow), since both the liquid ($Q_{m\ell}$) and gas (Q_{mg}) mass fluxes are positive (going upwards).

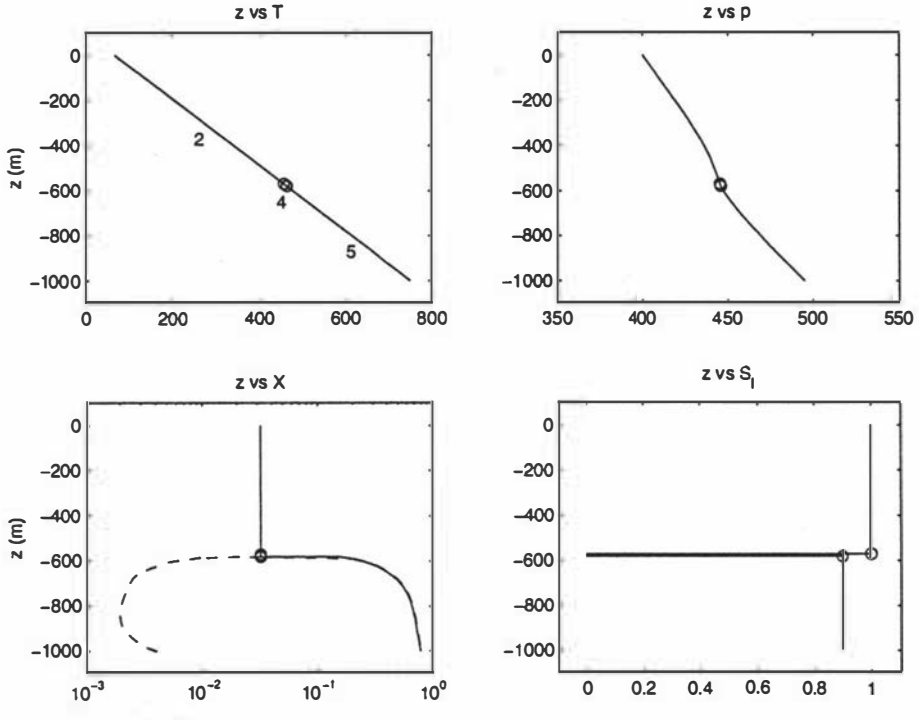

Figure 5.2: T, p, X and S_ℓ (liquid saturation) depth profiles of the fluid flow in Case I. The dashed lines represent $X_{\ell s}$ and X_{gs}; the numbers 2, 4 and 5 are the region numbers—see Figure 3.1 and Table 3.1 of Chapter 3.

Similar to the results of McNabb et al's. 2-D simulation, this case demonstrates that it is possible for a dense brine layer to exist at depth, which may shield the upper parts of the geothermal system from high magmatic temperatures. However in making this claim it needs to be remembered that our model is only 1-D and even though the initial (T, p, X) point is probably quite accurate, the other parameters may not be.

5.4.2 Case II

In this case we have:

- The initial (T, p, X) = (809 °C, 554 bars, 0.030) at a depth of 8000 m or 8 km $\approx$ depth of magma surface. We integrate up to the Earth's surface ($p = 1$ bar).
- $m_w = 1 \times 10^{-7}$ kg/m^2 s
- $q = 0.25$ J/m^2 s
- Corey curves are used with $S_{\ell r} = 0$ and $S_{gr} = 0$
- $k = 2 \times 10^{-15}$ m^2 $\approx$ 2 millidarcy (This value is chosen for mathematical convenience since the nature of permeability at such high temperatures is unknown.)
- $K = 2.5$ W/m K

[Kissling et al., 1996] in one of their simulations of fluid flow through the Wairakei geothermal system had single-phase liquid entering the system at a depth of 2500 m with (T, p) = (260 °C, 250 bars). At the Earth's surface, atmospheric conditions prevailed, i.e. they had (T, p) = (10 °C, 1 bar). They did not specify parameters such as the permeability structure or relative permeability functions for confidentiality reasons.

For this case, we choose T, p and X at 8000 m depth and the other paramaters so that when the fluid reaches depths of 2500 m and 0 m (the surface), the T and p values at these depths approximately equal those given by Kissling et al., see Figure 5.4. Unlike Case I, the fluid here becomes saturated at one stage (Region **3**) and deposition of solid sodium chloride occurs. If the volumetric expansion rate

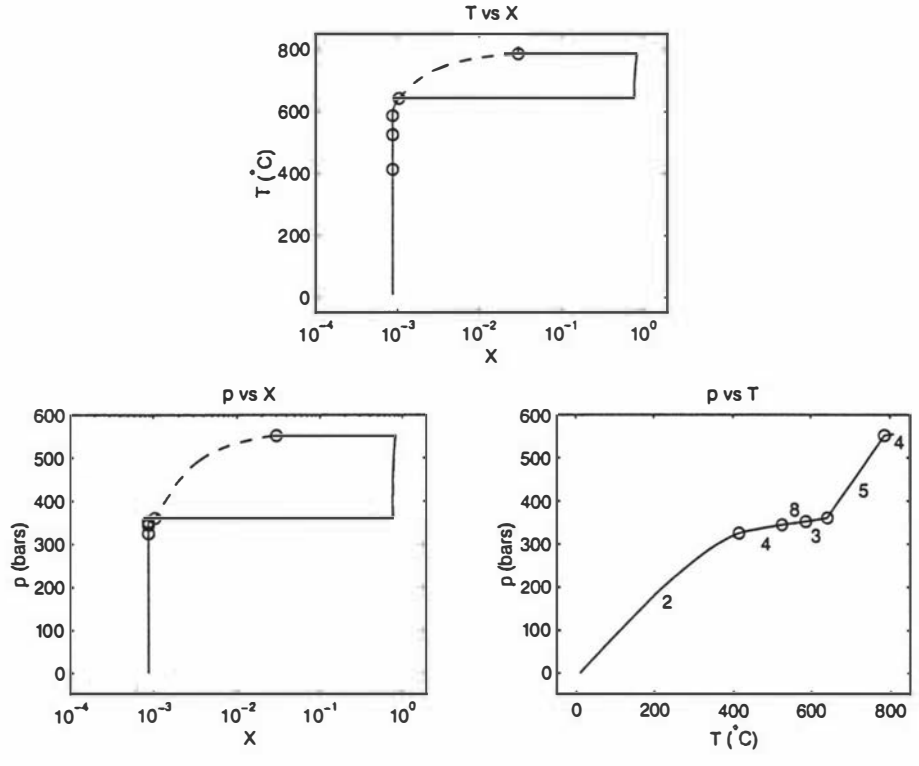

Figure 5.3: 2-D projections of the T-p-X brine state space showing three different perspectives of the state-space trajectory in Case II. The dashed lines represent $X_{\ell s}$ and X_{gs}; the numbers 2, 3, 4, 5 and 8 are the region numbers—see Figure 3.1 and Table 3.1 of Chapter 3.

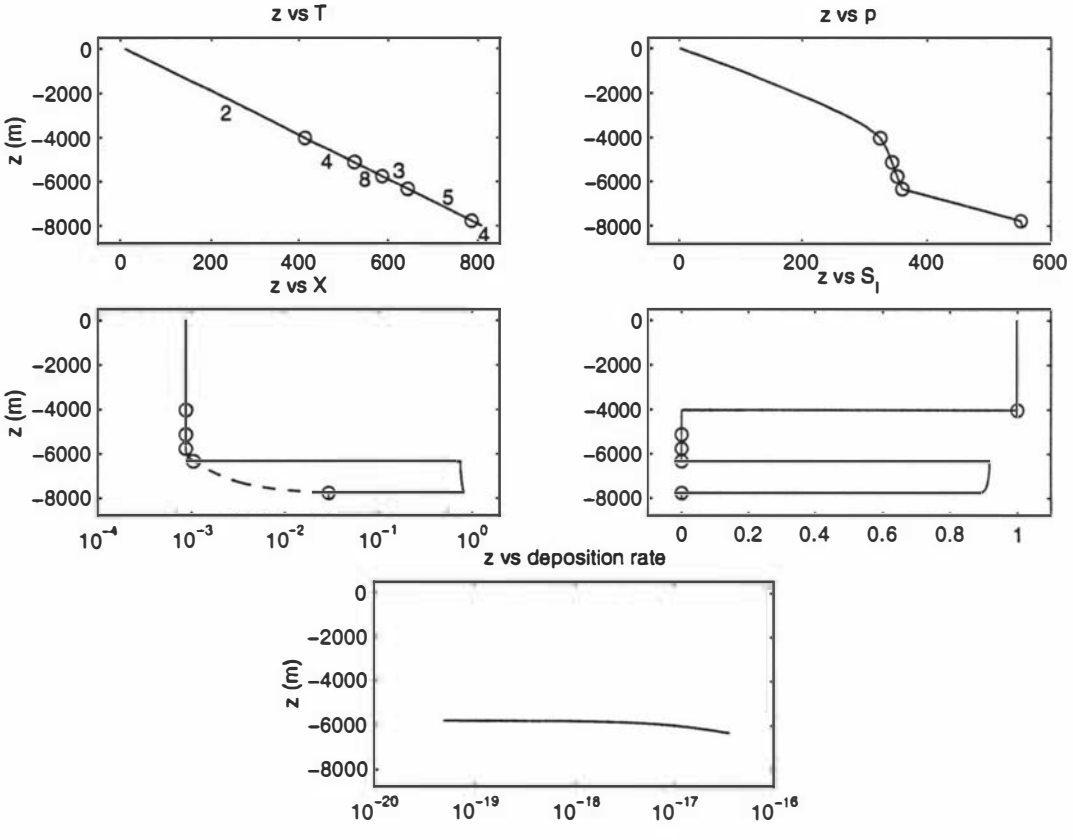

Figure 5.4: T, p, X, S_ℓ and deposition rate depth profiles of the fluid flow in Case II. The dashed lines represent $X_{\ell s}$ and X_{gs}; the numbers 2, 3, 4, 5 and 8 are the region numbers—see Figure 3.1 and Table 3.1 of Chapter 3.

is approximately 1×10^{-18} s^{-1}, a typical value for the sodium chloride deposition rate (see Figure 5.4), then this may be expressed as a rock matrix expansion rate of 0.0031 % per million years.

One possible interpretation of the fluid flow, as illustrated in Figures 5.3 and 5.4, is as follows. At depth magma degasses beneath a dense brine layer which is on the point of boiling (two-phase region where the effective X is close to $X_{\ell s}$ and $S_\ell \approx 0.9$). Co-flow is occuring in this two-phase region. The fluid then becomes saturated and deposits a band of salt leading to the fluid becoming less dense and less concentrated. The brine then becomes a gas and from 4000 m to the surface it is supercritical. Similar to Case I, note the reduction of a relatively high concentration brine at depth to a lower-salinity discharge fluid in the shallower zones, where control is determined by salt deposition and/or two-phase flow regions. As with Case I, it must be stressed that any interpretation must be guarded in the light of the dimensionality of our example and the lack of knowledge regarding the boundary conditions and parameters, especially at these greater depths.

5.5 Summary

This chapter has developed the equations which describe the vertical steady flow of brine through a geothermal system. These equations have been used in two examples in order to demonstrate that our correlations for the state space delineations (see Chapter 3) and the thermodynamic properties (see Chapter 4) work and give plausible results. The results of the examples show how transition between, and trajectories through, the different brine state space regions may be modelled. An attempt has been made at interpreting these results bearing in mind the theoretical nature of our examples and the assumptions made.

Chapter 6

Summary and conclusions

6.1 Summary

Geothermal systems are hot permeable fluid-saturated regions that lie between the magma and the Earth's surface. They can be found all over the world, typically at the boundaries of tectonic plates where the upward heat flux is higher than normal, e.g. Wairakei Geothermal Field in New Zealand and at mid-ocean ridges such as those found off the coast of South America. The upper parts of geothermal systems are called geothermal reservoirs and are able to be reached by drilling; the fluid is extracted and used for such purposes as electricity generation, home heating and recreational bathing. It is commonly believed that for systems like Wairakei, the magma lies about 5–10 km below the Earth's surface. Magmatic temperatures are thought to be 800–1200 °C, i.e. well above the the critical temperature of water (= 374.15 °C). Most of the fluid within a geothermal system is believed to be of meteoric origin, and that groundwater filters down below the Earth's surface by way of faults and fractures in the rocks, is heated and then rises back to the surface as a plume of hot fluid by way of convection.

In order to help predict the long-term behaviour of geothermal reservoirs, models have previously been developed by other researchers and simulations performed with computers. Most of these models have either modelled the geothermal fluid as pure water, H_2O-NaCl (brine) or H_2O-NaCl-CO_2 mixtures. Geothermal fluid is known to consist of water (solvent), a number of solutes (the principal one being NaCl or common salt) and non-condensible gases (carbon dioxide, CO_2, being the

main one). Most researchers used NaCl and CO_2 to represent the combined effects of the solutes and non-condensible gases respectively. The pure-water models extend to supercritical temperatures and pressures (above the critical (T, p) = (374.15 °C, 221.2 bars) of water), whereas most of the previous models for brine (and H_2O-NaCl-CO_2 systems) have been for subcritical temperatures.

A geothermal system is a porous medium consisting of solid rock and pore space through which the fluid and heat may flow. In order to mathematically model the flows through such a system, conservation laws for mass, linear momentum (Darcy's law) and energy are used. Applying these laws results in a set of partial differential equations with derivatives in time and space. In order to solve these equations, knowledge of the thermodynamic properties of density (ρ), specific enthalpy (h) and viscosity (dynamic viscosity, μ, or kinematic viscosity, $\nu = \mu/\rho$) of the model fluid is required.

This thesis models geothermal fluid as H_2O-NaCl. The state or primary variables chosen are T, p and X (the mass fraction of sodium chloride). We have revised the state space description given by [McKibbin and McNabb, 1993] in the light of more recent and comprehensive data sets. This description involves dividing the T-p-X brine state space into eight regions by developing correlations which delineate these regions. Vapour pressure lowering due to salinity is accounted for. These regions correspond to the brine being in different phases which include single-phase liquid, single-phase gas, two-phase (liquid + gas), supercritical (neither liquid nor gas) and regions where saturated brine (liquid or gas) is in equilibrium with solid sodium chloride precipitate. The correlations enable any chosen (T, p, X) value (or state point) to be classified and allocated to one of the eight regions by direct calculation rather than by data table interpolation.

New correlations for ρ, h and μ have been developed and these cover the entire T-p-X brine state space. The thermodynamic properties are determined according to which of the eight regions the state point is in.

Finally, we have tested our correlations for the state space delineations and thermodynamic properties by seeing if plausible results are obtained in the case of steady vertical flow. Some non-physical assumptions were made in those regions where deposition of NaCl occurs, in order to model such flows in these regions. Plausible results have indeed been obtained, although any interpretation of the

results must be cautious, since our model is only 1-D and the boundary conditions and parameters are not well known, especially at depth.

6.2 Conclusions

Our correlations for the state space delineations and the thermodynamic properties do not exactly fit the data for pure H_2O-NaCl systems, but even if they did, they would not necessarily be exactly correct for geothermal fluids, since such fluids are not pure brine. Also the composition of geothermal fluids is not accurately known at depth, so that we cannot possibly hope to exactly model such fluids. Therefore like most researchers in this field, we have represented the combined effects of the solutes by the main solute component, i.e. NaCl.

Some of the published data for the system H_2O-NaCl is inconsistent, and in order to obtain workable correlations that are qualitatively correct, we have used data sets that are self-consistent. Our correlations are simple algebraic formulae in terms of the primary state variables T, p and X. We have successfully used our correlations in computer subroutines that are used in the numerical simulation of steady vertical flows. Since our correlations extend to supercritical temperatures and pressures, deep, hot, high-pressure brines are able to be modelled as well as brines at shallower depths.

Future work involves:

- Testing our correlations on more general cases, e.g. a fully 3-D model in which the flow is not steady and the rock matrix does not expand to accomodate deposition of NaCl. Hence the effective porosity will no longer be constant over time and the permeability will also vary with time (and position).

- Incorporating our subroutines for the state space delineations and thermodynamic properties in the TOUGH2 simulator, in order to extend its temperature range to supercritical.

- Adding CO_2 to our H_2O-NaCl model and developing correlations for the H_2O-NaCl-CO_2 system, which can also be used in numerical simulators.

- Refining the correlations as more experimental data becomes available for the thermodynamic properties (especially h and μ) of brine at supercritical

temperatures.

- Using the correlations to help predict deposition environments that can be matched with fluid inclusion data to guide mineral exploration.

Appendix A

Correlation formulae for the state space delineations

The coefficient values are given in Table A.1.

Three-phase surface [$p_{SAT}(T)$, Figure 3.4, and $X_{g\ SAT}(T)$, Figure 3.5]. $p_{SAT}(T)$ is the boundary between Region 3 and Regions 1 & 5 ($T < 800$ °C). $X_{g\ SAT}(T)$ is where the gas boundary of the two-phase region (Region 5) meets the three-phase surface ($T < 800$ °C).

For $T < 800$ °C,

$$p_{SAT}(T) = a_1 t + a_2 t^2 + a_3 t^3 + a_4 t^4 + a_5 t^5 \quad \text{where } t = (\tfrac{T}{800})^2$$

$$X_{g\ SAT}(T) = 10^{-[b_0 + \frac{b_1}{T-825} + b_2 (T-550)^2]}$$

For $800 \leq T \leq 3127$ °C,

$$p_{SAT}(T) = p_{c\ sat}(T) = c_0 + c_1 exp(c_2 T)$$

which is the saturation curve for sodium chloride

$$X_{g\ SAT}(T) = 1$$

Halite-saturated gas surface [$X_{g\ sol}(T,p)$, Figure 3.7]. Boundary between Regions 3 and 8.

For $T < 800$ °C and $p \leq p_{SAT}(T)$,

$$X_{g\ sol}(T,p) = X_{g\ SAT}(T) \left[\frac{p}{p_{SAT}(T)}\right]^y$$

For $T \leq 350$ °C, $y = 6.5$

For $350 < T < 800$ °C, $y = 6 - \frac{T-400}{100}$

Critical curve [$p_{CRIT}(T)$, Figure 3.8 (a), and $X_{CRIT}(T)$, Figure 3.8 (b)]. Apex of Region 5.

For $T \leq 374.15$ °C,

$$p_{CRIT}(T) = p_{w\ sat}(T)$$

which is the saturation curve for water

$$X_{CRIT}(T) = 0$$

For $374.15 < T \leq 850$ °C,

$$p_{CRIT}(T) = d_{10} + d_{11}T + d_{12}T^2 + d_{13}T^3$$

For $850 < T \leq 3127$ °C,

$$p_{CRIT}(T) = d_{20} + d_{21}T + d_{22}T^2 + d_{23}T^3$$

For $374.15 < T \leq 3127$ °C,

$$X_{CRIT}(T) = e_0 + e_1T + e_2T^2 + e_3T^3$$

Halite-saturated liquid surface [$X_{\ell\ SAT}(T)$ and $X_{\ell\ sol}(T,p)$, Figure 3.10]. $X_{\ell\ SAT}(T)$ is where the liquid boundary of the two-phase region (Region 5) meets the three-phase surface ($T < 800$ °C). $X_{\ell\ sol}(T,p)$ is the boundary between Region 1 and Regions 2 & 6 ($T < 800$ °C).

For $T < 800$ °C,

$$X_{\ell\ SAT}(T) = X_{\ell\ sol}(T,p) = f_0 + f_1 T + f_2 T^2 + f_3 T^3$$

For $800 \leq T \leq 3127$ °C,

$$X_{\ell\ SAT}(T) = X_{\ell\ sol}(T,p) = 1$$

Two-phase region, liquid boundary [$X_{\ell s}(T,p)$, Figures 3.11 and 3.12]. Region 5.

For $p_{SAT}(T) < p < p_{CRIT}(T)$, $374.15 < T \leq 3127$ °C,

$$X_{\ell s}(T,p) = X_{CRIT}(T) \left\{ \frac{X_{\ell\ SAT}(T)}{X_{CRIT}(T)} \right\}^{\left[\frac{p_{CRIT}(T)-p}{p_{CRIT}(T)-p_{SAT}(T)}\right]^z}$$

where $z = b\left\{1 - \frac{1.4 log_{10}[X_{CRIT}(T)]}{1+80a} + 6a\right\}^{-1}$ and $a = (\frac{T}{800})^2 - (\frac{374.15}{800})^2$

For $374.15 < T \leq 900$ °C, $b = g_0 + g_1 T$

For $900 < T \leq 3127$ °C, $b = 2.5$

For $T \leq 374.15$ °C, $X_{CRIT}(T) = 0$ and $p_{CRIT}(T) = p_{w\ sat}(T)$, the above becomes

$$X_{\ell s}(T,p) = X_{\ell\ SAT}(T) \left[\frac{p_{w\ sat}(T) - p}{p_{w\ sat}(T) - p_{SAT}(T)} \right]^z$$

where $z = 0.5 \ln(10)/1.4$

Table A.1: Coefficient values for the correlation formulae for the state space delineations.

i	0	1	2	3	4	5
a_i		1.32729e1	3.18909e3	-7.24296e2	-8.15640e3	5.67834e3
b_i	3.44340e0	1.47519e2	3.93180e-5			
c_i	-1.10476e-1	6.87956e-3	3.47030e-3			
d_{1i}	2.56326e2	-3.28926e0	1.05024e-2	-5.24390e-6		
d_{2i}	-3.28254e3	9.20086e0	-4.19191e-3	5.18556e-7		
e_i	-4.28737e-1	1.38295e-3	-6.79448e-7	1.22578e-10		
f_i	2.63500e-1	7.48368e-6	1.44611e-6	-3.80860e-10		
g_i	-9.23029e-1	3.80337e-3				
h_i	-1.20121e0	5.72558e-3	-3.15039e-6			

Two-phase region, gas boundary [$X_{gs}(T,p)$, Figures 3.11 and 3.12]. Region 5.

For $p_{SAT}(T) < p < p_{CRIT}(T)$, $374.15 < T \leq 3127$ °C,

$$X_{gs}(T,p) = dX_{CRIT}(T)\left\{\frac{X_{g\ SAT}(T)}{X_{CRIT}(T)}\right\}^{\left[\frac{p_{CRIT}(T)-p}{p_{CRIT}(T)-p_{SAT}(T)}\right]^z}$$

where

$$d = 10^{\left\{\left[\frac{p_{CRIT}(T)-p}{p_{CRIT}(T)-p_{SAT}(T)}\right]^{1.5}-\left[\frac{p_{CRIT}(T)-p}{p_{CRIT}(T)-p_{SAT}(T)}\right]^{0.5}\right\}}$$

For $374.15 < T \leq 900$ °C, $z = h_0 + h_1 T + h_2 T^2$

For $900 < T \leq 3127$ °C, $z = 1.4$

For $T \leq 374.15$ °C, $X_{CRIT}(T) = 0$ and $p_{CRIT}(T) = p_{w\ sat}(T)$, the above becomes

$$X_{gs}(T,p) = X_{g\ SAT}(T)\left[\frac{p_{w\ sat}(T) - p}{p_{w\ sat}(T) - p_{SAT}(T)}\right]^z$$

where $z = 0.5\ln(10)/1.4$

Appendix B

Correlation formulae for the thermodynamic properties

The coefficient values are given in Table B.1.

B.1 Density

Saturated liquid and gas densities for sodium chloride, Figure 4.5. Densities on the right-hand boundaries ($X = 1$) of Regions 2, 6 and 7, see Figure 3.1 (c).

For $800 \leq T \leq 3127$ °C,

$$\rho_{\ell\ SAT}(T) = \rho_{c\ell\ sat}(T) = a_0 + a_1 T + a_2 T^2 + a_3 T^3 + a_4 T^4$$

$$\rho_{g\ SAT}(T) = \rho_{cg\ sat}(T) = b_0 + b_1 T + b_2 T^2 + b_3 T^3 + b_4 T^4$$

Saturated liquid and gas densities for brine, Figure 4.6. Densities at $X_{\ell\ SAT}(T)$ and $X_{g\ SAT}(T)$—where the liquid and gas boundaries respectively of the two-phase region (Region 5) meet the three-phase surface ($p_{SAT}(T)$).

For $T < 800$ °C,

$$\rho_{\ell\ SAT}(T) = c_0 + c_1 t + c_2 t^2 + c_3 t^3 + c_4 t^4 + c_5 t^5 + c_6 t^6$$

$$\rho_{g\ SAT}(T) = d_1 t^2 + d_2 t^4 + d_3 t^6 + d_4 t^8 + d_5 t^{10}$$

where $t = \frac{T}{800}$

Critical density. Density at $p_{CRIT}(T)$, $X_{CRIT}(T)$ which give the critical curve that runs along the apex of Region 5.

For $T \leq 374.15$ °C, Figure 4.8,

$$\rho_{CRIT}(T) = \begin{cases} \rho_{wg\ sat}(T) \\ \rho_{w\ell\ sat}(T) \end{cases}$$

the saturated gas and liquid densities of water

For $374.15 < T \leq 3127$ °C, Figure 4.7,

$$\rho_{CRIT}(T) = e_0 + e_1 T^{0.1} + e_2 T^2 + \frac{e_3}{T - 320}$$

Two-phase region, density on liquid surface. Density at $X_{\ell s}(T, p)$, the liquid boundary of Region 5 (two-phase region).

For $T \leq 374.15$ °C, Figure 4.10,

$$\rho_{\ell s}(T,p) = \rho_{w\ell\ sat}(T) + [\rho_{\ell\ SAT}(T) - \rho_{w\ell\ sat}(T)] \left[\frac{p_{w\ sat}(T) - p}{p_{w\ sat}(T) - p_{SAT}(T)}\right]^{\frac{1}{2.2}}$$

For $374.15 < T \leq 3127$ °C, Figure 4.11,

$$\rho_{\ell s}(T,p) = \rho_{CRIT}(T) + [\rho_{\ell\ SAT}(T) - \rho_{CRIT}(T)] \left[\frac{p_{CRIT}(T) - p}{p_{CRIT}(T) - p_{SAT}(T)}\right]^{\frac{1}{z}}$$

For $374.15 < T \leq 850$ °C, $z = f_0 + f_1 T + f_2 T^2$

For $850 < T \leq 3127$ °C, $z = 1.6$

Two-phase region, density on gas surface. Density at $X_{gs}(T,p)$, the gas boundary of Region 5 (two-phase region).

For $T \leq 374.15$ °C, Figure 4.10,

$$\rho_{gs}(T,p) = \rho_{wg\ sat}(T) + [\rho_{g\ SAT}(T) - \rho_{wg\ sat}(T)] \left[\frac{p_{w\ sat}(T) - p}{p_{w\ sat}(T) - p_{SAT}(T)}\right]^{\frac{1}{z}}$$

where $z = g_{10} + g_{11}T + \frac{g_{12}}{T-380}$

For $374.15 < T \leq 3127$ °C, Figure 4.11,

$$\rho_{gs}(T,p) = \rho_{CRIT}(T) + [\rho_{g\ SAT}(T) - \rho_{CRIT}(T)] \left[\frac{p_{CRIT}(T) - p}{p_{CRIT}(T) - p_{SAT}(T)}\right]^{\frac{1}{z}}$$

For $374.15 < T \leq 850$ °C, $z = g_{20} + g_{21}T$

For $850 < T \leq 3127$ °C, $z = 1.9$

B.2 Specific enthalpy

Saturated liquid and gas enthalpies for sodium chloride, Figure 4.28. Enthalpies on the right-hand boundaries ($X = 1$) of Regions 2, 6 and 7, see Figure 3.1 (c).

For $800 \leq T \leq 3127$ °C,

$$h_{\ell\ SAT}(T) = h_{c\ell\ sat}(T) = j_0 + j_1 T$$

$$h_{g\ SAT}(T) = h_{cg\ sat}(T) = \begin{cases} k_{10} + k_{11} T, & T \leq 1465\ ^\circ\text{C} \\ k_{20} + k_{21} T, & T > 1465\ ^\circ\text{C} \end{cases}$$

Saturated liquid and gas enthalpies for brine, Figure 4.28. Enthalpies at $X_{\ell\ SAT}(T)$ and $X_{g\ SAT}(T)$—where the liquid and gas boundaries respectively of the two-phase region (Region 5) meet the three-phase surface ($p_{SAT}(T)$).

For $T < 800$ °C,

$$h_{\ell\ SAT}(T) = m_0 + m_1 T + m_2 T^2 + m_3 T^3$$

$$h_{g\ SAT}(T) = n_0 + n_1 T + n_2 T^2 + n_3 T^3$$

Critical enthalpy, Figure 4.28. Enthalpy at $p_{CRIT}(T)$, $X_{CRIT}(T)$ which give the critical curve that runs along the apex of Region 5.

For $T \leq 374.15$ °C,

$$h_{CRIT}(T) = \begin{cases} h_{wg\ sat}(T) \\ h_{w\ell\ sat}(T) \end{cases}$$

the saturated gas and liquid enthalpies of water

For $374.15 < T \leq 3127$ °C,

$$h_{CRIT}(T) = \begin{cases} q_{10} + q_{11}T + q_{12}T^2, & T \leq 600\ ^\circ\text{C} \\ q_{20} + q_{21}T, & T > 600\ ^\circ\text{C} \end{cases}$$

Two-phase region, enthalpy on liquid surface, Figure 4.29. Enthalpy at $X_{\ell s}(T,p)$, the liquid boundary of Region 5 (two-phase region).

For $T \leq 374.15$ °C,

$$h_{\ell s}(T,p) = h_{w\ell\ sat}(T) + [h_{\ell\ SAT}(T) - h_{w\ell\ sat}(T)] \left[\frac{p_{w\ sat}(T) - p}{p_{w\ sat}(T) - p_{SAT}(T)}\right]^{\frac{1}{1.4}}$$

For $374.15 < T \leq 3127$ °C,

$$h_{\ell s}(T,p) = h_{CRIT}(T) + [h_{\ell\ SAT}(T) - h_{CRIT}(T)] \left[\frac{p_{CRIT}(T) - p}{p_{CRIT}(T) - p_{SAT}(T)}\right]^{\frac{1}{z}}$$

For $374.15 < T \leq 550$ °C, $z = r_0 + r_1 T$

For $550 < T \leq 3127$ °C, $z = 3$

Two-phase region, enthalpy on gas surface, Figure 4.29. Enthalpy at $X_{gs}(T,p)$, the gas boundary of Region 5 (two-phase region).

For $T \leq 374.15$ °C,

$$h_{gs}(T,p) = h_{wg\ sat}(T) + [h_{g\ SAT}(T) - h_{wg\ sat}(T)] \left[\frac{p_{w\ sat}(T) - p}{p_{w\ sat}(T) - p_{SAT}(T)}\right]^{\frac{1}{1.7}}$$

For $374.15 < T \leq 3127$ °C,

$$h_{gs}(T,p) = h_{CRIT}(T) + [h_{g\ SAT}(T) - h_{CRIT}(T)] \left[\frac{p_{CRIT}(T) - p}{p_{CRIT}(T) - p_{SAT}(T)}\right]^{\frac{1}{z}}$$

For $374.15 < T \leq 550$ °C, $z = s_0 + s_1 T$

For $550 < T \leq 3127$ °C, $z = 3$

B.3 Dynamic viscosity

Viscosity for liquid sodium chloride. Viscosity on the right-hand boundaries ($X = 1$) of Regions 2, 6 and 7, see Figure 3.1 (c).

For $800 \leq T < 1000$ °C, Figure 4.34,

$$\mu_c(T) = u_0 + u_1 T$$

For $T \geq 1000$ °C,

$$\mu_c(T = 1000) = u_0 + u_1 1000$$

Viscosity for brine. Viscosity for all regions.

For $T < 800$ °C, Figure 4.36,

$$\begin{aligned} \mu_b(T,p,X) &= \left\{ \mu_w(T,p)\,(1+3X) \left(\frac{800-T}{800}\right)^9 + \right. \\ &\quad \left. \left(\frac{T}{800}\right)^9 [\mu_w(T,p)(1-X) + \mu_c(800)X] \right\} \\ &\quad / \left\{ \left(\frac{800-T}{800}\right)^9 + \left(\frac{T}{800}\right)^9 \right\} \end{aligned}$$

For $T \geq 800$ °C,

$$\mu_b(T,p,X) = \mu_w(T,p)(1-X) + \mu_c(T)X$$

Table B.1: Coefficient values for the correlation formulae for the thermodynamic properties.

i	0	1	2	3	4	5	6
a_i	1.74412e3	1.14967e-1	-6.21000e-4	2.71397e-7	-4.29832e-11		
b_i	2.29444e1	-1.02287e-1	1.54158e-4	-9.19469e-8	1.90449e-11		
c_i	1.22004e3	-6.09462e2	3.17390e3	-1.75541e4	4.08000e4	-3.73488e4	1.18784e4
d_i		4.54453e0	1.75270e3	-2.47078e3	5.56320e1	6.58004e2	
e_i	-1.35369e3	1.09119e3	-8.80332e-5	-1.58302e4			
f_i	3.33107e0	-3.79871e-3	2.07312e-6				
g_{1i}	7.87001e-1	1.02499e-3	-1.36276e1				
g_{2i}	4.75804e0	-3.36240e-3					
j_i	2.66797e2	1.22736e0					
k_{1i}	3.29122e3	1.15807e0					
k_{2i}	5.77035e3	-5.34171e-1					
m_i	0.00000e0	3.57384e0	-3.79475e-3	1.59816e-6			
n_i	2.50000e3	2.85416e0	-7.99981e-3	8.89497e-6			
q_{1i}	2.72369e3	-2.94154e0	3.29231e-3				
q_{2i}	1.67958e3	7.74040e-1					
r_i	-2.00426e0	9.09866e-3					
s_i	-1.06597e0	7.39266e-3					
u_i	4.71624e-3	-4.02030e-6					

Appendix C

Equations for the thermodynamic properties for the regions

C.1 Region 1

Density

$$\rho_b = \rho_{\ell\ SAT}(T)$$

Specific enthalpy

$$h_b = h_{\ell\ SAT}(T)$$

Dynamic viscosity

$$\begin{aligned} \mu_b \;=\; & \left\{ \mu_w(T,p)\,(1+3X)\left(\frac{800-T}{800}\right)^9 + \right. \\ & \left. \left(\frac{T}{800}\right)^9 \left[\mu_w(T,p)(1-X) + \mu_c(800)X\right] \right\} \\ & \Big/ \left\{ \left(\frac{800-T}{800}\right)^9 + \left(\frac{T}{800}\right)^9 \right\} \end{aligned} \tag{C.1}$$

C.2 Regions 2b and 6

Density

$$\rho_{1000}(T,X) = \rho_w(T,p=1000) + X[1695 - \rho_w(T,p=1000)]$$

For $\rho_{1000} \leq \rho_{\ell s}$:

$$\rho_b = \rho_{\ell s}(T,p) \tag{C.2}$$

For $\rho_{1000} > \rho_{\ell s}$:

For $p_{\ell s} \leq 500$ bars and $p \leq 1000$ bars:

$$\begin{aligned}\rho_b &= \rho_{\ell s}(T, p_{\ell s}(T,X)) \\ &\quad + \frac{p - p_{\ell s}(T,X)}{1000 - p_{\ell s}(T,X)}[\rho_{1000}(T,X) - \rho_{\ell s}(T,p_{\ell s}(T,X))]\end{aligned} \tag{C.3}$$

For $p_{\ell s} \leq 500$ bars and $p > 1000$ bars:

$$\rho_b = \rho_{1000}(T,X) \tag{C.4}$$

For $p > 500$ bars and $p \leq p_{\ell s} + 500$ bars:

$$\begin{aligned}\rho_b &= \rho_{\ell s}(T, p_{\ell s}(T,X)) \\ &\quad + \frac{p - p_{\ell s}(T,X)}{500}[\rho_{1000}(T,X) - \rho_{\ell s}(T,p_{\ell s}(T,X))]\end{aligned} \tag{C.5}$$

For $p > 500$ bars and $p > p_{\ell s} + 500$ bars:

$$\rho_b = \rho_{1000}(T,X) \tag{C.6}$$

Specific enthalpy

$$h_b = h_{\ell s}(T,p)$$

Dynamic viscosity

For $T < 800$ °C, see Equation (C.1), with $p = p_{CRIT}(T)$ for Region 6.

For $T \geq 800$ °C,

$$\mu_b(T,p,X) = \mu_w(T,p)(1-X) + \mu_c(T)X \tag{C.7}$$

$p = p_{CRIT}(T)$ for Region 6.

C.3 Region 2a

Density

$$\rho_b = \rho_w(T,p) + \frac{X}{X_{CRIT}(T)}[\rho_{2b}(T,p,X_{CRIT}(T)) - \rho_w(T,p)]$$

where $\rho_{2b}(T,p,X_{CRIT}(T))$ is given by Equations (C.2) - (C.6), with $p_{\ell s}(T,X) = p_{CRIT}(T)$, $\rho_{\ell s}(T,p) = \rho_{\ell s}(T,p_{\ell s}(T,X)) = \rho_{CRIT}(T)$ and $\rho_{1000}(T,X) = \rho_{1000}(T,X_{CRIT}(T))$.

Specific enthalpy

$$h_b = h_w(T,p) + \frac{X}{X_{CRIT}(T)}[h_{CRIT}(T) - h_w(T,p)]$$

Dynamic viscosity

See Equations (C.1) and (C.7).

C.4 Region 3

Density

$$\rho_b = \rho_{g\ SAT}(T)\frac{p}{p_{SAT}(T)}$$

Specific enthalpy

$$h_b = h_{g\ SAT}(T)\frac{p}{p_{SAT}(T)}$$

Dynamic viscosity

See Equation (C.1).

C.5 Region 4

Density

$$\rho_b = \rho_w(T,p) + \frac{X}{X_{gs}(T,p)}[\rho_{gs}(T,p) - \rho_w(T,p)]$$

Specific enthalpy

$$h_b = h_w(T,p) + \frac{X}{X_{gs}(T,p)}[h_{gs}(T,p) - h_w(T,p)]$$

Dynamic viscosity

See Equations (C.1) and (C.7).

C.6 Region 5

Density

$$\rho_b = (1 - S_\ell)\rho_{gs}(T,p) + S_\ell\rho_{\ell s}(T,p) \tag{C.8}$$

Specific enthalpy

$$h_b = \frac{(1 - S_\ell)\rho_{gs}(T,p)h_{gs}(T,p) + S_\ell\rho_{\ell s}(T,p)h_{\ell s}(T,p)}{\rho_b}$$

where ρ_b is calculated from Equation (C.8).

Dynamic viscosity

See Equations (C.1) and (C.7).

C.7 Region 7

Density

$$\rho_b = \rho_w(T,p) + X[\rho_{g\ sol}(T,p) - \rho_w(T,p)]$$

Specific enthalpy

$$h_b = h_w(T,p) + X[h_{g\ sol}(T,p) - h_w(T,p)]$$

Dynamic viscosity

See Equation (C.7).

C.8 Region 8

Density

$$\rho_b = \rho_w(T,p) + \frac{X}{X_{g\ sol}(T,p)}[\rho_{g\ sol}(T,p) - \rho_w(T,p)]$$

Specific enthalpy

$$h_b = h_w(T,p) + \frac{X}{X_{g\ sol}(T,p)}[h_{g\ sol}(T,p) - h_w(T,p)]$$

Dynamic viscosity

See Equation (C.1).

Bibliography

[Alkan et al., 1995] Alkan, H., Babadagli, T., and Satman, A. (1995). The prediction of the PVT/phase behaviour of the geothermal fluid mixtures. In *Proc. World Geothermal Congress*, pages 1659–1665. International Geothermal Association.

[Anderko and Pitzer, 1992] Anderko, A. and Pitzer, K. S. (1992). Equation of state for pure sodium chloride. *Fluid Phase Equilibria*, 79:103–112.

[Anderko and Pitzer, 1993] Anderko, A. and Pitzer, K. S. (1993). Equation of state representation of phase equilibria and volumetric properties of the system NaCl-H_2O above 573 K. *Geochimica et Cosmochimica Acta*, 57:1657–1680.

[Andersen et al., 1992] Andersen, G., Probst, A., Murray, L., and Butler, S. (1992). An accurate PVT model for geothermal fluids as represented by H_2O-CO_2-NaCl mixtures. In *Proc. 17th Workshop on Geothermal Reservoir Engineering*, pages 239–248. Stanford University.

[Arnold, 1970] Arnold, E. (1970). UK Steam Tables in SI Units. Edward Arnold Ltd., London.

[Barton and Bloom, 1956] Barton, J. L. and Bloom, H. (1956). A boiling point method for determination of vapor pressures of molten salts. *J. Phys. Chem.*, 60:1413–1416.

[Battistelli, 1998] Battistelli, A. (1998). Private communication.

[Battistelli et al., 1993] Battistelli, A., Calore, C., and Pruess, K. (1993). A fluid property module for the TOUGH2 simulator for saline brines with non-condensible gas. In *Proc. 18th Workshop on Geothermal Reservoir Engineering*, pages 249–259. Stanford University.

[Battistelli et al., 1995] Battistelli, A., Calore, C., and Pruess, K. (1995). Vapor pressure lowering effects due to salinity and suction pressure in the depletion of vapor-dominated geothermal reservoirs. In *Proc. TOUGH Workshop '95, Lawrence Berkeley Laboratory Report LBL-37200*, pages 77–83.

[Battistelli et al., 1997] Battistelli, A., Calore, C., and Pruess, K. (1997). The simulator TOUGH2/EWASG for modelling geothermal reservoirs with brines and non-condensible gas. *Geothermics*, 26(4):437–464.

[Bear and Bachmat, 1991] Bear, J. and Bachmat, Y. (1991). *Introduction to modeling of transport phenomena in porous media*, volume 4. Kluwer Academic Publishers, Holland.

[Bear and Verruijt, 1994] Bear, J. and Verruijt, A. (1994). *Modeling groundwater flow and pollution.* D. Reidel Publishing Company, Holland.

[Bischoff, 1991] Bischoff, J. L. (1991). Densities of liquids and vapors in boiling NaCl-H_2O solutions: a PVTX summary from 300 ° to 500 °C. *American Journal of Science*, 291:309–338.

[Bischoff and Pitzer, 1989] Bischoff, J. L. and Pitzer, K. S. (1989). Liquid-vapor relations for the system NaCl-H_2O: Summary of the P-T-x surface from 300 °C to 500 °C. *American Journal of Science*, 289:217–248.

[Bodnar, 1994] Bodnar, R. J. (1994). Synthetic fluid inclusions: XII. The system H_2O-NaCl. Experimental determination of the halite liquidus and isochores for a 40 wt % NaCl solution. *Geochimica et Cosmochimica Acta*, 58(3):1053–1063.

[Bodnar et al., 1985] Bodnar, R. J., Burnham, C. W., and Sterner, S. M. (1985). Synthetic fluid inclusions in natural quartz. III. Determination of phase equilibrium properties in the system H_2O-NaCl to 1000 °C and 1500 bars. *Geochimica et Cosmochimica Acta*, 49:1861–1873.

[Bowers and Helgeson, 1983] Bowers, T. S. and Helgeson, H. C. (1983). Calculation of the thermodynamic and geochemical consequences of nonideal mixing in the system H_2O-CO_2-NaCl on phase relations in geologic systems: Equation of state for H_2O-CO_2-NaCl fluids at high pressures and temperatures. *Geochimica et Cosmochimica Acta*, 47:1247–1275.

[Cathles, 1977] Cathles, L. M. (1977). An analysis of the cooling of intrusives by ground-water convection which includes boiling. *Economic Geology*, 72:804–826.

[Chierici et al., 1981] Chierici, G. L., Giannone, G., Sclocchi, G., and Terzi, L. (1981). A wellbore model for two-phase flow in geothermal reservoirs. 56th Soc. of Petr. Eng. Annual Fall Tech. Conf. San Antonio, Texas.

[Chou, 1987] Chou, I.-M. (1987). Phase relations in the system NaCl-KCl-H_2O. III: Solubilities of halite in vapor-saturated liquids above 445 °C and redetermination of phase equilibrium properties in the system NaCl-H_2O to 1000 °C and 1500 bars. *Geochimica et Cosmochimica Acta*, 51:1965–1975.

[Datz et al., 1961] Datz, S., Smith, W. T., and Taylor, E. H. (1961). *J. Chem. Phys.*, 34:558.

[Ellis and Golding, 1963] Ellis, A. J. and Golding, R. M. (1963). The solubility of carbon dioxide above 100 °C in water and in sodium chloride solutions. *American Journal of Science*, 261:47–60.

[Ershaghi et al., 1983] Ershaghi, I., Abdassah, D., Bonakdar, M., and Ahmad, S. (1983). Estimation of geothermal brine viscosity. *Journal of Petroleum Technology*, pages 621–628.

[Faust and Mercer, 1981] Faust, C. R. and Mercer, J. W. (1981). GEOTHER: A finite difference model of three dimensional, single and two phase heat transport in a porous medium. Technical report, Geotrans. Inc.

[Gunter et al., 1983] Gunter, W. D., Chou, I.-M., and Girsperger, S. (1983). Phase relations in the system NaCl-KCl-H_2O II: Differential thermal analysis of the halite liquidus in the NaCl-H_2O binary above 450 °C. *Geochimica et Cosmochimica Acta*, 47:863–873.

[Haas, 1976] Haas, J. L. (1976). Physical properties of the coexisting phases and thermochemical properties of the H_2O component in boiling NaCl solutions: 1421-A. United States Government Printing Office, Washington, D.C. 20402.

[Haas and Potter, 1977] Haas, J. L. and Potter, R. W. (1977). The measurement and evaluation of PVTX properties of geothermal brines and the derived thermodynamic properties. In *Proc. Symp. Thermophys. Prop.*, pages 604–614.

[Hanano and Seth, 1995] Hanano, M. and Seth, M. S. (1995). Numerical modeling of hydrothermal convection systems including super-critical fluid. In *Proc. World Geothermal Congress*, pages 1681–1686. International Geothermal Association.

[Hayba and Ingebritsen, 1994] Hayba, D. O. and Ingebritsen, S. E. (1994). The computer model HYDROTHERM, a three-dimensional finite-difference model to simulate ground-water flow and heat transport in the temperature range of 0 to 1,200 °C. Water-Resources Investigations Report 94-4045, U.S. Geological Survey, Reston, Virginia.

[Hayba and Ingebritsen, 1997] Hayba, D. O. and Ingebritsen, S. E. (1997). Multiphase groundwater flow near cooling plutons. *Journal of Geophysical Research*, 102(B6):12,235–12,252.

[Henley and McNabb, 1978] Henley, R. W. and McNabb, A. (1978). Magmatic vapor plumes and ground-water interaction in porphyry copper emplacement. *Economic Geology*, 73(1):1–20.

[Herbert et al., 1988] Herbert, A. W., Jackson, C. P., and Lever, D. A. (1988). Coupled Groundwater Flow and Solute Transport With Fluid Density Strongly Dependent Upon Concentration. *Water Resources Research*, 24(10):1781–1795.

[James and Lord, 1992] James, A. M. and Lord, M. P. (1992). *MacMillan's Chemical and Physical Data*. The MacMillan Press Ltd., London.

[Janz, 1988] Janz, G. J. (1988). Thermodynamic and transport properties of molten salts: Correlation equations for critically evaluated density, surface tension, electrical conductance, and viscosity data. *Journal of Physical and Chemical Reference Data*, 17(2).

[Kaufmann, 1968] Kaufmann, D. W., editor (1968). *Sodium Chloride the production and properties of salt and brine*, chapter 25. American Chemical Society Monograph Series. Hafner Publishing Company, New York.

[Kirshenbaum et al., 1962] Kirshenbaum, A. D., Cahill, J. A., McGonigal, P. J., and Grosse, A. V. (1962). The density of liquid NaCl and KCl and an estimate of their critical constants together with those of the alkali halides. *Journal of Inorg. Nucl. Chem.*, 24:1287–1296.

[Kissling, 1995] Kissling, W. M. (1995). Extending MULKOM to super-critical temperatures and pressures. In *Proc. World Geothermal Congress*, pages 1687–1690. International Geothermal Association.

[Kissling, 1996] Kissling, W. M. (1996). Large scale numerical models of TVZ-type geothermal fields. In *Proc. 18th New Zealand Geothermal Workshop*, pages 275–280. University of Auckland.

[Kissling et al., 1996] Kissling, W. M., Brown, K. L., O'Sullivan, M. J., White, S. P., and Bullivant, D. P. (1996). Modelling chloride and CO_2 chemistry in the Wairakei geothermal reservoir. *Geothermics*, 25(3):285–305.

[Knight and Bodnar, 1989] Knight, C. L. and Bodnar, R. J. (1989). Synthetic fluid inclusions: IX. Critical properties of NaCl-H_2O solutions. *Geochimica et Cosmochimica Acta*, 53:3–8.

[Lichti and Sanada, 1997] Lichti, K. A. and Sanada, N. (1997). Materials issues for utilisation of deep geothermal systems. In *Proc. 19th New Zealand Geothermal Workshop*, pages 169–174. University of Auckland.

[Lide, 1996] Lide, D. R., editor (1996). *CRC Handbook of Chemistry and Physics*, pages 8–73. CRC Press, 77th edition.

[McKibbin and McNabb, 1993] McKibbin, R. and McNabb, A. (1993). Modelling the phase boundaries and fluid properties of the system H_2O-NaCl at high temperatures and pressures. In *Proc. 15th New Zealand Geothermal Workshop*, pages 267–273. University of Auckland.

[McKibbin and McNabb, 1995a] McKibbin, R. and McNabb, A. (1995a). From magma to groundwater: the brine connection. In *Proc. World Geothermal Congress*, pages 1125–1130. International Geothermal Association.

[McKibbin and McNabb, 1995b] McKibbin, R. and McNabb, A. (1995b). Mathematical modelling of non-condensible gases in hot dense brines: the system H_2O-NaCl-CO_2. In *Proc. 17th New Zealand Geothermal Workshop*, pages 255–262. University of Auckland.

[McKibbin and McNabb, 1998] McKibbin, R. and McNabb, A. (1998). Deep hydrothermal systems: Mathematical modelling of hot dense brines containing non-condensible gases. To be published in *Journal of Porous Media*.

[McNabb, 1992] McNabb, A. (1992). The Taupo-Rotorua hot-plate. In *Proc. 14th New Zealand Geothermal Workshop*, pages 111–114. University of Auckland.

[McNabb et al., 1993] McNabb, A., White, S., and McKibbin, R. (1993). Brine circulation and hot-plate formation. In *Proc. 15th New Zealand Geothermal Workshop*, pages 275–277. University of Auckland.

[Michaelides, 1981] Michaelides, E. E. (1981). Thermodynamic properties of geothermal fluids. *Geothermal Resources Council Transactions*, 5:361–364.

[Norton and Knight, 1977] Norton, D. and Knight, J. (1977). Transport phenomena in hydrothermal systems: cooling plutons. *American Journal of Science*, 277:937–981.

[Oldenburg et al., 1995] Oldenburg, C., Pruess, K., and Lippmann, M. (1995). Heat and mass transfer in hypersaline geothermal systems. In *Proc. World Geothermal Congress*, pages 1647–1652. International Geothermal Association.

[O'Sullivan and McKibbin, 1989] O'Sullivan, M. J. and McKibbin, R. (1989). *Geothermal Reservoir Engineering.* University of Auckland.

[Phillips et al., 1981] Phillips, S. L., Igbene, A., Fair, J. A., Ozbek, H., and Tavana, M. (1981). A technical databook for geothermal energy utilization. Lawrence Berkeley Laboratory, University of California, Berkeley, CA 94720.

[Pitzer, 1995] Pitzer, K. S. (1995). Ionic fluids: Near-critical and related properties. *J. Phys. Chem.*, 99(35):13070–13077.

[Pitzer, 1996] Pitzer, K. S. (1996). Sodium chloride vapor at very high temperatures: Linear polymers are important. *J. Chem. Phys.*, 104(17):6724–6729.

[Pitzer, 1997] Pitzer, K. S. (1997). Private communication.

[Pitzer and Jiang, 1996] Pitzer, K. S. and Jiang, S. (1996). Equation of state for NaCl-H_2O: comparison with mineral dehydration equilibria. *Contrib. Mineral Petrol.*, 122:428–430.

[Pitzer and Palaban, 1986] Pitzer, K. S. and Palaban, R. T. (1986). Thermodynamics of NaCl in steam. *Geochimica et Cosmochimica Acta*, 50:1445–1454.

[Pitzer et al., 1983] Pitzer, K. S., Peiper, J. C., and Busey, R. H. (1983). Thermodynamic properties of aqueous sodium chloride solutions. Technical report, Lawrence Berkeley Laboratory and Oak Ridge National Laboratory.

[Potter, 1978] Potter, R. W. (1978). Viscosity of geothermal brines. *Geothermal Resources Council, Transactions*, 2:543–544.

[Potter and Brown, 1977] Potter, R. W. and Brown, D. L. (1977). The volumetric properties of aqueous sodium chloride solutions from 0 ° to 500 °C at pressures up to 2000 bars based on a regression of available data in the literature. United States Government Printing Office, Washington, D.C. 20402.

[Potter and Haas, 1978] Potter, R. W. and Haas, J. L. (1978). J. Res. U.S. Geol. Survey, Volume 6, No 2.

[Pritchett, 1993] Pritchett, J. W. (1993). STAR User's manual. Appendix F.1—The "BRNGAS" equation-of-state. S-Cubed Report SSS-TR-89-10242, revision A. La Jolla, CA.

[Pruess, 1983] Pruess, K. (1983). Development of the general purpose simulator MULKOM. In Annual Report 1982 LBL-15500, Lawrence Berkeley Laboratory, University of California, Berkeley, CA.

[Pruess, 1987] Pruess, K. (1987). TOUGH User's Guide. Technical Report LBL-20700, Lawrence Berkeley Laboratory, University of California.

[Pruess, 1991] Pruess, K. (1991). TOUGH2—A general-purpose numerical simulator for multiphase fluid and heat flow. Technical Report LBL-29400, Lawrence Berkeley Laboratory, University of California.

[Roberts et al., 1987] Roberts, P. J., Lewis, R. W., Carradori, G., and Peano, A. (1987). An extension of the thermodynamic domain of a geothermal reservoir simulator. *Transport in Porous Media*, 2:397–420.

[Rogers and Pitzer, 1982] Rogers, P. S. Z. and Pitzer, K. S. (1982). Volumetric properties of aqueous sodium chloride solutions. *J. Phys. Chem. Ref. Data*, 11(1):15–81.

[Satik et al., 1996] Satik, C., Walters, M., and Horne, R. N. (1996). Adsorption characteristics of rocks from vapor-dominated geothermal reservoir at tThe Geysers. In *Proceedings 21st Workshop on Geothermal Reservoir Engineering*, pages 469 – 479. Stanford, CA.

[Saul and Wagner, 1989] Saul, A. and Wagner, W. (1989). A fundamental equation for water covering the range from the melting line to 1273 K at pressures up to 25000 MPa. *J. Phys. Chem. Ref. Data*, 18(4):1537–1564.

[Schmidt, 1979] Schmidt, E. (1979). *Properties of steam and water in SI-units.* Springer-Verlag. p.190.

[Silvester and Pitzer, 1976] Silvester, L. F. and Pitzer, K. S. (1976). Thermodynamics of geothermal brines, I. Thermodynamic properties of vapor-saturated NaCl (aq) solutions from 0–300 °C. Technical Report LBL-4456, UC-66, TID-4500-R64, Lawrence Berkeley Laboratory.

[Simonson et al., 1994] Simonson, J. M., Oakes, C. S., and Bodnar, R. J. (1994). Densities of NaCl(aq) to the temperature 523 K at pressures to 40 MPa measured with a new vibrating-tube densitometer. *J. Chem. Thermodynamics*, 26:345–359.

[Sourirajan and Kennedy, 1962] Sourirajan, S. and Kennedy, G. C. (1962). The system H_2O-NaCl at elevated temperatures and pressures. *American Journal of Science*, 260:115–141.

[Sterner et al., 1988] Sterner, S. M., Hall, D. L., and Bodnar, R. J. (1988). Synthetic fluid inclusions. V. Solubility relations in the system NaCl-KCl-H_2O under vapor-saturated conditions. *Geochimica et Cosmochimica Acta*, 52:989–1005.

[Stull and Prophet, 1971] Stull, D. R. and Prophet, H., editors (1971). *JANAF Thermochemical Tables.* U.S. Department of Commerce, National Bureau of Standards, 2nd edition.

[Tanger and Pitzer, 1989] Tanger, J. C. and Pitzer, K. S. (1989). Thermodynamics of NaCl-H_2O: A new equation of state for the near-critical region and comparisons with other equations for adjoining regions. *Geochimica et Cosmochimica Acta*, 53:973–987.

[Todd, 1980] Todd, D. K. (1980). *Ground Water Hydrology.* John Wiley & Sons, 2nd edition.

[Verma and Pruess, 1988] Verma, A. and Pruess, K. (1988). Thermohydrological conditions and silica redistribution near high-level nuclear wastes emplaced in saturated geological formations. *Journal of Geophysical Res.*, 93 (B2):1159–1173.

[Wahl, 1977] Wahl, E. F. (1977). *Geothermal Energy Utilization.* Wiley, New York.

[White, 1995] White, S. P. (1995). Multiphase nonisothermal transport of systems of reacting chemicals. *Water Resources Research*, 31(7):1761–1772.

[White and Kissling, 1992] White, S. P. and Kissling, W. M. (1992). Modelling geothermal reservoirs, recent developments. In *Proc. 14th New Zealand Geothermal Workshop*, pages 99–104. University of Auckland.

[Whiting and Ramey, 1969] Whiting, R. L. and Ramey, H. J. (1969). Application of material and energy balances to geothermal steam production. *J. Pet. Tech.*, pages 893–900.